FP7 2013 Cooperation Work Programme
Theme 6: Environment (Including Climate Change)

Novel indicators for identifying critical *INFRA*structure at *RISK* from Natural Hazards

Deliverable D3.1

Hazard Distribution Matrix

Primary Author	Dina D'Ayala, Pierre Gehl/University College London (UCL)
WP	3
Submission Date	16/12/2014
Primary Reviewer	Bryan Adey/Eidgenössische Technische Hochschule Zürich (ETHZ)
Dissemination Level	PU

This project has received funding from the European Union's Seventh Programme for research, technological development and demonstration under grant agreement No 603960.

Project Information

Project Duration: 1/10/2013 - 30/09/2016

Project Coordinator:
Professor Eugene O' Brien
Roughan & O' Donovan Limited
eugene.obrien@rod.ie

Work Programme: 2013 Cooperation Theme 6:
Environment (Including Climate Change).

Call Topic: Env.2013.6.4-4 Towards Stress Testing of Critical Infrastructure Against Natural Hazards-FP7-ENV-2013-two stage.

Project Website: www.infrarisk-fp7.eu

Partners:

Roughan & O' Donovan Limited, Ireland

Eidgenössische Technische Hochschule Zürich, Switzerland.

Dragados SA, Spain.

Gavin and Doherty Geosolutions Ltd., Ireland.

Probabilistic Solutions Consult and Training BV, Netherlands.

Agencia Estatal Consejo Superior de Investigaciones Científicas, Spain.

University College London, United Kingdom.

PSJ, Netherlands.

Stiftelsen SINTEF, Norway.

Ritchey Consulting AB, Sweden.

University of Southampton (IT Innovation Centre), United Kingdom.

Document Information

Version	Date	Description	Primary Author
Rev01	11/07/2014	Deliverable D3.1 on the estimation of hazard for an infrastructure system	D. D'Ayala, P. Gehl, M. Garcia-Fernandez, M. J. Jimenez, M. Ni Choine, M. Tucker, K. Gavin, K. Martinovic, Y.V. Avdeeva, P. van Gelder, M. T. Salceda Page, M. J. Segarra Martinez
Rev02	30/09/2014	Deliverable D3.1 on the estimation of hazard for an infrastructure system	D. D'Ayala, P. Gehl, M. Garcia-Fernandez, M. J. Jimenez, M. Ni Choine, M. Tucker, K. Gavin, K. Martinovic, Y.V. Avdeeva, P. van Gelder, M. T. Salceda Page, M. J. Segarra Martinez
Rev03	09/12/2014	Deliverable D3.1 on the estimation of hazard for an infrastructure system Final revision following review comments from ETHZ	D. D'Ayala, P. Gehl, M. Garcia-Fernandez, M. J. Jimenez, M. Ni Choine, M. Tucker, K. Gavin, K. Martinovic, Y.V. Avdeeva, P. van Gelder, M. T. Salceda Page, M. J. Segarra Martinez

Abbreviations

CAV	Cumulative Absolute Velocity
CDF	Cumulative Distribution Function
CI	Critical Infrastructure
EDP	Engineering Demand Parameter
GEV	Generalized Extreme Value distribution
GMPE	Ground-Motion Prediction Equation
I_a	Arias Intensity
IM	Intensity Measure
N_{eq}	Effective Number of Cycles
PDF	Probability Distribution Function
PFA	Peak Floor Acceleration
PGA	Peak Ground Acceleration
PGD	Permanent Ground Deformation
PGV	Peak Ground Velocity
Sa (Sd)	Spectral Acceleration (Displacement)
Sai	Inelastic Spectral Acceleration
SI	Velocity Spectrum Intensity

Table of Contents

1.0 SCOPE

Critical infrastructures (CIs) are exposed to several hazard types. In the INFRARISK project we concentrate on, earthquakes, landslides and floods. These can be further decomposed into hazard sub-categories (i.e. pluvial / fluvial / coastal floods or flood-induced scour) in order to take into consideration appropriate intensity measures and the corresponding damaging mechanisms (see Figure 1).

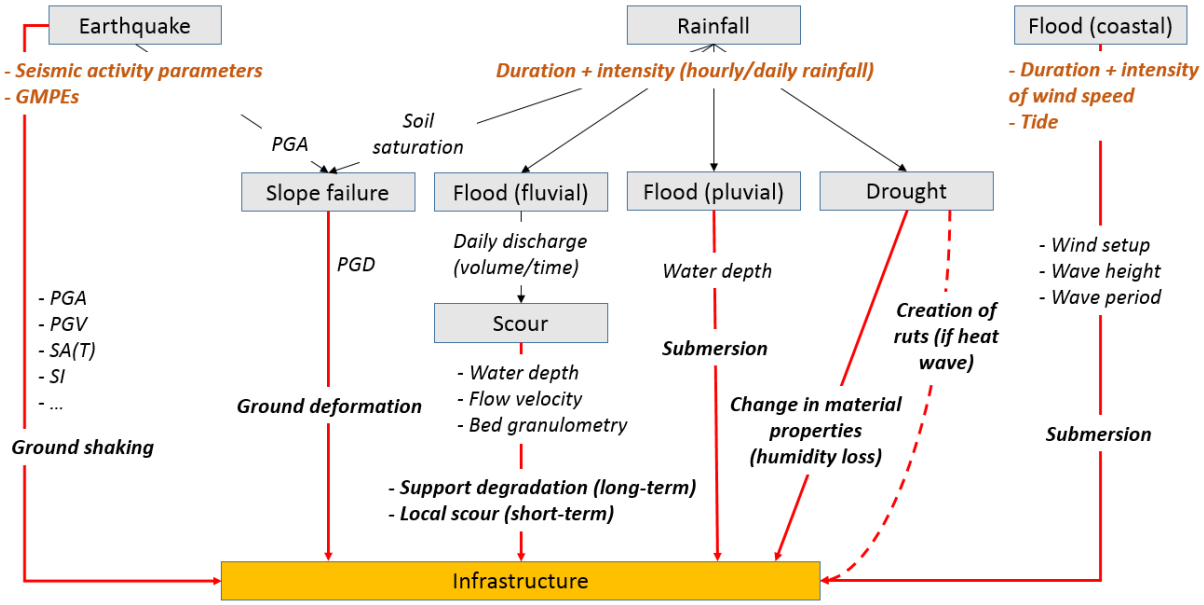

Figure 1: Preliminary presentation of the different hazard types considered in the INFRARISK framework

Even though some cascading events and interactions between hazards can be observed from Figure 1, the purpose of the present report is to review and harmonize analytical probability functions for single hazards. Therefore, in the present context, all hazard types are treated as independent: to this end, a simple probabilistic framework is proposed, where the hazard intensity level is evaluated at the site of interest, based on a given source or triggering event (see Figure 7). In the case of an independent hazard type, such as an earthquake, the source event can simply be the seismic activity that generates the ground motion. On the other hand, for induced hazards (for instance, scour at bridges), the source event has to represent the conditions created by the outcome of the triggering hazard (e.g. state of the channel section, in terms of depth and velocity, due to a fluvial flood). For each of the hazard types considered, probability models for the hazard propagation (i.e. from the source event to intensity measure at the vulnerable site) are then discussed. For consistency, three classes of variables are introduced in order to describe the source event and its effects:

- Source variables: they describe the nature / magnitude of the source event (e.g. seismic activity parameters for seismic hazard, duration and intensity of rainfall for floods).
- Propagation model variables: they describe the models that are used to compute the distributed intensity measures at the sites, given the occurrence of the source event.
- Site variables: they describe the specific conditions that are inherent to the vulnerable site of interest, for instance the soil class or the topography of the area. They can be seen as local

corrective factors with respect to the baseline intensity measures that have been computed with standard site conditions.

These three sets of variables for each of the primary or triggered hazards conditions allow computing the Intensity measure of interest at the site, given a correlating spatial-temporal model. This distinction follows the source-propagation-site (or source-pathway-receptor) framework that is usually used in hazard assessment procedures. For instance, in the case of seismic hazard, propagation-related uncertainties are represented by the variability in the GMPEs that can be possibly applied: as recommended by the FP7 SHARE project (http://www.share-eu.org), appropriate use of GMPEs for a given area should include a weighted combination of a set of various GMPEs, following a logic tree framework (Delavaud et al, 2012).

Following the Performance Based Engineering (PBE) framework, whether it is for earthquakes (Krawinkler, 1999) or for other hazards such as hurricanes (Barbato et al., 2013), each hazard type could be represented by a hazard curve that expresses the frequency of exceedance of a given intensity measure level over a given period of time and a selected geographical area:

$$\lambda_{im}(\mathrm{IM}) = P(im \geq \mathrm{IM} | \mathbf{O}, \mathbf{P}, \mathbf{S}) \quad (1)$$

Where IM represents the intensity measure (scalar or vector measure), **O** the vector of source variables, **P** the vector of propagation variables and **S** the vector of site variables. Each of the input variables **O, P** or **S** can include *epistemic* and *aleatory* variables. Moreover, in the context of stress-tests for CIs, the emphasis is put on the assessment of low-probability high-consequence events: the low-probability part has to be addressed by using specific statistical models such as extreme value distributions, which is the object of Section 2.

These two general chapters are followed by a series of thematic sections that describe the characteristics of the hazard models for earthquakes, landslides, floods and scour (Sections 5 to 8). For each of the hazard types we present an approach to consistently determine the description of and relationship among source events, propagation models, probability approaches and intensity measures, at different spatio-temporal scales. The spatial correlation issue is crucial in the case of spatially distributed infrastructures: the correlation of the intensity measures obtained at the sites will greatly influence the scale at which the fragility functions can be used. This is particularly true in the case of linear objects such as road segments, where the unit length to be selected as an elementary object may vary substantially depending on the object typology and characteristics, but also on the nature of the risk assessment performed.

To ensure harmonization of approaches among different hazards, so as to obtain commensurable risk measures, a simple proof-of-concept example is introduced in section 9: this sand-box application is used to benchmark the different assumptions and models for each hazard type. The aim is to ensure that the proposed methodology is applicable to a section of critical transport infrastructure, and verify whether the proposed IMs are properly usable as inputs to the fragility functions.

The results of the proof-of-concept exercise provide the operational outcome of this deliverable: a multi-hazard harmonization, presented in section 10: it takes the form of a hazard descriptor matrix, where the key parameters and assumptions are summarized for each hazard type. This allows a CI manager to build up the first block of a multi-risk assessment.

Finally, this document aims at reviewing and recommending the different hazard assessment methods that are to be used within the INFRARISK framework: it should be seen as a set of guidelines that can be applied in the specific context of multiple hazard assessments and low-probability high-consequence events.

2.0 THEORETICAL BACKGROUND

This section details the general mathematical framework that is used for the exploitation of empirical hazard data, in order to derive probabilistic models (i.e. probability of occurrence over a given return period). The focus is put on the estimation of extreme value distributions.

The following considerations are applicable to all hazard types considered here: earthquakes, floods or landslides. These models represent the first tier of analysis that is common to different hazard types. Then, more elaborate models are usually used for a given hazard type, in order to account for specific physical variables and behaviours (e.g. Gutenberg-Richter law and Ground Motion Prediction Equations in the case of earthquakes).

2.1 Methodological considerations about analytical probability distributions related to pluvial-, fluvial-, coastal floods and earthquakes

The methodology to derive analytical probability distributions is heavily based on the limit theorem (Fisher-Tippet) which states that the maximum of many random variables has a distribution which converges to a:

- Reverse Weibull (bounded maximum), or;
- Gumbel, or;
- Frechet (bounded minimum);

regardless of the parent distribution.

There are two conditions which need to be fulfilled:

- Random variables are independent;
- Random variables have the same parent distribution.

Assume that $X_1, X_2, ..., X_n$ are independent and identically distributed random variables coming from a parent distribution with a cumulative distribution function $F(x)$ and probability distribution function $f(x)$. Define $H_n = max(X_1, X_2, ..., X_n)$ then H_n has a CDF given by:

$$H_n(x) = P(\max\{X_1, X_2, ..., X_n\} < x) = F^n(x) \quad (2)$$

Notice that the percentiles of H_n move to the right with increasing n, approaching the upper and lower end points if they are bounded, or going to infinity if they are unbounded. When n goes to infinity, we have:

$$\lim_{n\to\infty} H_n(x) = \begin{cases} 1 & \text{if } F(x) = 1 \\ 0 & \text{if } F(x) < 1 \end{cases} \quad (3)$$

that is, the limit distribution degenerates to a Dirac function. To avoid this degeneracy, we transform the random variable x by means of constants a_n and b_n such that:

$$\lim_{n\to\infty} H_n(a_n + b_n x) = \lim_{n\to\infty} F^n(a_n + b_n x) = H(x) \quad (4)$$

where $H(x)$ is a non-degenerated CDF.

The above three extreme value distributions can be plotted using a semi-logarithmic graph:

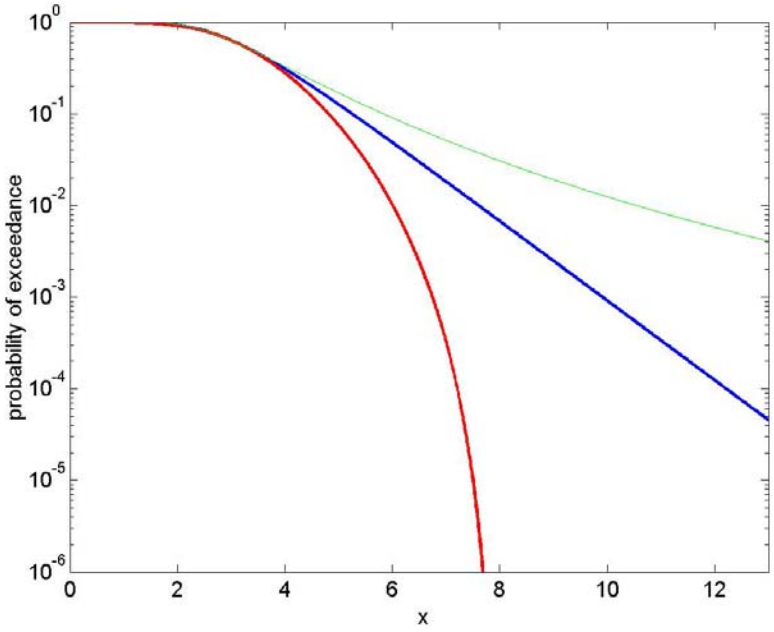

Figure 2: Extreme value distributions (Weibull in red, Frechet in green, Gumbel in blue)

The tail of the extreme value distribution can show a convex curvature (the red line, corresponding to a Weibull distribution), a concave curvature (the green line, corresponding to a Frechet distribution) and a straight line (the blue line, corresponding to a Gumbel distribution).

The above three types can be written as one overall 'Generalized Extreme Value distribution'. All three extreme value distributions are special cases of this Generalized Extreme Value distribution (GEV):

$$\mathrm{F}_{\mathrm{GEV}}(x)=\begin{cases}\exp\left\{-\left[1+\xi\alpha(x-u)\right]^{-1/\xi}\right\} & \text{for } \xi\neq 0\\ \exp\left\{-\exp\left[-\alpha(x-u)\right]\right\} & \text{for } \xi=0\end{cases} \quad (5)$$

With:

- $\xi = 0$: Gumbel (EV type I for maxima);
- $\xi > 0$: Frechet (EV type II for maxima);
- $\xi < 0$: Weibull (EV type III for maxima);

The domain of attraction shows the relationship between the parent and the asymptotic distribution. The short tailed distributions always lead to a Weibull domain of attraction, since the tail of the Weibull is finite.

Table 1: Relationship between the parent distribution and the asymptotic distribution type

Parent distribution	Asymptotic distribution type of maximum
Uniform, beta (short tail)	Reverse Weibull
Normal, exponential, gamma, lognormal, Weibull	Gumbel
Pareto, Cauchy, Student-t (fat tail)	Frechet

Sometimes physical considerations can be used to reduce the three limiting distributions to two. Parent distributions with a finite endpoint (like wave heights in shallow water) cannot lie in a Frechet-type domain of attraction (because they have their domain for *x* to infinity). Moreover, if we consider that the Gumbel distribution can be approximated as closely as desired by Weibull for maxima or Frechet, we conclude that the limit distribution can be selected solely from physical considerations. If we are dealing with random variables limited in the tail to the right, then a Weibull for maxima distribution is the limiting distribution.

From the assumption that we only have a set of extreme observations where the parent distribution *F(x)* is unknown, we would like to determine the domain of attraction. An estimator for the *c* parameter below can be found with the Pickands' method. Pickands (1975) shows that this *c* parameter is the same as the one in a Generalized Pareto distribution given by:

$$\mathrm{GPA}(x;a,c)=1-\left(1+cx/a\right)^{1/c} \quad (6)$$

Fitting its two parameters on the data gives us automatically the domain of attraction. As stated above a curvature observation of the data plotted on Gumbel probability paper can also be used:

Table 2: Relationship between the shape of the data plotted on Gumbel probability paper and the extreme value distribution

Convex curve	*H* is Weibull
Linear curve	*H* is Gumbel
Concave curve	*H* is Frechet

The central limit theorem explains why we might see so many times a normal distribution in practice: a stochastic variable that is influenced by a large number of independent processes will be approximately normally distributed. As we add more terms the approximation becomes better. This does not only apply to the sum but also to the average (which makes sense if one knows that if *X* has a normal distribution then it follows that also *a.X* has a normal distribution). In mathematical terms:

Given a set $X_1, X_2, \ldots, X_n$ of independent and identically distributed (i.i.d.) random variables, then:

$\lim_{n\to\infty}\frac{Y_n-n\mu}{\sigma\sqrt{n}}$ has a standard normal N(0,1) distribution.

The central limit theorem for the sum of random variables can easily be applied on the product of random variables by noting that log (product) = sum (log), and therefore: The product of n i.i.d. random variables converges to a lognormal distribution.

The analytical distribution type of probability density functions can be based on a number of theoretical considerations:

- Physical reasons;

- Probabilistic reasons, such as:
    - Central limit theory;
    - Extreme value theory;
    - Waiting time;
- Statistical reasons.

An example of statistical reasons is the diagram of β_1 (scaled skewness) versus β_2 (scaled kurtosis):

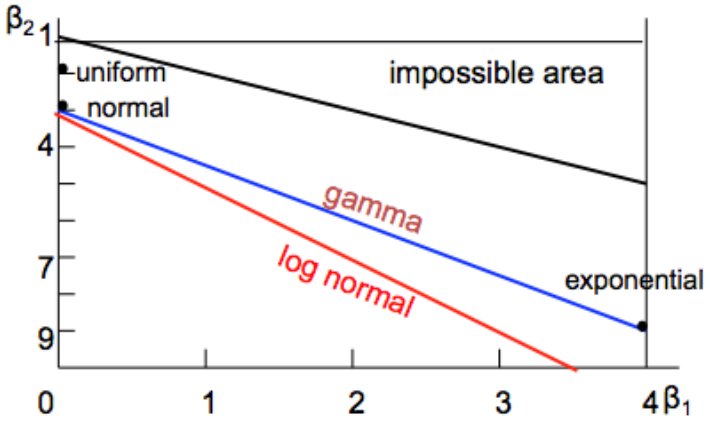

Figure 3: Scaled kurtosis as a function of scaled skewness for different probability distributions

For example, an exponential distribution, given by:

$$F(x) = 1 - e^{-\frac{x-\alpha_0}{\alpha_1}} \quad (7)$$

$$\beta_1 = \frac{m_3^2}{m_2^3} = \frac{\left(2\alpha_1^3\right)^2}{\left(\alpha_1^2\right)^3} = 4 \quad (8)$$

$$\beta_2 = \frac{m_4}{m_2^2} = \frac{9\alpha_1^4}{\left(\alpha_1^2\right)^2} = 9 \quad (9)$$

Is indicated by the node (4,9) in the above diagram. If the sample moments of the collected data are in the neighborhood of this dot, then there is reason to believe that the corresponding random variable is exponentially distributed.

Goodness of fit tests are suitable to test a hypothesized analytical probability distribution to a given dataset.

We test the compliance of the data with a distribution, for instance the χ^2-test.

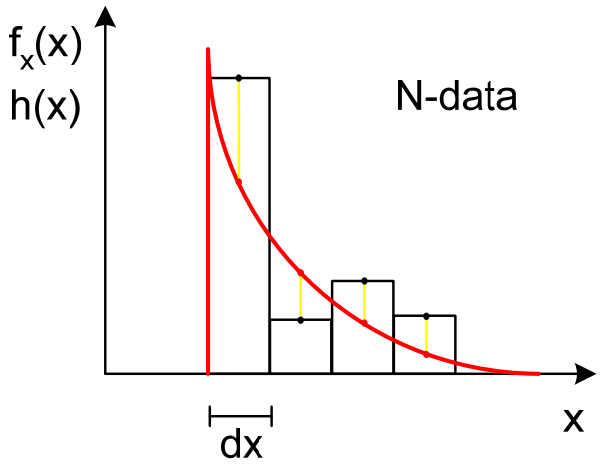

Figure 4: x^2-test for a given data set

The difference between the expected and actual number of observations is:

$$D = \sum \frac{(n_i - N \cdot p_i)^2}{N \cdot p_i} \quad (10)$$

$$\Pr\left\{D < x^2_{\alpha_i k-r-1}\right\} = 1-\alpha \quad (11)$$

If *D* remains below a certain critical value, the hypothesized analytical distribution can be accepted.

The Kolmogorov/Smirnov-test is another test to check the suitability of a given analytical distribution, conducted in the CDF domain, instead of the PDF domain:

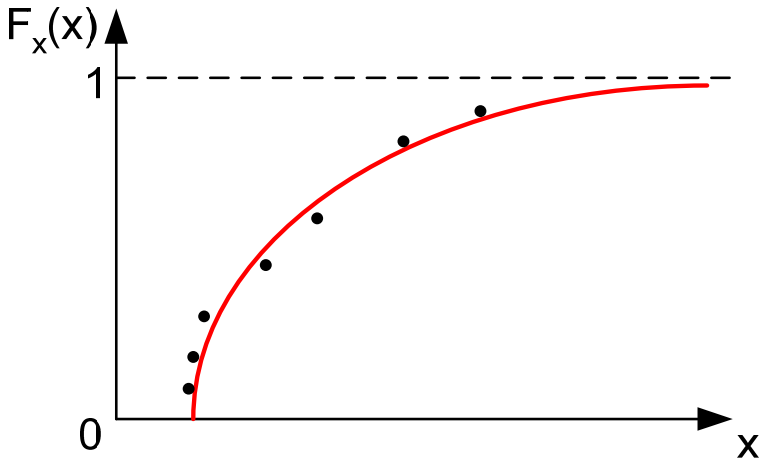

Figure 5: Kolmogorov-Smirnov test for a given data set

$$D = \max_{i=1..N} \left| 1 - \frac{i}{N} - F(x_i) \right| \quad (12)$$

$$\Pr\left\{ D < \frac{k}{\sqrt{N+r}} \right\} = 1-\alpha(k) \quad (13)$$

If *D* remains below a certain critical value, the hypothesized analytical distribution can be accepted.

Also relations between PDF's can be derived. The following relations have been found:

Table 3: Relationships between PDFs

X	***Y* = exp(*X*)**
Normal	Shifted Log Normal
Gumbel	Frechet
Exponential	Pareto

Finally it is possible to examine the tail behaviour of distributions. The following relations have been found (properties of the Halphen distributions are described in Perreault et al., 1999):

Table 4: Tail behaviour as a function of the return interval T

X	**Tail**
LogNormal	$\exp(\sqrt{\ln T})$
Gamma	$\ln T$
Normal	$\sqrt{\ln T}$
Halphen	T^{υ}

It is recommended (as well as in Mendel and Chick, 1993) to use theoretical considerations as much as possible in the distribution selection. Chick et al. (1995, 1996) proposed a physics-based approach to determine the PDFs of extreme river discharges. In their papers, a new model for predicting the frequency of extreme river levels is proposed which encapsulates physical knowledge about river dynamics, including formulae which describe river discharge. The model accounts for the river dynamics at a given location by modeling both how water gets into the river (via upstream tributaries) and how water leaves (discharge modeled by Chezy's equation). Although the simplified physical model makes several rough approximations (using memoryless properties and Chezy's equation for approximating discharge), insights were gained in the effects of Chezy's equation parameters on the shape of the curves relating the river level and flood return frequency can be shown with Chick's approach. These shapes do not always conform to the curves found for traditional models. In particular, the relation is not necessarily linear on log paper, as with the exponential model. It was shown that an increase in the power parameter of Chezy's equation led to a non-linear relation on log paper. As the power increased, the slope of the curve relating flood volume and the frequency of extreme floods decreased. This may be true for more complicated systems as well. It was concluded by Chick et al. (1995, 1996) that flood protection designs based on drawing straight lines on log paper would be conservative for extremely rare floods.

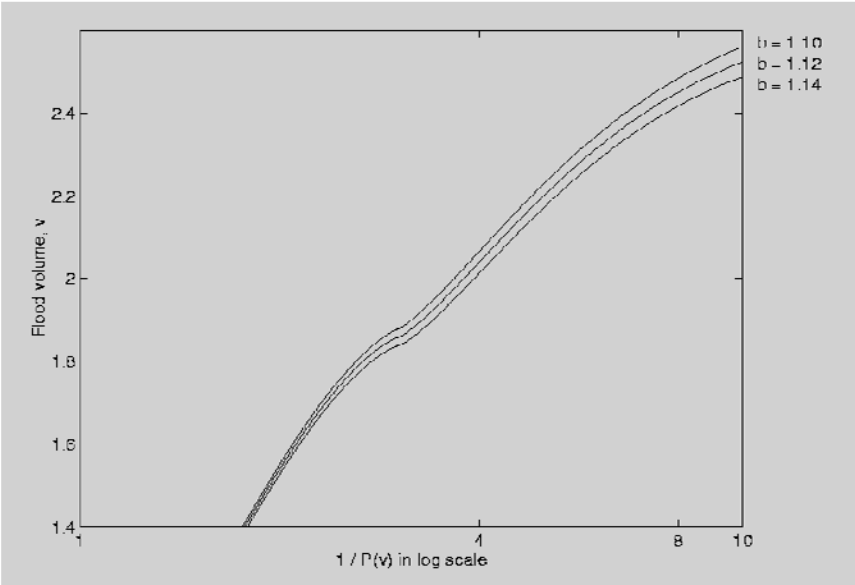

Figure 6: Effect of changes in the power parameter of Chezy's equation on the flood frequency curve (source: Chick et al., 1996)

Another interesting methodology to be considered is the regional frequency approach. The regional frequency analysis is widely used in flood analysis. The approach based on the theory of L-moments is developed by Hosking and Wallis (1997) is a reliable method for assessing exceedance probabilities of extreme environmental events when data is available from more than one site. The method of L-moments is analogous to the method of ordinary moments. The main advantage of L-moments is that, being a linear combination of data, they are less influenced by outliers whereas the ordinary moments requires squaring and cubing of the observed data. A well conducted regional frequency analysis involves objective and subjective techniques for defining homogeneous regions, assigning of sites to regions, identifying and fitting regional probability distribution to data, and testing hypotheses about distributions. The standard discordancy measure of Wilks for detection of multivariate outliers in terms of the sample L-moment ratios of the site's data is recommended by Hosking and Wallis (1997) as a guideline rather than a formal test during the process of initial data screening for forming the homogeneous region.

3.0 USE IN RISK MODELS

The previous chapter reviews some of the statistical approaches and models that can be used to verify and choose appropriate extreme values distributions. However in conducting risk analysis the focus should be not just on the probabilistic hazard models, but on efficient and robust selection of high-consequence events, i.e. what happens following the hazard event, with respect to the infrastructure under study. Figure 7 proposes an iterative process that allows to run preliminary loss scenarios and successive iterations, for main hazard events, but also for secondary hazard events, as for instance a landslide triggered by an earthquake, to determine the expected effect on the infrastructure and hence the necessity for a refined assessment .

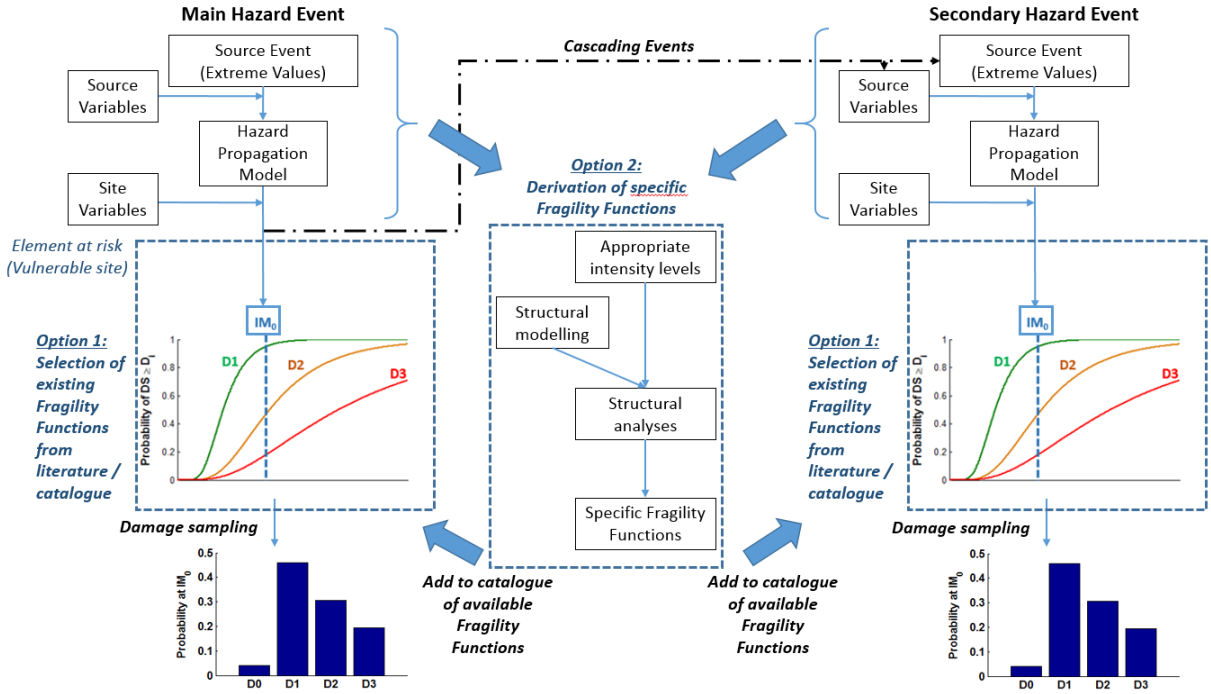

Figure 7: Proposed probabilistic framework for the hazard distribution at the CI components

As it can be seen in Figure 7, the appropriate selection of hazard source events ultimately serves two purposes:

- *Purpose 1:* to evaluate the hazard intensity level at each vulnerable site and to sample the component's damage state, based on a set of previously selected or generated fragility functions. For a given component at a given site, the probability of damage is estimated thanks to the set of fragility curves and the corresponding IM value (i.e. IM_0 in Figure 7): by comparing a standard uniform random variable with the damage probabilities, the damage state of the component can then be probabilistically sampled for each run.
- *Purpose 2:* to develop fragility functions with an analytical approach. This happens in the case that relevant fragility functions are not available for the given combination of hazard type and structural component. This can be done efficiently by tailoring the fragility study to the specific response of the infrastructure element to the level of intensity considered.

The knowledge of the nature and the intensity of the different source events, as well as the structural response to the applied loadings, are then essential to select the appropriate inputs for the derivation of the fragility functions. This can ensure that the fragility functions are accurate for

the correct range of expected intensity measures, especially in the case of low-probability events. This should also be used to check whether the selected fragility functions are actually valid for the desired range of hazard intensity.

For a given main hazard event, the computation of the distributed intensity measures serves the main purpose of feeding the fragility functions for the estimation of damage at the vulnerable sites. However, if interactions between hazards are assumed, then the main event intensity measures are also used to generate the initial condition (i.e. sources variables) for the triggering of a secondary event. Then, the same procedure for the selection / derivation of fragility functions is applied for the secondary hazard.

4.0 PROPOSAL FOR HAZARD DISTRIBUTION MATRIX

Several recent studies have tackled the issue of multi-hazard analysis. For instance, the FP7 MATRIX project (2010-2013) is focused on the hazards that are the most likely to affect Europe, namely earthquakes, landslides, volcanos, tsunamis, wild fires, storms and fluvial and coastal flooding. A distinction is made between the following frameworks:

- Single-type risk assessment, where losses are estimated for a single independent hazard type.
- Multi-type risk assessment, which may result from the occurrence of multiple hazard types, in the following configurations:
    - Simultaneous (and possibly independent) events occurring in the same area and time window;
    - Cascading events, where a given hazard event may trigger a secondary hazard event.

Two main approaches are identified in the MATRIX project for the comparison or combination of independent single risks (MATRIX, 2014), namely:

- Approach 1: The derivation of single risk curves, which implies the harmonization of temporal constraints, spatial scale and loss metrics for all hazard types;
- Approach 2: The development of a common framework, where all steps of the risk assessment procedure are harmonized (i.e. from hazard, to vulnerability and losses).

The use of risk curves has been promoted in the MATRIX project, since it allows for a straightforward combination and comparison of the considered risk levels. The combination of the aggregated risk that is associated to a given area is performed thanks to the independency assumption of the considered hazards: the total loss, P_{tot}, can be estimated as a function of the loss P_i associated with hazard type *i*:

$$P_{tot} = 1 - \prod \left(1 - P_i\right) \quad (14)$$

The comparison of two independent risks can also be performed for a given return period: the median of the loss distribution curves for the selected return period can be compared with some significance statistical tests, in order to check whether the differences between the potential losses induced by different hazard are notable or not. Such an exercise is directly aimed at facilitating the decision-making process that is involved in the resource allocation for risk mitigation.

When multiple hazards are considered, interactions have to be taken into account both at the hazard (i.e. cascading hazard events) and the consequence levels (i.e. cascading failure events): whether hazard events are considered simultaneous or triggered, the aggregation of the total losses usually requires vulnerability models that are able to account for the joint loading of two or more hazard types (see Figure 8). Finally, a combination of event- and fault-tree formulations is often employed in order to ensure an exhaustive exploration of all possible cascading scenarios.

Other studies by Selva (2012) and Garcia-Aristizabal & Marzocchi (2012) draw the same conclusions for the single-risk assessment of multiple hazards: such a framework requires a preliminary harmonization task, where a temporal and spatial homogenization of the risk assessment is carried out, as well as the definition of common metrics for loss assessment.

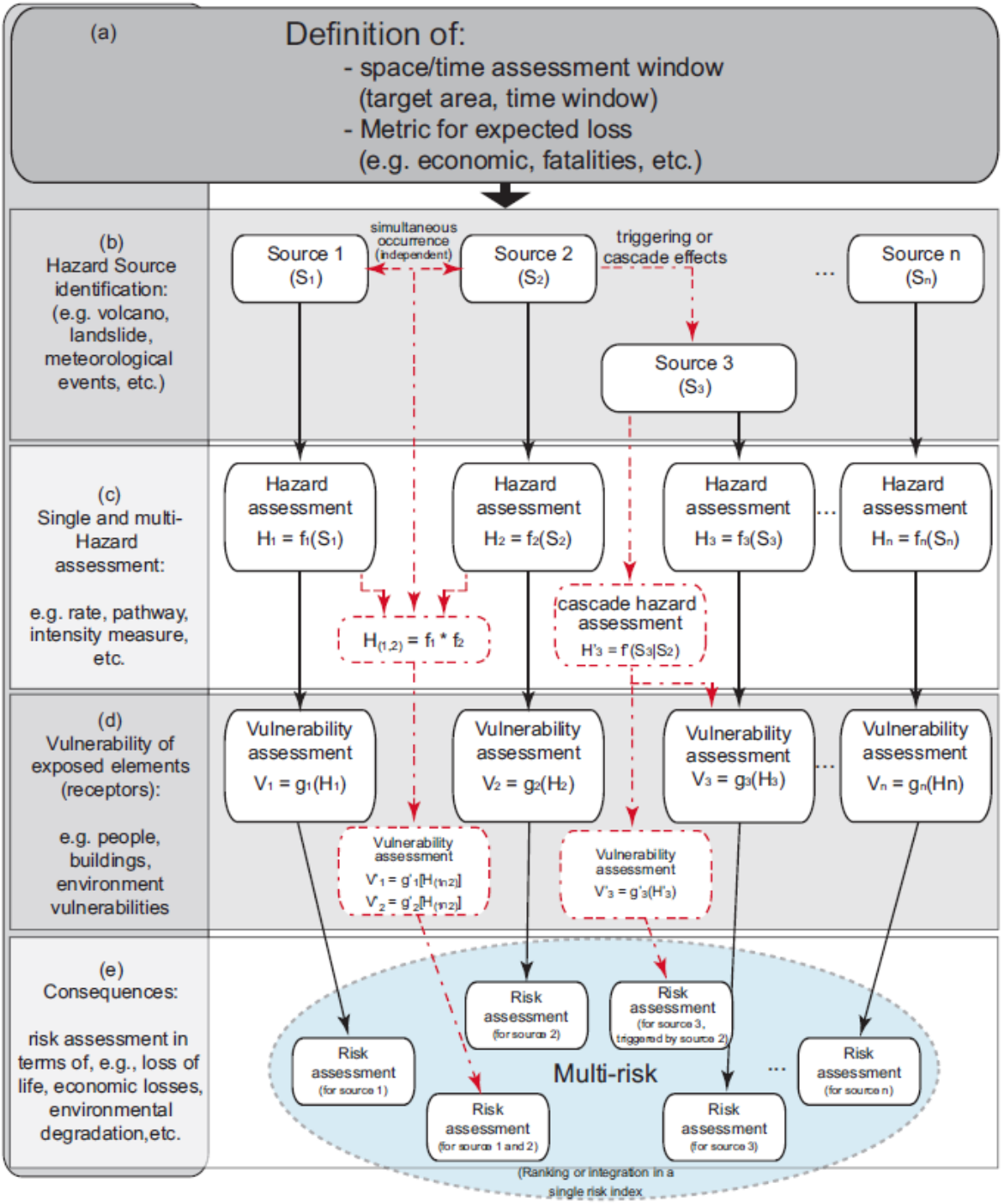

Figure 8: Proposition for multi-risk assessment, from Marzocchi et al. (2012)

Work Package 3 focuses on the analysis related to single hazard events, therefore, a simple risk convolution (i.e. the multiplication of the probability of occurrence of an event and its consequences for a given hazard, area and time period) following the black paths in Figure 8 can be carried out for each hazard type, as detailed in section 3, with the option of considering secondary triggered hazards. However, as the final objective of INFRARISK is to conduct multi-risk analysis, it is critical that at this stage a consistent procedure is proposed to estimate homogeneous distributions $\lambda_{im}(IM)$ for all hazards, before performing a convolution with the fragility functions. Therefore, it is proposed to represent all relevant hazard parameters within a Hazard Distribution Matrix (HDM): this matrix is

organized as a double entry table where each column represents a given hazard type and the describing parameters are detailed in the rows. Each hazard type is specified by the following main features:

- Source and site variables that are used to parameterize the hazard model. In the case of an independent hazard event, source variables are based on the distribution of physical parameters (e.g. rainfall pattern over the studied area or activity parameters of a seismic fault). In the case of an induced hazard, source variables result from the outcome of the triggering event (e.g. landslide probability expressed with respect to the seismic ground-motion distribution).
- Recommended method: the type of specific hazard assessment procedure that is advocated for use in the context of the INFRARISK framework.
- Distributed IM at site: which intensity measure is actually computed by the hazard model, for subsequent use as input to the fragility functions.
- Probabilistic model: whether a probabilistic model is available from a literature or only a set of deterministic equations can be used.
- Uncertainties: these are usually induced by the variability in the source or site variables, but they can also result from the hazard prediction models (e.g. standard-deviation associated with the ground-motion prediction equations).

Since the INFRARISK WP3 is focused on single risk analysis, the different hazard levels could be convolved by considering hazard types as independent events, therefore resulting in a linear combination of each hazard convolution, as presented in Figure 9.

The next step will then consist of using the results from D3.2 (Fragility Function Matrix) in order to perform a risk convolution for all hazard types and aggregating potential losses, under the assumption of a single risk analysis (i.e. independent events).

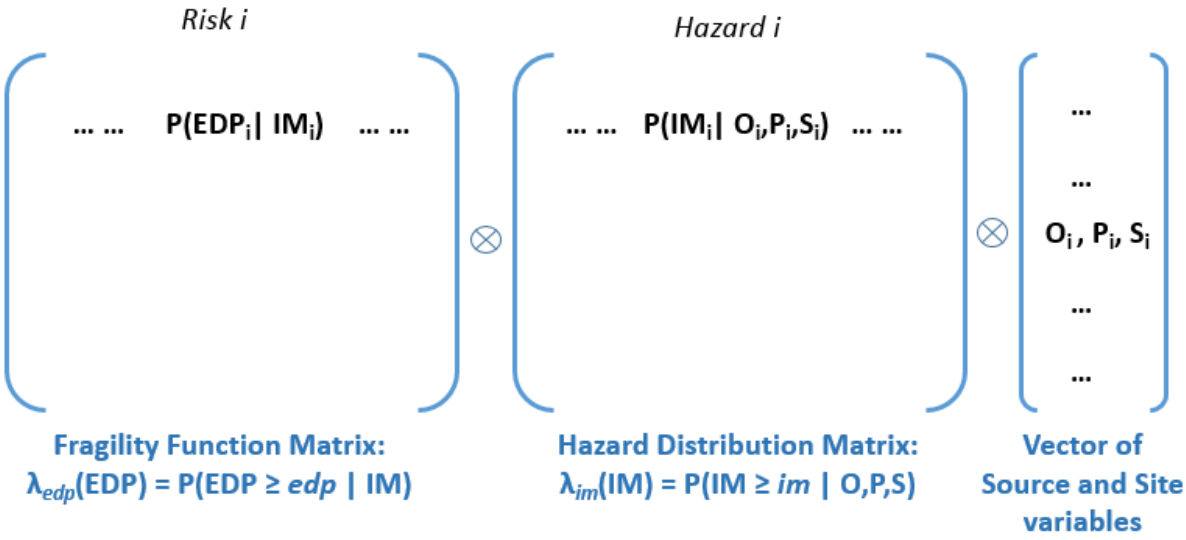

Figure 9: Proposed framework for the single risk analysis

5.0 EARTHQUAKES

5.1 General description

This section summarizes the expected development of earthquake ground shaking hazard to define the seismic input that could affect CIs resulting on damage / disruption. The corresponding branch from the hazard scheme of Figure 1 is highlighted in Figure 10.

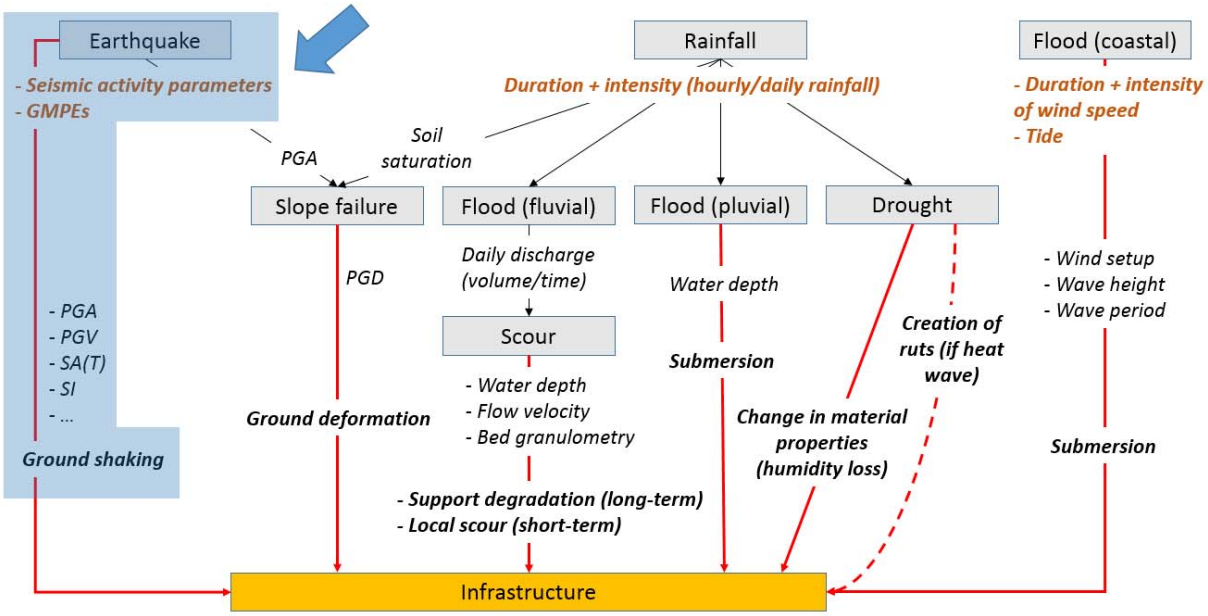

Figure 10: Synthesis of considered hazards and their corresponding IMs. Earthquake ground shaking hazard corresponds to the branch with grey background, the blue arrow pointing at it (from D3.1 section on IMs by UCL)

5.2 Intensity measures

Ground motion intensity can be characterized by different parameters or Intensity Measures, IMs. The selection of the most appropriated IMs should be mainly guided by the infrastructure type under analysis and the working scale; i.e., which IM contribute most to damage to the system and/or its components.

Instrumental IMs are by far the most reliable to characterize ground motion, as compared to empirical IM based on damage observations (macroseismic intensity). The methodology to generate ground shaking intensities allows for having both single-value IM and synthetic ground-motion time histories (e.g., accelerograms).

Most common ground shaking IM for highway and railway infrastructure, including single elements as bridges, is peak ground acceleration, PGA; but peak ground velocity, PGV, spectral acceleration at specific frequencies, SA(f),or velocity spectrum intensity, SI, are also commonly used, among others.

Table 5 summarizes a preliminary selection of IMs that were considered most efficient for different elements at risk in the framework of the European project SYNER-G (2011).

Table 5: Selected efficient Intensity Measures for different systems (from Deliverable D2.13 of SYNER-G, 2011)

IM	Context
PGA	Acceleration sensitive structures (e.g. substations, pumping, storage), machinery and electric components Non-structural components (i.e. PFA) Tunnels Bridges
PGV	Pipelines Intermediate-period structures
Sa / Sd	Buildings (all periods) Bridge components (i.e. columns) Sliding block displacement (known masses)
I_a	Sliding block displacement (uncertain masses, stiff slope) Bridge response (components with uncertain properties)
CAV	Liquefaction
N_{eq}	Liquefaction
SI	Sliding block displacement (uncertain masses, ductile slope) Building foundation response Soil-structure interaction
Sai	Buildings (estimates of inelastic response properties)
IM_{1E+2E}, IM_{1I+2E}	Large buildings (known estimates of higher periods)

5.3 Spatial scale of analysis

As it is described in section 5.4.4., seismic hazard analysis should be carried out considering a sub-regional scale; i.e., 100-200 km around the CI of interest. Single-site analysis could be performed for individual components of the CI, each one considered as a unit, provided there is enough information available on local soil characteristics.

5.4 Methodology

5.4.1 Seismic hazard and seismic risk

Seismic risk can be defined as the multiplication of the probability of occurrence of a seismic event and its consequences for a given seismic hazard, area and time period.

The most common outputs obtained from seismic risk analyses, which depend on the way in which the seismic hazard is modelled, are summarized in Table 6 from Crowley et al. (2010). It includes events from both deterministic and probabilistic approaches.

Table 6: Different possible outputs as a function of the hazard description (from Crowley et al., 2010)

Hazard description	'Risk' output
Deterministic events, maps of ground shaking	Damage / loss maps (i.e. spatial distribution of damage / loss) that are conditional on a given event occurring
Hazard maps	Damage / loss maps that are conditional on the hazard with a given return period
Hazard curves	Single asset "loss curves" (better known as loss exceedance curves) and damage / loss for a given return period
Probabilistic events-based ground-motion fields	Multiple asset (aggregate) loss curves and aggregate damage / loss maps with a given return period

The different outputs have varying uses. Among them,

- to plan for interventions, for example in the case of emergency planning or post-earthquake rapid loss assessment when a single earthquake scenario is considered;
- to provide a simple comparative estimate for different assets of the levels of conditional or unconditional risk when a hazard map or hazard curve is used;
- to produce aggregate loss exceedance curves of portfolios of buildings/ exposed assets, using probabilistic events-based ground-motion fields (for example, based on Monte Carlo simulation).

5.4.2 Seismic hazard assessment

General goal of earthquake engineering analyses is to ensure that a structure can withstand a given level of ground shaking, hazard, while maintaining a desired level of performance (Baker, 2013). The evaluation of seismic hazard requires an estimate of the expected ground motion at the site of interest. Basically, two main approaches are considered for seismic hazard assessment, deterministic and probabilistic.

Going beyond the observation of effects from past earthquakes and looking at the causes of seismicity, a first approach to evaluate the ground motion that could affect a structure in an earthquake is given by the Deterministic Seismic Hazard Assessment (DSHA). It originated in the NPP (Nuclear Power Plant) industry. Basic objective of a DSHA is to identify a 'worst-case' scenario ground motion that could affect the facility of interest, so design seems to be bound to be safe. Main steps include finding the nearest active fault/earthquake source, defining the largest earthquake that could be generated, assuming the largest earthquake happens at the closest point to the site, and calculating what the ground motion will be. When using DSHA, conceptual problems arise quickly and are difficult to overcome; including very often the possibility of coming up with grossly over-conservative hazard values, which not necessarily are those potentially more dangerous for the facility (e.g., in terms of spectral content).

Probabilistic seismic hazard assessment (PSHA) is concerned with the evaluation of the likelihood of strong motion intensities, which may cause destruction of buildings and infrastructure, and disruption of economic and social activities (Atkinson and Goda, 2013). PSHA aims to quantify the uncertainties about the location, size, and resulting shaking intensity of future earthquakes, and combine them to produce a description of the distribution of future shaking levels, and their

associated rates of exceedance, that may occur at a site. Basic PSHA, as developed from the original concept by Cornell (1968), is composed of three major modules: (1) identification of earthquake sources capable of producing damaging ground motions and characterization of earthquake occurrence in time and space, (2) ground motion intensity (shaking) prediction, including path and site effects, and (3) integration of hazard contributions and modelling of uncertainties.

A key limitation to the deterministic approach is that the range of possible earthquakes is not captured, and the selection of the worst-case scenario, both in terms of earthquake and associated ground motion intensity, is not straightforward. The critical choice for a 'worst-case' earthquake is already difficult and subjective (actually, the worst-case event would be that with the maximum conceivable magnitude located directly below the site, which is not necessarily realistic); but it is even a greater problem to define the worst-case ground motion intensity produced by this earthquake.

Figure 11a shows a simple example of the limitations of DSHA for identifying a worst-case event. The M6.5 nearby event from fault A produces larger spectral acceleration amplitudes at short periods at the site, while the M7.5 earthquake from fault B produces larger amplitudes at long periods (Figure 11b). So, while one could take the envelope of the two spectra, there is not a single 'worst-case' event that produces the maximum spectral acceleration amplitudes at all periods (Baker, 2013). These challenges prevent of finding a true 'worst-case' event, leaving DSHA to alternatively identify a 'reasonably large' event (e.g., a nearby large-magnitude earthquake with some level of reasonable associated intensity identified). An event chosen that way is classically described as a 'Maximum Credible Earthquake' (MCE). More recently, the same acronym, MCE, is retained in DSHA to mean 'Maximum Considered Earthquake'; to recognize the fact that larger earthquakes, and larger ground motion intensities, are likely to be credible as well.

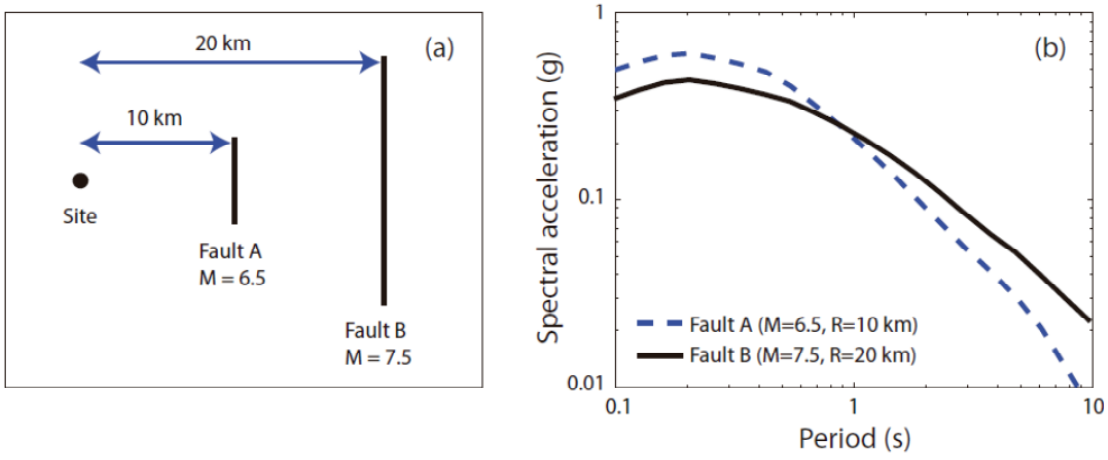

Figure 11: (a) Map view of a hypothetical site located 10 km from a fault capable of producing a maximum magnitude of 6.5, and 20 km from a fault capable of producing a magnitude 7.5 earthquake. (b) Predicted median response spectra from the two maximum earthquakes (*from Baker, 2013*)

The response spectra in Figure 11b represent median values predicted by empirical models developed and calibrated from recorded ground motions. By definition, these median values are exceeded in 50% of observed values for the same magnitude and distance. To illustrate the significant scatter around ground motion prediction models, Figure 12 shows observed spectral

acceleration values at 1 s period from the 1999 Chi-Chi, Taiwan earthquake, and an empirical model of ground motion prediction (Baker, 2013). At short distances (1-3 km) observed values vary nearly one order of magnitude. The one-standard-deviation bounds (dashed lines) should enclose about 2/3 of the observed values, considering that scatter of the log of spectral accelerations around the mean prediction is well-represented by a normal distribution (PDF plot in Figure 12). Still, that will be exceeded 16% of the time, which corresponds to the probability of a normal random variable being more than one standard deviation greater than its mean (Baker, 2013).

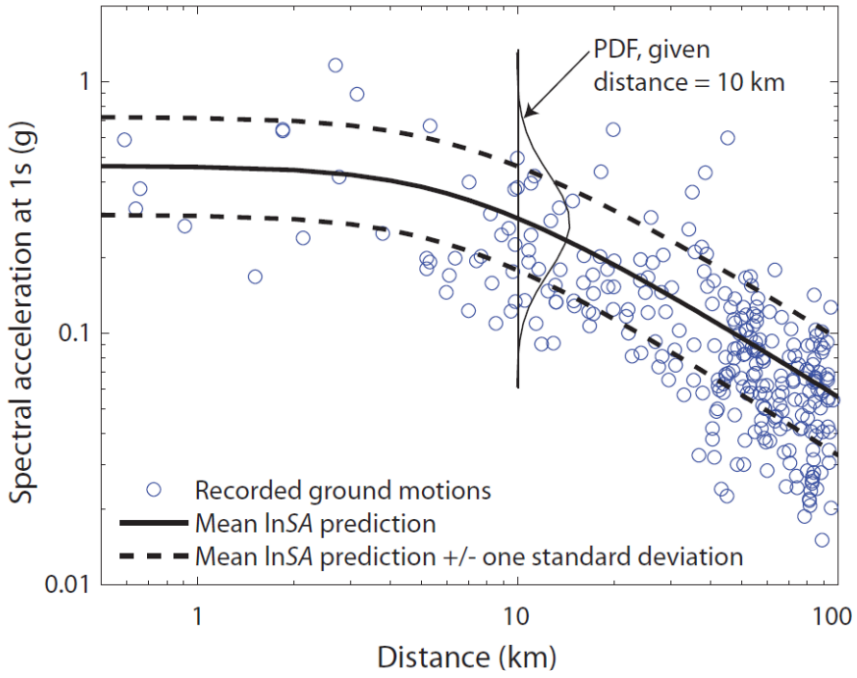

Figure 12: Observed spectral acceleration values at 1 s from the 1999 Chi-Chi, Taiwan earthquake, and empirical ground motion prediction model of Campbell and Bozorgnia (2008), illustrating variability in ground motion intensity (*from Baker, 2013*)

In the case of spatially distributed infrastructure, or infrastructure networks, the deterministic approach to seismic hazard analysis (DSHA), using one single scenario earthquake (relative popular in current practice), suffers from conceptual problems difficult to overcome as described above.

An approach to seismic hazard analysis for infrastructure networks in a probabilistic-based framework allows addressing the identified concerns. PSHA is not searching for a 'worst-case' ground motion intensity; instead it considers all possible earthquakes and resulting ground motions, along with their associated probabilities of occurrence, in order to find the level of ground motion intensity exceeded with some tolerably low rate (Baker, 2013).

5.4.3 Probabilistic-based approaches

The conventional way of performing hazard calculations to evaluate the expected ground motion intensities for different probability levels is by numerical integration (total probability theorem). This kind of approach has been implemented in recent applications at European (SHARE: http://www.share-eu.org) and global (GEM: http://www.globalquakemodel.org/) scales, where the OpenQuake software suite of open-source software was used (http://www.globalquakemodel.org/openquake/about/).

An alternative approach, especially suited when looking for low probability ground motions, is by using Monte Carlo simulation, which gives exactly the same results for the same input models with the advantages of being a more transparent procedure, facilitating the identification of events that contribute more to target amplitude levels (deaggregation at any probability level), having a more powerful and flexible handling of uncertainties, and making straightforward the link with probabilistic risk analysis, where Monte Carlo simulation is a common tool (Musson, 1999, 2000, 2012; Crowley and Bommer, 2006; Hong et al., 2006; Shiraki et al., 2007; Atkinson and Goda, 2013).

Following the Monte Carlo approach for seismic hazard assessment, first a synthetic earthquake catalogue is generated by drawing random samples from given spatio-temporal features of seismicity; i.e., earthquake-source geometries and seismicity model parameters (e.g., magnitude recurrence, focal deph) for magnitudes greater than a minimum threshold. On a second step, the synthetic catalogue is used to obtain ground motion amplitudes at the site(s) of interest (i.e., ground motion catalogues), by specified ground-motion prediction equation(s) (GMPEs). Ground motion variability (to account for the fact that a magnitude-distance combination does not always give the same ground motion) is considered by generating random values of epsilon (number of standard deviations from the median) to obtain a final ground motion value based on the expected scatter, or aleatory variability, from the sigma value of the GMPEs.

The classical approach to considering epistemic uncertainty in ground-motion generation and propagation is by using multiple GMPEs, though it is not necessarily the best one (Atkinson and Goda, 2013). Ground motion catalogues are then derived considering aleatory variability by multiplying a random number drawn from the standard normal distribution by the sigma value of the GMPE and adding it to the GMPE median motion. This simulation procedure may be an alternative to capture intra-event variability for a given single scenario. Mean hazard curves are built from the sorted maximum ground motions as a function of exceedance probability, and mean fractiles at various annual probabilities of exceedance can also be extracted. Deaggregation at any probability level is obtained directly for tracking those combinations of sources, GMPE and sigma contributing the most to the hazard curves.

An alternative to this traditional approach of separating epistemic and aleatory components, for characterizing uncertainties in ground motion prediction, is by treating them as being equivalent. All uncertainties are considered in the same way, through the Monte Carlo simulation procedure, allowing for efficient sampling of the parameter space, and providing the treatment of the obtained ground motion amplitudes using extreme-value statistics. Regardless the kind of approach followed and assuming that the total uncertainty is correctly estimated it does not affect the mean hazard (McGuire, 2004). It is increasingly recognized in the literature that the division in two components is somehow artificial and it could lead to overestimate (or even to underestimate in some cases) the total uncertainty (Bommer et al., 2005; Bommer and Scherbaum, 2008; Atkinson and Goda, 2013). Furthermore, it is important to carry out comprehensive sensitivity analyses to identify the controlling factors for PSHA results. In some cases, these analyses may be even more important than uncertainty analysis, in that they can provide insight into the critical assumptions driving the PSHA results (Atkinson and Goda, 2013).

The joint consideration of the epistemic and aleatory components of uncertainty is a way to defining the expected future distribution of ground motion amplitudes based on uncertain input parameters. Especially at low probabilities, this helps reducing unintended conservatism in computed seismic

hazard estimates. In addition, those amplitudes follow a general extreme-value distribution, which allows a robust fitting of their statistical parameters, since the use of a Monte Carlo simulation approach eliminates the problems associated with sparse statistics, as it is often the case when applying extreme-value methods. Treating uncertainty this way facilitates investigation of the occurrence of extremes (very low probability of exceedance); i.e. realization of extreme amplitudes over long periods of time from unlikely combinations, resulting in larger predicted extremes for low-probability fractiles. A summary of the Monte Carlo simulation process as applied to PSHA is shown in Figure 13 (Musson, 2012).

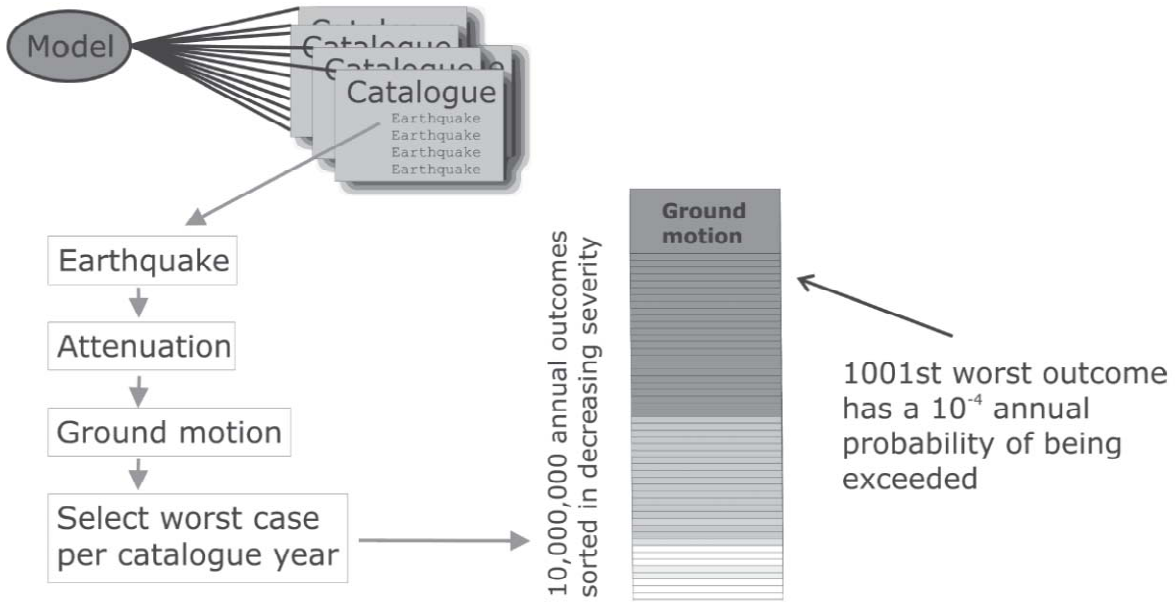

Figure 13: Summary of the Monte Carlo simulation process for PSHA (from Musson, 2012)

5.4.4 Low-probability high-consequence hazard

The selection of methods/metrics/data for hazard assessment is strongly dependent on how a low probability high-impact hazard 'event' affecting a CI is defined.

In what follows, regarding earthquakes, an 'event' will be considered as a level of ground motion shaking isolated from its effects on the CI; and 'low probability' will be interpreted as such that available hazard assessments (e.g., building codes) do not provide expected seismic input at those probabilities (e.g., annual probability of exceedance of 10^{-4}-10^{-5} for NPP stress tests). Most important is that the low probability levels have to be linked in advance to the performance of the CI (e.g. Miller and Baker, 2013).

A suitable approach may be summarized in the following two steps:

- A first step consists of carrying out a preliminary performance analysis of the CI and its main elements, identifying the weak points/elements and the associated ground motion input values leading to failure; following a similar approach as e.g., the HCLPF for NPPs (NRC, 2010). HCLPF stands for High Confidence of Low Probability of Failure Capacity. It is an index of seismic margin for NPP components. It considers both the uncertainty and randomness variability and is the acceleration value for which there is a 95% confidence that the failure probability is less than 5%. For some applications a mean value can fit, and uncertainty

analysis is not performed; then the HCLPF capacity is approximately defined as a 1% conditional probability of failure (EPRI, 2002)

- On a second step, representative generic or specific (see details below) ground motion fields consistent with the selected performance level/exceedance (e.g., annual probability of extensive-damage/collapse) is identified and their corresponding probability/percentile-fractile calculated by applying a Monte Carlo simulation approach.

This approach to low probability seismic input develops ground-motion 'catalogues' for selected areas (spatial scale should be defined), and corresponding to expected hazard events for different seismic characteristics (e.g. low, medium and high seismicity areas), from which the required probability/percentile-fractile can be selected by the user. Additionally, region-specific ground motion field catalogues are developed.

The procedure to obtain seismic input should be based on Monte Carlo simulation to allow dealing with low probability ground-motions. For optimization of the procedure, a preliminary sensitivity analysis is carried out to try to identify main factors driving the PSHA results, and its alternative approaches are normally for the treatment of uncertainties taken into consideration; i.e., separating aleatory and epistemic, or considering both in the same way. It should include the following main steps:

- *Seismogenic sources & seismic catalogues*
  An area, e.g., 100-200km, around the CI is considered as the potential seismic source. This approach of considering the CI located inside a seismic source area represents a kind of 'worst case', when compared to source models of several area sources surrounding the CI location. Alternatively, a specific fault could be the source, provided its geometrical and activity parameters are given; but then spatial bias could be introduced. In both cases, the source is modelled based on its seismicity parameters (e.g., using those parameters derived for Europe in SHARE project, available in the Portal of European Facility for Earthquake Hazard and Risk, EFEHR, www.efehr.org), and then an earthquake catalogue of predefined length (or a set of sub-catalogues) is generated by Monte Carlo simulation. Most important will be to define in advance the annual probabilities of interest of ground motion exceedance in order to derive stable and reliable results (e.g., robust ground motion shaking hazard, including its uncertainty, is obtained when the length of the simulated catalogue is about 1000-2000 times the return period of interest).

- *GMPEs*
  A set of GMPEs, with associated relative weights, should be selected. An example from the criteria developed in the European project SYNER-G (SYNER-G, 2011) is summarized in Table 7.

- *Seismic input*
  The resulting seismic input is given in the form of site-specific ground motion 'catalogues' along with mean-hazard curves. In addition, deaggregation and fractiles at selected probability levels are provided. In all cases, the different ground motion IMs previously selected (PGA, PGV, SA at various frequencies/periods) are calculated for rock-like sites. Site effects, if relevant, can be added with factors from standard soil classifications (e.g. EC8) or specific for the site, if available.

Table 7: Candidate GMPEs for application to European case studies in SYNER-G (from Deliverable D2.13 of SYNER-G, 2011)

Model	Applicable IMs	IM Definition
Akkar et Bommer (2010)	PGA, PGV, Sa/Sd	Geometric Mean
Bindi et al. (2010)	PGA, PGV, Sa/Sd	Maximum
Bommer et al. (2009)	Td	Arbitrary, Geometric Mean
Boore and Atkinson (2008)	PGA, PGV, Sa/Sd	GMRot150
Bozorgnia et al. (2010)	Sai (constant ductility)	GMRot150
Campbell and Bozorgnia (2008)	PGA, PGV, Sa/Sd	GMRot150
Campbell and Bozorgnia (2010)	CAV	Geometric Mean
Cauzzi and Faccioli (2008)	PGA, Sd	Geometric Mean
Danciu and Tselentis (2007)	PGA, PGV, Sa/Sd, I_a, SI, CAV	Arithmetic Mean
Kramer and Mitchell (2006)	CAV	Arithmetic Mean
Stafford and Bommer (2009)	N_{eq}	Independent
Travasarou et al. (2003)	I_a	Arithmetic Mean

- *Uncertainties*
  As it was referred to earlier, blending of aleatory and epistemic uncertainty is the preferred approach. Both are treated as being equivalent and considered in the same way in the PSHA calculations (as stated above, it is increasingly recognized among the hazard community that there is no fundamental reason to treat them separately, being this distinction somehow artificial). This alternative approach provides the same mean hazard curves as that from the traditional separation of aleatory/epistemic components, and allows obtaining a distribution of maximum amplitudes that follows a general extreme-value distribution, facilitating the analysis of the occurrence of extremes, as required in the specific approach to low probability hazard.

- *Correlation*
  Spatial correlation of ground motion plays a significant role when hazard analysis requires the quantification of joint occurrences at several sites during the same earthquake. A similar situation holds for correlation between various IMs; especially regarding the selection of ground motion time histories for Performance Based Design (PBD). As explained above, PSHA by Monte Carlo simulation provides an alternative procedure to capture intra-event variability for single earthquake scenarios. The need for additional spatial correlation analysis and correlation between ground motion parameters should be evaluated (available models from the literature can be used; e.g., Jarayam and Baker, 2009; Bradley, 2011).

Following the described approach, not only the expected low probability hazard consistent with the selected CI performance is provided, but also the consistency with respect to its further use in risk assessment together with the extreme-value analysis for the development of stress tests.

Following the same philosophy of ‘low frequency, high-consequence hazards’, the results from the standard cases above, namely extreme values and disaggregation, could be considered for defining the source parameters for generating synthetic time-histories by e.g., stochastic point-source or

finite-fault modelling (random horizontal component of acceleration) to populate a catalogue of ground motions for fragility curves derivation. Eventually, those could be complemented with real records fitting the criteria used for the generation of synthetics, if available.

5.5 Conclusions

When the focus is on low probability high-consequence seismic hazard events affecting CIs suggests the use of a probabilistic-based approach applying Monte Carlo simulation methods as most adapted. This approach produces the same output as conventional PSHA methods using the same input data. Main advantages of using Monte Carlo simulations rather than the numerical integration involved in traditional PSHA are:

a) the capability of using large synthetic seismic catalogues to allow for analysis of events with a low probability of occurrence;

b) a more transparent handling of disaggregation at any probability level (i.e. return period of ground motion level), giving more information about the hazard in terms of earthquakes and distances contributing most to specific ground motions;

c) a more flexible and powerful way of dealing with uncertainties, which can be handled as distribution functions, with their mean and standard deviation, where values are sampled for each simulation.

By contrast, in conventional PSHA, the use of logic trees not only introduces subjectiveness (i.e. mostly base on 'expert' opinion) in the choice of weights for each branch (Musson, 2000), but also can be problematic due to the exponential expansion of the number of tree combinations when using relatively complex models of uncertainties.

The distinction between aleatory and epistemic components of ground motion uncertainty, which are implicitly coupled, could be ambiguous and non-unique, because parts of the total uncertainty could belong to either component (Strasser et al., 2009), and there is a risk of 'double-counting' that overestimates total uncertainty leading to artificially large hazard values at low probabilities (Atkinson and Goda, 2013). This fact, widely acknowledged (Bommer et al., 2005; Bommer and Scherbaum, 2008; Strasser et al., 2009; Atkinson and Goda, 2013), suggests that the joint consideration of aleatory and epistemic components through Monte Carlo simulation procedures may be the best approach to handle uncertainties in a more flexible and powerful way when dealing with low probabilities. This alternative approach allows an efficient sampling of the parameter space as well as the direct treatment of the resulting ground motion amplitudes using extreme-value statistics.

6.0 LANDSLIDES

6.1 General description

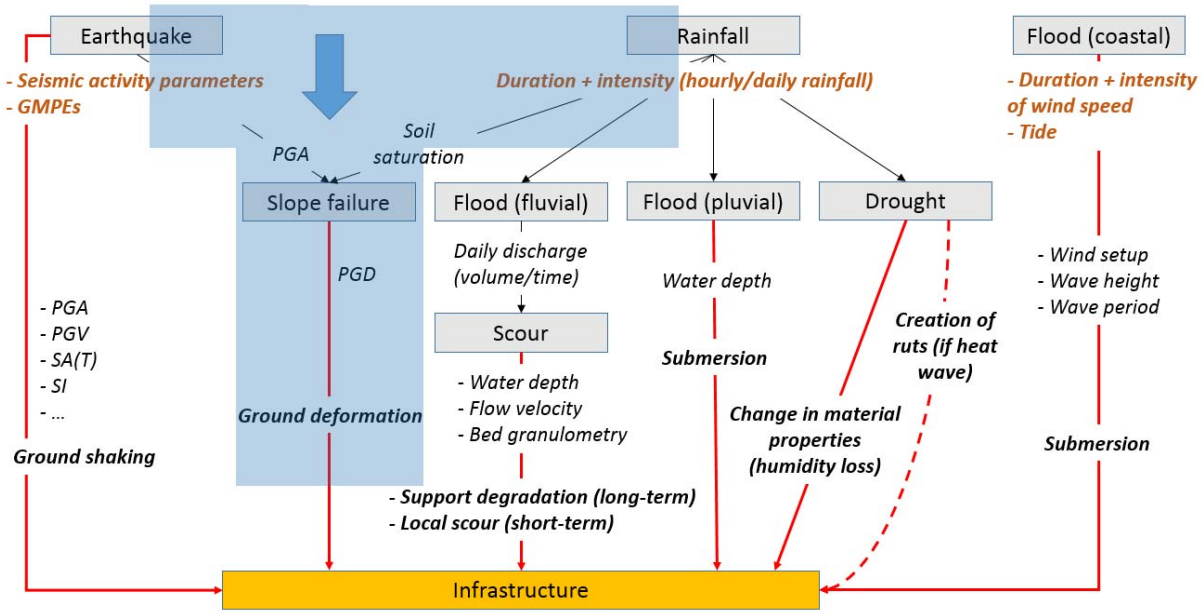

Figure 14: Synthesis of considered hazards and their corresponding IMs. Earthquake- and rainfall-induced landslide hazard corresponds to the branch with grey background, the blue arrow pointing at it.

A landslide has been defined as 'a movement of mass of soil (earth or debris) or rock down a slope' (Courture, 2011). This broad definition includes both slow and fast moving debris flows, rockfalls and permanent ground deformations resulting from earthquake ground movement. Landslides occur throughout the world, under all climatic conditions and terrains, cost billions in monetary losses, and are responsible for thousands of deaths and injuries each year (Highland & Bobrowsky, 2008). For example, in May 2014, a series of heavy rainfall induced landslides struck in the Argo district of Badakhshan in Northeastern Afghanistan, causing a significant loss of life and widespread damage to homes and agriculture. The landslides affected over 17,000 families and caused 155 deaths (OCHA, 2014). These landslides were triggered by long periods of heavy rainfall in the previous months. The 2008 Wenchuan earthquake in China caused more than 15,000 geohazards in the form of landslides, rockfalls, and debris flows which resulted in about 20,000 deaths (Yin, et al., 2009). From these two examples, it is noted that mass movements or landslides can be treated as induced hazards which can be triggered by the main hazard sources. For the purpose of the INFRARISK project, rainfall and earthquakes are considered as the main hazard sources. Therefore, two separate models are required that relate landslide hazard to the source event; a rainfall-triggered landslide hazard model and an earthquake-triggered landslide hazard model. It is noted here that the landslide risk analysis will be carried out on road sections built on or under slopes. Therefore, it should be highlighted that, although for the purpose of analysis of risk to infrastructure, landslides are here treated as hazards, the models describing their occurrence, are essentially slope fragility curves.

There are a number of different landslide types that can occur depending on the type of slope and triggering factor. Cruden and Varnes (1996) proposed the taxonomic classification outlined in Table 8. In order to measure the impact of a landslide, an intensity measure is required. There is no

universal landslide intensity measure available as it depends on the landslide type. Table 8 details a list of suitable landslide intensity measures for the various landslide types.

Table 8: Taxonomic classification of landslides (Cruden & Varnes, 1996)

Landslide Type	Description of Movement		Intensity Measure
Slides	Slides are mass movements characterized by a distinct zone of weakness that separates the sliding portion from the more stable underlying material.		Permanent Ground Deformation (PGD) Volume
Rockfalls	Falls are abrupt movements of rock masses that become detached from steep slopes of cliffs.		Volume
Topples	Topples are distinguished by the forward rotation of a rock/soil unit or units about some pivotal point below or low in the unit		Volume
Flows	Debris flows	A rapid mass movement in which a combination of loose soil, rock, organic matter, air and water mobilize as a slurry and flow downslope	Volume×Velocity
	Debris Avalanche	A very rapid mass movement of non-saturated material which remains laterally unconfined and unchannelled along most of its length.	Volume×Velocity
	Earthflow	An intermittent flow-like movement of plastic clayey earth. Flows of both saturated and dry material are possible.	Volume×Velocity
	Mudflow	An earthflow of material wet enough to flow rapidly and containing at least 50% sand, silt and clay sized particles.	Volume×Velocity
	Creep	A slow steady downward movement of slope-forming soil or rock.	Permanent Ground Deformation
Lateral Spreads	A mass movement dominated by lateral extension and accompanied by shear or tensile fractures, as usually occur on very gentle slopes or flat terrains.		Permanent Ground Deformation

Landslide hazard assessment has played an important role in developing land utilization regulations aimed at minimizing the loss of lives and damage to property (Motamedi & Liang, 2013). Furthermore, it can be used in order to prioritize risk mitigation measures and retrofit strategies. Varnes (1984) defined landslide hazard as the probability of occurrence of a potentially destructive landslide within a specified period of time and within a given geographical area. Guzzetti et al. (1999) modified this definition to incorporate landslide magnitude, as expressed below:

$$H = P[M \geq m] \quad (15)$$

where *H* is the landslide hazard value (0-1)/year, *M* is the landslide magnitude and *m* is a specified magnitude for a given time period, a given location and given preparatory factors. The preparatory

factors in the equation refer to all of the specifics of the area, including geology, geometry, and geotechnical properties. It is worth noting that although this definition of landslide hazard includes a prediction of landslide size, the majority of landslide hazard assessments described in the literature do not include a prediction of landslide size. Magnitude-frequency relations (M-F curves) give landslide occurrence probabilities of events equal to or greater than a certain magnitude (Corominas et al, 2014). Several possible IMs can serve to describe the magnitude of landslide event. The most commonly used are landslide volume, displacement, velocity or kinetic energy, the choice depending on the landslide type. The development of M-F curves is usually difficult due to limited data and other restrictions (Corominas et al, 2014). The difference between landslide hazard and susceptibility should be highlighted here. Landslide susceptibility is the likelihood of a landslide occurring in an area on the basis of local terrain conditions (Brabb, 1984). Landslide susceptibility does not consider the temporal probability of failure or the magnitude of the expected landslide. Landslide hazard on the other hand, is the probability of occurrence of a landslide of given magnitude within a specified period of time (IAEG Commision on Landslides, 1990).

Landslide hazard methods can be divided into two categories: statistical methods and geotechnical approaches (Aloetti & Chowdhurry, 1999). Statistical methods, such as bivariate or multivariate statistical analyses, quantify the relationships between landslide occurrences and related factors, such as soil type, land use, slope geometry, vegetation and parent material (Park, et al., 2013). Statistical landslide hazard assessments are therefore eminently empirical in nature, and require a landslide inventory or knowledge of previous landslides to predict future occurrence. Guzzetti et al. (2005) proposed a probabilistic model to determine landslide hazard using a landslide inventory. The model predicts the location, frequency and magnitude of landslides at a basin scale. The method prepares a multi temporal inventory map through the interpretation of multiple sets of aerial photographs taken over a given time period. The inventory map is then divided into mapping units and based on the landslides inventoried in each unit; the exceedance probability of having one or more landslides is obtained for different periods. The probability of landslide size is estimated by analysing the frequency‑area statistics of landslides, obtained from the multi-temporal inventory map. Unfortunately, this type of approach requires comprehensive multi-temporal landslide databases, which are rarely available in practice (Jaiswal, et al., 2010). Figure 15 shows the degree of completeness of landslide databases in Europe. From the figure it can be seen that the majority of European countries have databases that are less than 50% complete.

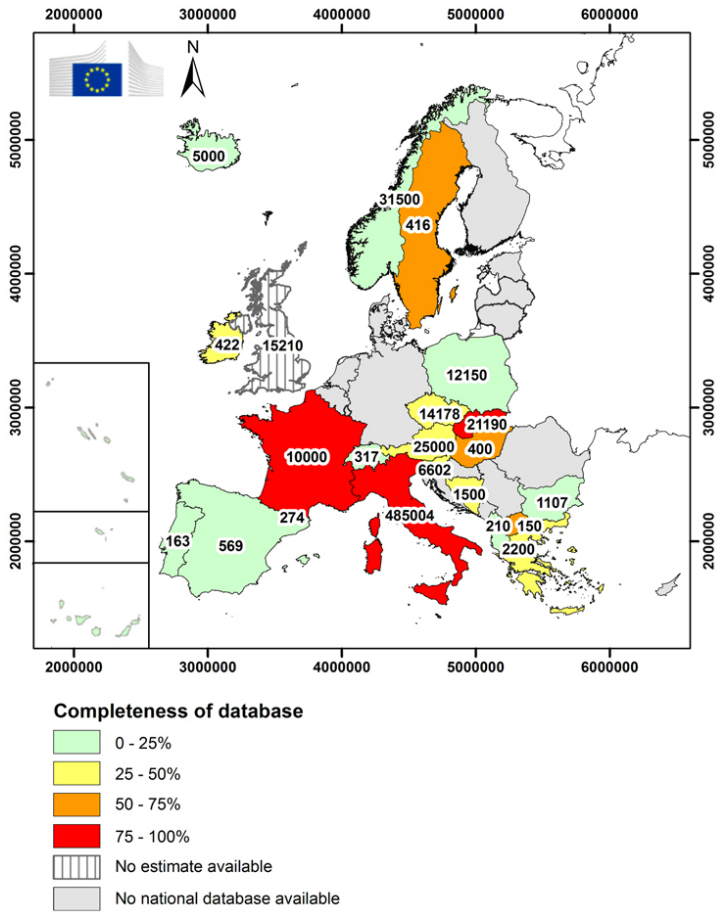

Figure 15: Number and estimated completeness of landslide locations in national (n = 24) landslide databases in Europe (Van Den Eeckhaut & Hervás, 2012)

A landslide hazard assessment can also be carried out using a geotechnical approach. The geotechnical approach analyzes the mechanical condition of slopes and evaluates their stability using mathematical calculations (Park, et al., 2013) and a probabilistic distribution of the parameters. This approach, relying on analytical methods, is the one adopted in this study.

6.2 Intensity Measures

Intensity measures used in the development of fragility curves are typically derived from the loading on the structure (Schultz, et al., 2010). In the INFRARISK project, a slope (critical rail and road cuttings and embankments) is considered as a piece of infrastructure rather than a hazard source. Therefore, an environmental load characteristic like rainfall intensity and duration could be used as an intensity measure for rainfall-triggered landslides. However, since the INFRARISK project accounts for both rainfall-triggered and earthquake-triggered landslides, in addition to other hazard types like floods and earthquakes, a need for consistent type of intensity measure exists. The effects of rainfall intensity and duration can have different effects on slopes located very close together because of variation in slope angle, aspect, vegetation etc. Flooding which is also considered in the INFRARISK project can also contribute to increased water content and, therefore, reduced strength in a slope. Therefore, the intensity measure adopted in the project is the degree of saturation of the near surface soil. As rainfall percolates into a slope the near surface suctions reduce and the degree of

saturation rises, this is a therefore a good reflector of the current and antecedent rainfall patterns experienced by the slope.

The infiltration process leads to the development of relatively shallow planar slope failures surfaces parallel to the slope to develop (Fourie, et al., 1999). These failures are often observed in man-made slopes, i.e. road and rail embankments, which justifies the use of the infinite slope model adopted for the landslide hazard analysis in the INFRARISK project. This model is described in Section 6.4.2 of this deliverable.

Therefore, precipitation will be used as the intensity measure for rainfall-triggered landslides. The three parameters shown below will be accounted for in the intensity measure adopted. The exact combination is discussed in Deliverable 3.2.

- The antecedent rainfall (e.g. rainfall in previous month which describes approximately the degree of saturation of the slope [mm/h]);
- Rainfall intensity [mm/h];
- Rainfall duration [h];

Earthquake-triggered sliding events are the second type of landslide considered in this study. This type of landslide involves the sliding of a certain depth of soil away from the stable ground below. This type of landslide can affect a road section in two ways, depending on whether the slide happens above or below the road section. If the slide happens above the road section, as shown in Figure 16, the displaced ground could block the roadway. An example of this occurred following the Niigata-Cheutsu Oki, Japan Earthquake in 2007 where a shallow translational landslide occurred on a steep natural slope along the road connecting the towns of Kashiwaza and Kariwa. The landslide blocked a major road and prevented access, Figure 17 (Saygili, 2008; Kayen, et al., 2007). If the slide happens below the road section, as shown in Figure 16, the road surface may become damaged.

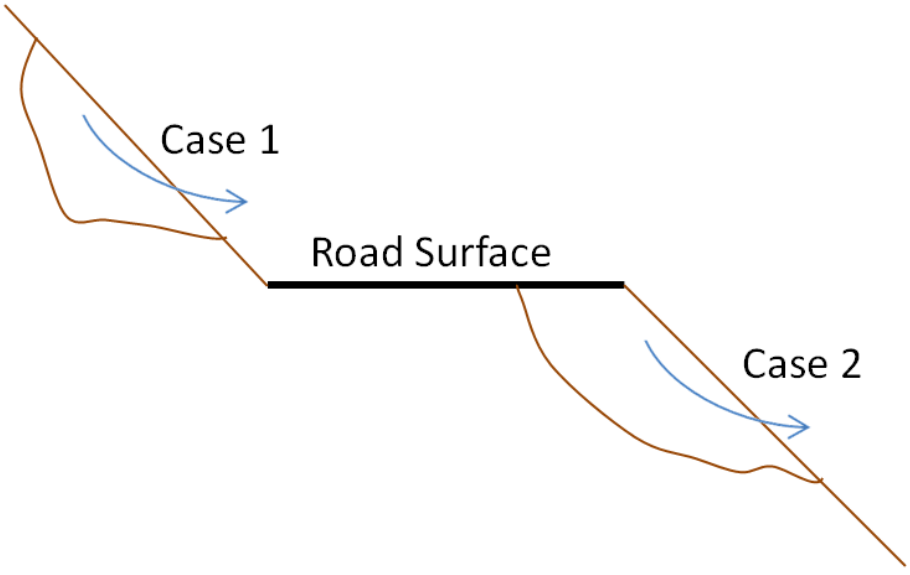

Figure 16: Two examples of sliding mechanisms that can cause damage to a road along a slope

Figure 17: Landslide following the Niigata-Cheutsu Oki, Japan Earthquake 2007 (Kayen, et al., 2007)

For earthquake-induced landslides, either Permanent Ground Deformation (PGD) or Peak Ground Acceleration can be used as the intensity measure (Safeland, 2011). However, as mentioned previously, in this project we adopt the approach that a road or rail line built on a slope or an embankment is considered as an infrastructure component rather than a hazard source. Therefore, it is more appropriate to use PGA as the intensity measure for the landslide hazard model. This is consistent with the rainfall induced landslide hazard model developed herein, which uses the rainfall intensity as the landslide intensity measure.

It must be noted that the landslides mentioned here are only two of a number of landslide types that can occur on slopes. However, the hazard assessment methods for landslides such as debris flows and rockfalls available in the literature require large amounts of empirical data and are, therefore, not applicable to regions where this data is unavailable. If landslide intensity is to be predicted in a quantitative manner, in situations with little data, only types of landslides for which analytical methods are available, and hence of generic applicability, irrespective of location and available data.

6.3 Spatial scale of analysis

For both the earthquake-triggered landslide hazard model and the rainfall-triggered landslide hazard model, the spatial scale of the analysis can be local. In this case each slope to be included in the analysis will go through an independent check to determine the probability of failure, since the slope geometry and soil parameters play a crucial role in the model. Various sections of the same embankment or cutting might have substantially different probabilities of failure depending on their slope angle, variability of soil parameters etc. Depending on the homogeneity, the asset (slope under consideration) could stretch for several hundred meters, although typically there will be much larger

number of shorter asset lengths. A local spatial analysis is a common approach due to the heterogeneity issues present.

For the earthquake-triggered landslide hazard model the triggering event is the seismic ground motion. The earthquake models described in Section 5 have associated GMPEs for PGA and PGV. Based on this model, a shake map can be produced which shows the spatial variation in earthquake intensity across a geographic area. The spatially distributed earthquake intensity will be used as input for the earthquake-triggered landslide hazard model. The spatial distribution of the soil saturation ratio must also be considered as it is a required input for the landslide hazard model. For the current study, this will be derived from precipitation information and judgment, however, a more rigorous hydraulic analysis can also be used (Saygili, 2008). When carrying out a landslide fragility analysis on an infrastructure component, the spatial scale of the analysis must be decided. For example, if a 1 km stretch of road is being assessed, the road should be discretized into smaller sections so that a unique fragility analysis can be carried out on each section. It is recommended that this value of length should be linked to the characteristic width of the landslide under consideration.

For the rainfall-triggered landslide hazard model, rainfall infiltration analysis is of crucial importance. A relatively simple but accurate model will be needed in order to maintain the complexity and the computational requirements of the landslide hazard model in the IDST at a suitable level. For that reason, a straightforward 1-D analytical infiltration model such as Green-Ampt (Green & Ampt, 1911) or Horton (Jury & Horton, 2004) has an advantage over the more complex 2D or 3D models (e.g. Richard's equations and/or FE analyses). Some enhanced and modified 1D infiltration models have shown very good estimates compared with complex FE analyses and site tests (Gavin & Xue, 2008).

Although rainfall occurs over relatively large geographic areas, zones with identical rainfall intensity and duration tend to be quite localized. Because of variations in topography (slope angle, aspect etc.) and soil conditions, failure probabilities also tend to vary over relatively small scales. The spatial variation of parameter values will therefore determine the spatial scale of the landslide. Landslide run-out is governed by the topography downslope, which is of importance for the infrastructure positioned under the unstable slope. For the type of linear network elements considered in INFRARISK, the assets (road and rail track) are situated either directly on embankments or immediately adjacent to cuttings and landslides which affect these structures are typically very localized occurring within meters of the road or rail line or within the asset (slope) itself, as seen in Figure 17. Run-out modelling could only prove beneficial in the case of high-mobility debris flows originating on natural slope some distance uphill from the infrastructure elements. For these reasons, this will not be explicitly considered in the overarching methodology for INFRARISK.

6.4 Methodology

6.4.1 Earthquake-Triggered Landslide Hazard

Recent earthquakes such as the 2008 Wenchuan earthquake in China have shown that earthquake-induced landslides are a significant secondary seismic hazard. The seismic performance of slopes is typically evaluated based on the sliding displacement predicted to occur along a critical sliding surface (Rathje, 2013). This displacement represents the cumulative downslope movement of a sliding mass due to earthquake shaking, measured as peak ground deformation (PGD). The rigid sliding block approach, first proposed by Newmark (1965), is adopted in numerous studies to

estimate the yield acceleration of a slope (Jibson, et al., 2000; McCrink, 2001; Saygili & Rathje, 2009). The yield acceleration of a sliding block represents the horizontal accelation that results in a factor of safety equal to 1.0 for the slope and this acceleration level initiates sliding (Saygili & Rathje, 2009). The yield acceleration can be derived using an infinite slope model, as shown in Figure 18,and is a function of multiple slope characteristics, as shown in Table 9 (Saygili & Rathje, 2009). Earthquake induced displacements are expected if the Peak Ground Acceleration (PGA) of the earthquake exceeds the yield acceleration.

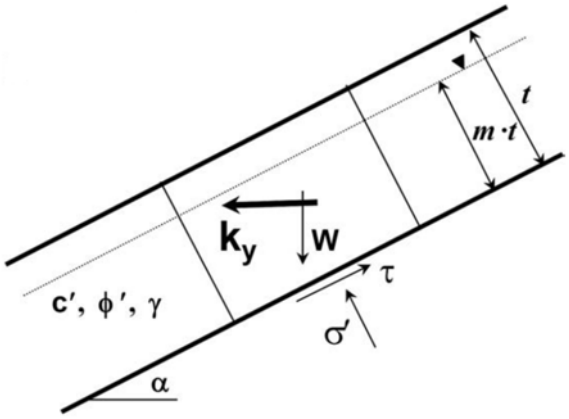

Figure 18: Infinite slope representation used to define k_y (Saygili & Rathje, 2009)

In order to carry out an earthquake induced landslide hazard analysis, information is required about the yield acceleration of the relevant slopes and the seismic hazard in the region. Using the infinite slope model shown in Figure 18, k_y can be explicitly described as (Saygili & Rathje, 2009):

$$k_y = \frac{(\mathrm{FS}-1)g}{(\tan\varphi'+1)/\tan\alpha} \quad (16)$$

$$\mathrm{FS} = \frac{c'}{\gamma \cdot t \cdot \sin\alpha} + \frac{\tan\varphi'}{\tan\alpha} - \frac{\gamma_w \cdot m \cdot \tan\varphi'}{\gamma \cdot \tan\alpha} \quad (17)$$

where k_y is the yield acceleration in the horizontal direction in units of g (g = acceleration due to gravity), FS is the static factor of safety, α is the slope angle, φ' is the effective internal friction angle of the soil, c' is the effective cohesion of the soil, γ is the unit weight of the soil, t is the failure surface depth normal to the slope, γ_w is the unit weight of water and m is the percentage of failure thickness that is saturated (i.e. saturation ratio). The input parameters required to estimate k_y can be seen in Table 9, along with recommendations as to how the parameters should be estimated. Values for k_y should be estimated across the study area at suitable intervals producing a landslide susceptibility map. The expected level of shaking must be accounted for to carry out a full hazard analysis.

Table 9: **Parameters used to estimate k_y**

Parameter	Source
Slope Angle (α)	Digital Elevation Model
Effective Cohesion (c')	Geologic maps and geological data
Internal Friction Angle (φ')	Geologic maps and geological data
Unit weight (γ_w)	Typically assumed
Failure surface thickness (t)	Typically assumed
Saturation ratio (m)	Derived from precipitation information and judgment

In order to calculate the sliding displacement of a rigid sliding mass, an analytical or empirical approach can be adopted. Using an analytical approach, a suite of recorded acceleration time-history ground motions can be selected and numerically integrated for the sliding episodes that initiate when k_y is exceeded in the destabilizing direction (Rathje, et al., 2013). Numerous empirical models have been developed in the literature. In this report two empirical models proposed by Saygili and Rathje (2008) and Rathje and Saygili (2009) are presented. These models were developed from displacements computed using over 2,000 recorded motions from the Next Generation Attenuation (NGA) database (Rathje, et al., 2013). The first model presented here uses a single ground motion parameter (PGA) and the earthquake magnitude (M) to predict the sliding displacement and is therefore referred to as a scalar model. This second model uses two ground motion parameters (PGA, PGV) and is therefore referred to as a vector model. These models predict displacement in cm and assume a lognormal distribution for displacement (Rathje, et al., 2013).

Scalar Model:

$$\ln D = a_1 + a_2\left(\frac{k_y}{\text{PGA}}\right) + a_3\left(\frac{k_y}{\text{PGA}}\right)^2 + a_4\left(\frac{k_y}{\text{PGA}}\right)^3 + a_5\left(\frac{k_y}{\text{PGA}}\right)^4 + a_6 \ln \text{PGA} + a_7(\text{M}-6) \quad (18)$$

$$\sigma_{\ln D(\text{PGA,M})} = 0.73 + 0.79\left(\frac{k_y}{\text{PGA}}\right) - 0.54\left(\frac{k_y}{\text{PGA}}\right)^2 \quad (19)$$

Vector Model:

$$\ln D = a_1 + a_2\left(\frac{k_y}{\text{PGA}}\right) + a_3\left(\frac{k_y}{\text{PGA}}\right)^2 + a_4\left(\frac{k_y}{\text{PGA}}\right)^3 + a_5\left(\frac{k_y}{\text{PGA}}\right)^4 + a_6 \ln \text{PGA} + a_7 \ln \text{PGV} \quad (20)$$

$$\sigma_{\ln D(\text{PGA,PGV})} = 0.41 + 0.52\left(\frac{k_y}{\text{PGA}}\right) \quad \sigma_{\ln D(\text{PGA,PGV})} = 0.41 + 0.52\left(\frac{k_y}{\text{PGA}}\right) \quad (21)$$

Both probabilistic and deterministic approaches are used to evaluate permanent ground displacement hazard in the literature (Rathje, et al., 2013). However, Rathje et al. (2013) suggest that in practice, engineers generally consider a ground motion amplitude at a given hazard level and then make a deterministic prediction of displacement, rather than evaluating a displacement associated with a given hazard level. This approach is adopted in this project since landslides are considered secondary hazards in the methodology and therefore hazards curves are only developed for the seismic hazard. In order to account for some uncertainty in the displacement prediction, an

upper bound displacement is considered. Rathje et al. (2013) carried out a study investigating the difference between probabilistic and deterministic displacements for a range of k_y values using the ground motion hazard at 12 sites in California. The aim of the study was to recommend a level of epsilon (i.e. ε_D = number of standard deviations) required for the deterministic approach to predict displacements similar to the probabilistic approach. The values of ε_D can be used as shown in Equation (21) to predict hazard-consistent levels of displacement (Rathje & Saygili, 2011):

$$D_{\text{hazard-consistent}} = \exp\left[\ln D_{\text{median}} + \varepsilon_D \cdot \sigma_{\ln D}\right] \quad (22)$$

In Equation (21), the median displacement is found using Equations (17) and (19) and the ground motion values derived from PSHA. The standard deviation is found using Equations (18) and (20). Rathje & Saygili (2011) found that ε_D varied with k_y/PGA, as shown in Figure 19.

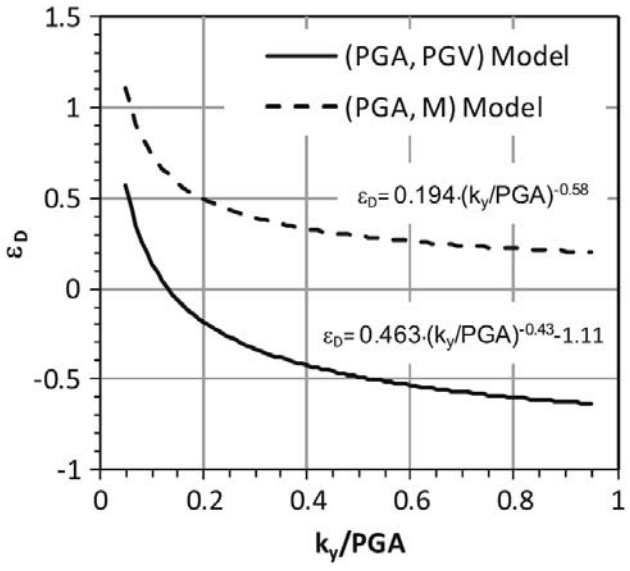

Figure 19: Recommended ε_D to use in deterministic displacement analyses to generated displacements consistent with probabilistic analyses (Rathje, et al., 2013)

In order to carry out a landslide risk assessment, an estimate of road damage is required for a given PGD. Fragility curves are a useful tool that provide the probability of a given damage state occurring for a given intensity measure. As mentioned previously, PGA is used as the intensity measure in this study. Safeland (2011) developed landslide fragility curves in terms of PGA and k_y for both major and urban roads. This approach takes into account the soil characteristics and the local topography when estimating damage to a road. Safeland developed these fragility curves based on existing HAZUS fragility functions for roads (NIBS, 2004), as shown in Figure 20 for highways and major roads respectively. These are the only fragility curves available in the literature for estimating the vulnerability of roads due to landslides (Safeland, 2011). However, they have shown a realistic assessment of the expected damage level in most cases (Azevedo, et al., 2010). Using the predictive models shown in Equations (17-20), the existing HAZUS curves are modified to produce fragility curves in terms of both k_y and PGA. These fragility curves are developed in Deliverable 3.3 'Fragility Functions Matrix'.

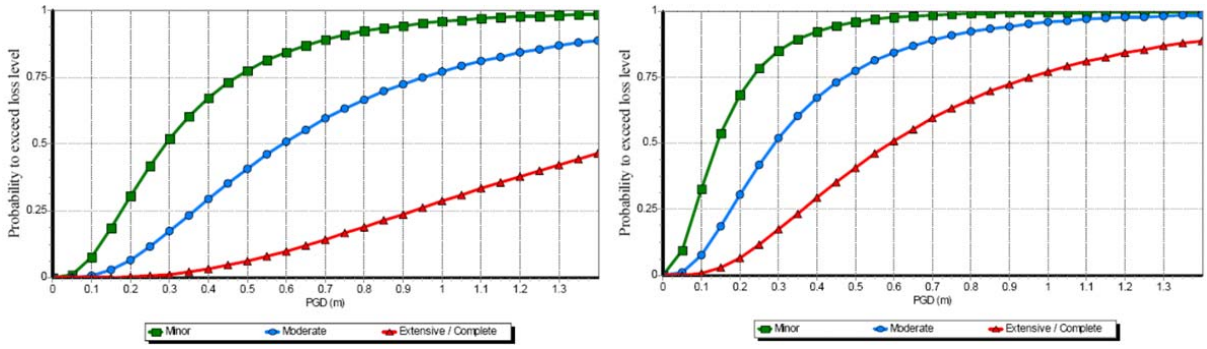

Figure 20: Landslide fragility curves at various damage states for highways (left) and urban roads (right), from (NIBS, 2004)

6.4.2 Rainfall-Triggered Landslide Hazard

In embankments and other engineered fills placed above the water table level, the water table is usually at great depth. The near surface soils experience negative pore-water pressure (suction), which contributes greatly to the overall slope stability. Many slope failures have been recorded that occurred during or shortly after rainfall, as water infiltrates into the slope reducing near surface suction. Given changing climatic conditions (increasing and more intense rainfall events), landslides are becoming much more prevalent across transport networks. In addition to the risk posed to life by rapid landslide events, additional problems are caused by the interruption of transport routes (Gavin & Xue, 2008).

The translational (planar) failure mechanism assuming an infinite slope model, shown in Figure 21, has been shown to be the most appropriate model for describing shallow landslides. Landslides that have a small depth relative to their length and a wetting front depth of less than 2 m (see Figure 21) are referred to as shallow landslides. The model is similar to that adopted for earthquake induced landslides.

Regarding the possibility of accounting for rotational slope failures, a certain level of consistency and standardization between earthquake- and rainfall-triggered models has to be reached: therefore the emphasis is put on translational slip models. Furthermore, climate change issues, which are emphasized in INFRARISK, have much a larger effect on translational slope failures (Gavin & Xue, 2008).

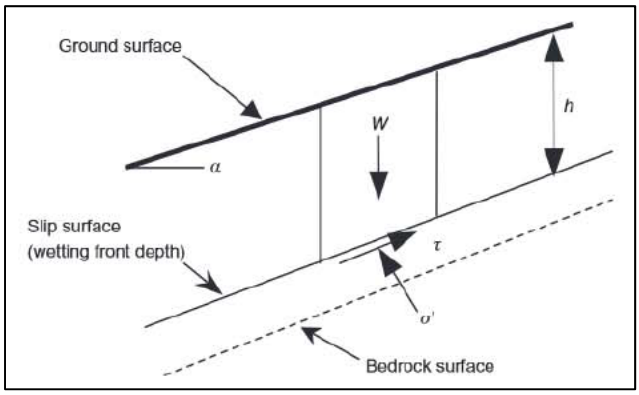

Figure 21: Infinite Slope Model (Gavin & Xue, 2008)

The Factor of safety (FS) is described using the following model, with the effect of the suction and effective cohesion included as the total cohesion, *C*:

$$\mathrm{FS} = \frac{C + \gamma \cdot h \cdot \cos^2 \alpha \cdot \tan \varphi'}{\gamma \cdot h \cdot \cos \alpha \cdot \sin \alpha} \quad (23)$$

$$C = c' + (u_a - u_w) \cdot \tan \varphi^b \quad (24)$$

where c' is the effective cohesion, u_a is the pore-air pressure on the failure plane, φ' is the angle of internal friction associated with the net normal stress state variable ($\sigma_n - u$), u_w is the pore-water pressure on the failure plane, (u_a - u_w) is the metric suction on the failure plane, and φ^b is the angle indicating the rate of increase in shear strength relative to the matric suction.

These suctions in the soil are transient and reduce as water percolates into the slope (and a wetting front develops) during periods of heavy or prolonged rainfall. The spatial and temporal movement of the wetting front and subsequent change of suction values can be calculated using different infiltration models for unsaturated soils. For this class of problem consideration of infiltration is essential and the model represents a step forward from the other rainfall-triggered landslide hazard models found in the literature (Liener 2008, Park 2013), which mainly target natural slopes and do not account for the effect of soil suction.

On long, linear transport networks such as roads and railways, key input parameters such as c' and φ' are spatially varied. Proper statistical descriptions of these parameters within a probabilistic calculation model are essential to obtain reasonable estimates of slope safety. The most common probabilistic method which is applied to slopes in the literature is Monte Carlo Simulation. However, the infinite slope model can also be expressed as a simple limit state expression; therefore, the probability of failure can be obtained with the other probabilistic tools, namely FORM, FOSM or a genetic algorithm.

The probabilistic calculation will result in probabilities of failure for series of landslide areas and depths, and give information on the spatial extent and volume of the sliding body. The landslide volume affecting the infrastructure element is directly correlated to the damage and the usability of the element. This issue will be further addressed in Task 3.2 where families of fragility curves will be developed on the basis of probabilistic calculations described here.

One state of the art example of relevance was produced in the Safeland project - deliverable D2.5 (Safeland 2011, Smith J. et al. 2013), concerning the physical vulnerability of roads to debris flows. In this work the expected volume of debris affecting a road was correlated with road damage level and usability through fragility curves, as seen in Table 10 and Figure 22.

Table 10: Damage state definitions (from Safeland, 2011)

Damage State	High Speed Roads	Local Roads
P1 (Limited damage)	Encroachment limited to verge/hardstrip	Partial blockage of carriageway
P2 (Serious damage)	Blockage of hardstrip and one running lane	Complete blockage of carriageway and/or damage to ancillaries
P3 (Destroyed)	Complete blockage of carriageway and/or repairable damage to surfacing	Complete blockage of carriageway and/or damage to surfacing. For unpaved roads the surfacing may remain damaged but passable at reduced speeds post clean-up

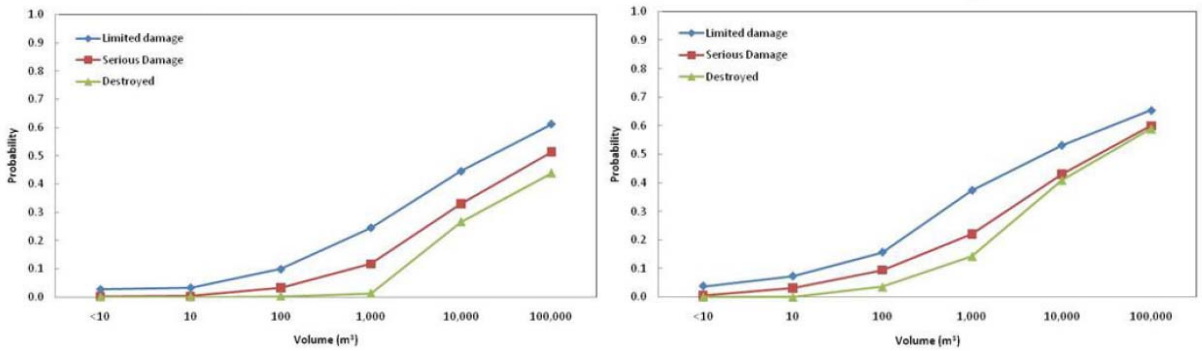

Figure 22: Fragility curves for the impact of debris flow on road segment, high speed road (left), local roads (right), from EU SAFELAND project deliverable 2.5

The probabilities for a level of damage exceedance for a given volume of debris flow used in the Safeland (2011) study were derived empirically from a questionnaire sent to 47 experts. The INFRARISK approach will thus be a step forward by implementing quantitative geotechnical calculations in obtaining correlations between landslide body volume and damages to linear network infrastructure elements.

6.5 Conclusions

Landslide hazard assessment is an extremely complex task with multiple sources of uncertainty. Two landslide hazard models were outlined in this section, namely an earthquake-induced landslide hazard model and a rainfall-induced landslide hazard model. Both of these models used a geotechnical approach since statistical methods require extensive landslide inventories that are rarely available in practice.

The earthquake-induced landslide hazard model is capable of predicting PGD as a function of PGA. This model depends heavily on the soil and topography characteristics listed in Table 9 and therefore these need to be estimated carefully. Based on the predictive model for PGD, road section fragility curves will be developed in Deliverable 3.2 that provide the probability of reaching a defined level of road damage for a given level of earthquake ground shaking and ground conditions.

The rainfall model is capable of predicting the occurrence of a slip and the failure volume either as a result of a given rainfall event or as a change in the degree of saturation or suction in a slope. Because of the inclusion of infiltration (either directly or indirectly) the method represents a significant improvement on the state of practice in hazard assessment.

7.0 FLOODS

7.1 General description

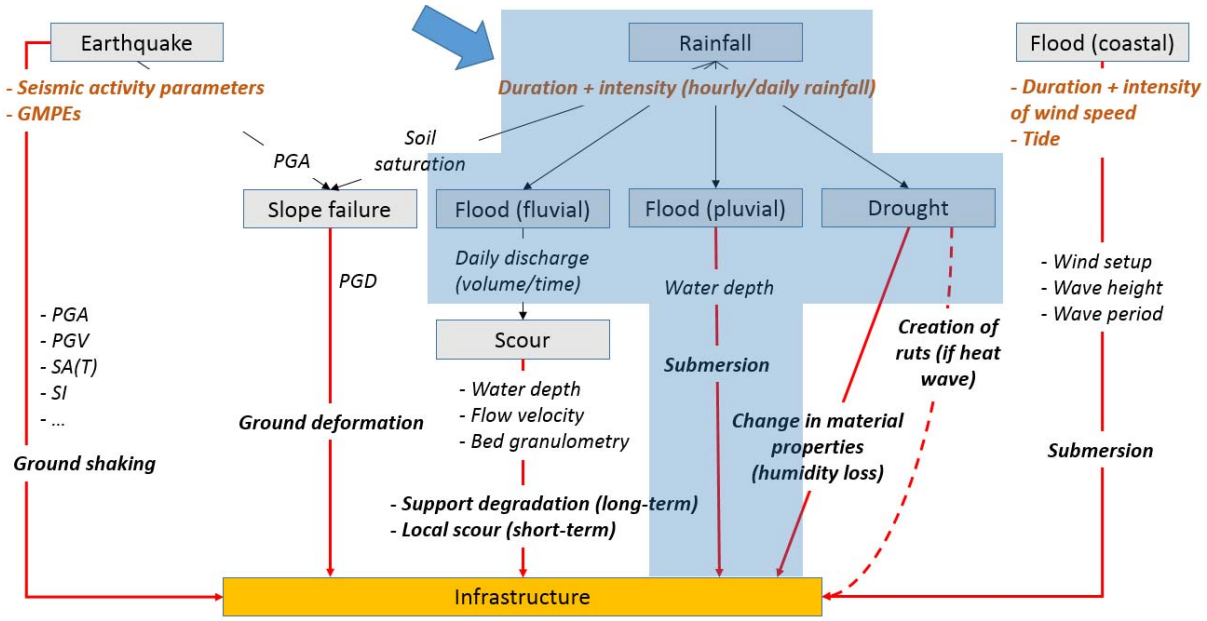

Figure 23: Synthesis of considered hazards and their corresponding IMs. Fluvial and pluvial flood hazard corresponds to the branch with grey background, the blue arrow pointing at it.

Flood is a hazard that is usually defined as a rise in water level that cause an overflow of inland and/or tidal waters onto normally dry land areas: 512 floods occurred in Europe in the last 50 years with a total damage of 98.562 million euro (Guha-Sapir et al., 2009). Two types of flood hazard are considered in this chapter: coastal and rainfall related. Rainfall over extended periods of time and an extended area and/ or with high intensity can cause the river level to rise and overflow the river banks that is called a fluvial flood.

Pluvial or surface flood occurs when the rainwater cannot be absorbed by the storage area (ground, canals, lakes, rivers, etc.) and flows directly over the surface. It is usually caused by storm events with high rainfall intensities ("tropical").

Drought is a hazard and can be defined as deficiency of water over extended period of time. In the last 50 years, 41 droughts were registered in Europe, with a total damage of 32.749 million euros (Guha-Sapir et al., 2009). There are five main types of droughts (Tate and Gustard, 2000): meteorological (rainfall deficiency), hydrological (deficiency in water flow), agricultural (deficiency of soil moisture), groundwater drought (deficit in groundwater storage), operational drought (conflict of water shortage and water management demands). In INFRARISK the first type of drought (rainfall deficient) is considered. The drought may also lead to soil erosion, dust storms, etc.

Regarding the floods (and drought) hazard estimation, deterministic and probabilistic approaches can be identified. The probabilistic approach is based on the estimation of the probability of occurrence of events exceeding a certain intensity with an estimated frequency within a given period of time. Section 2 on probabilistic methodologies is used to analyse pluvial, fluvial and coastal flood related hazards based on empirical data.

7.1.1 Effect of climate change

In the work of Feyen et. al. (2012) the fluvial flood risk under two climate scenarios (high SRES A2 and low B2 emission) were investigated for Europe. Their results indicate an increase in extreme river discharge for some of the countries such as Belgium, Denmark, France, Germany, Ireland, Luxembourg, the Netherlands and the United Kingdom (Figure 24). It leads to an increase in flood damage in these countries and makes flood hazard assessment an important task.

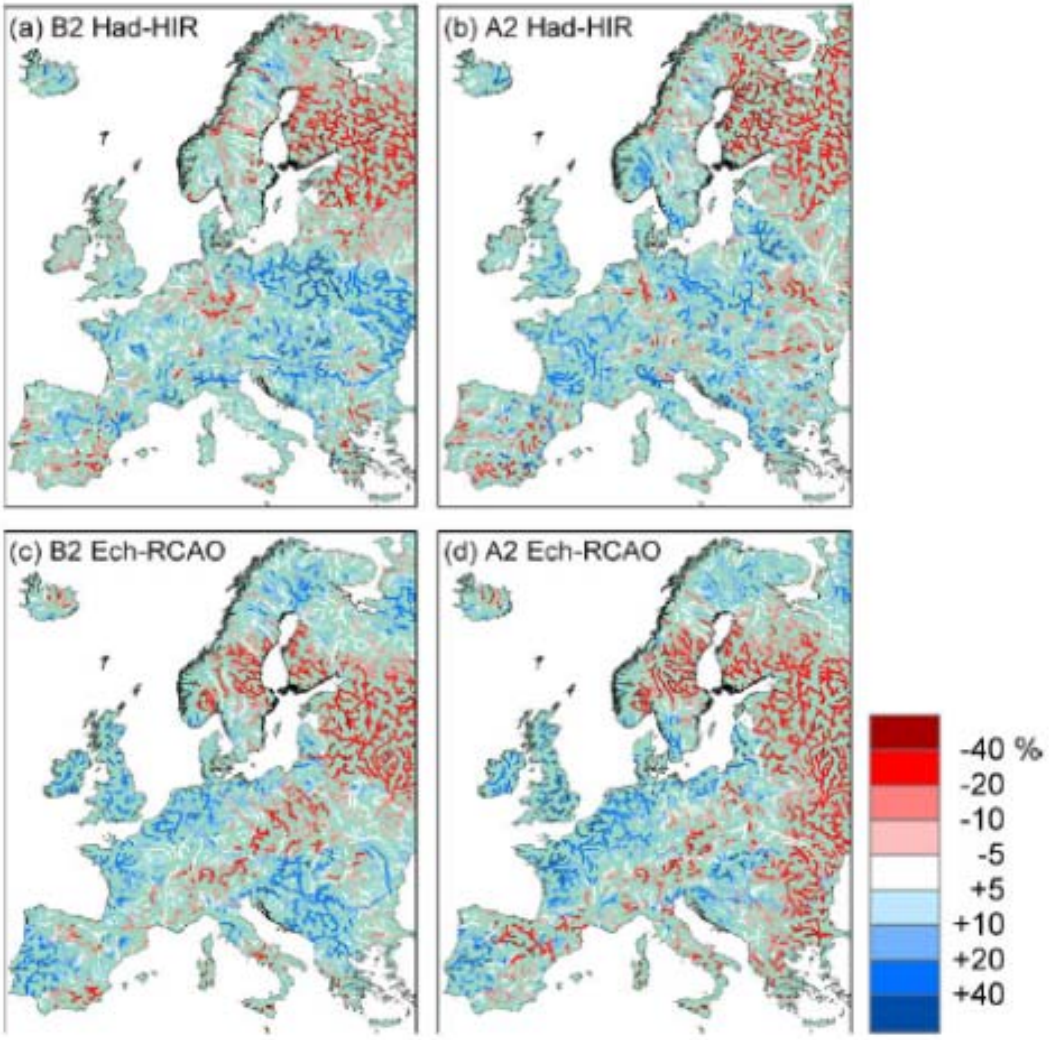

Fig. 1 Relative change in 100-year return level of river discharge between scenario (2071–2100) and control period (1961–1990) for climate scenarios B2 Had-HIR (a), A2 Had- HIR (b), B2 Ech-RCAO (c) and A2 Ech-RCAO (d). Shown here are only rivers with an upstream area of 1,000 km^2 or more (from Dankers and Feyen 2009)

Figure 24: Relative change in flood return levels (Dankers and Feyen, 2009)

Although different climate scenarios show differences in future prediction of precipitation change, the precipitation intensity is projected to increase over many areas (Christensen and Christensen 2003; Kundzewicz et al. 2006). Maguire and Falconer (2011) projected an increase in frequency of pluvial and flash flooding in several countries of Europe (Figure 25).

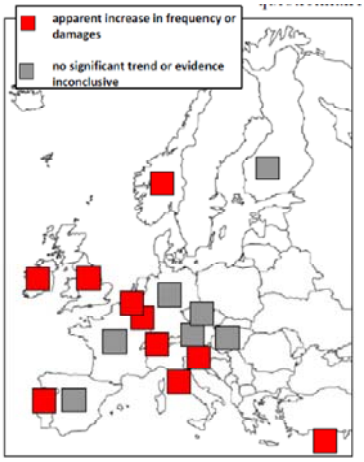

Figure 25: Trend in Frequency of Pluvial and Flash Flooding Across Europe (Maguire and Falconer, 2011)

Coastal flood hazards can be also recognized as a growing threat over Europe. Recent studies provide an evidence that the sea level rise increased from the 19th to the 20th century (Bindoff et al.,2007; Goennert and Ferk, 1996 in: Sterr, 2008; Devoy, 2008). Under the future climate change scenarios it is considered likely to witness significant extreme wave height rises along the western European coast (Debernard and Roed, 2008; Grabemann and Weisse, 2008) and declines in extreme wave height in the Mediterranean Sea (Lionello et al., 2008). It means that northern European countries have to face the risk of this hazard in the long term (Figure 26, source: "This is climate change in Europe", published in November 2013 by Climate Action Network Europe, Brussels, Belgium).

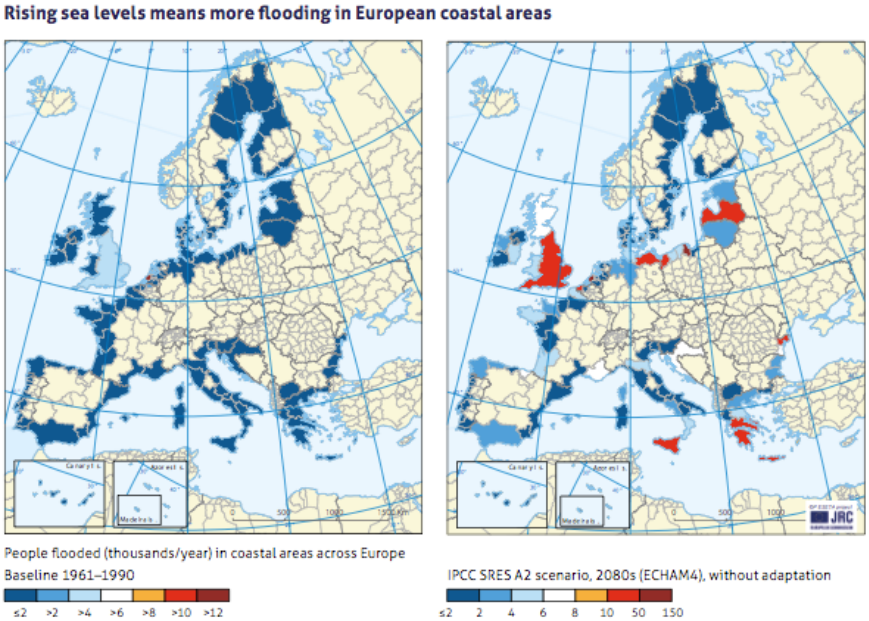

Figure 26: Coastal flood projections (Climate Action Network, 2013)

Finally, many studies concluded that further increase in droughts is expected, in particular for Southern European areas (IPCC, 2001; Watson et al., 1997).

7.2 Intensity measures

Common intensity measures to be considered for the different flood events are the following:

- Rainfall *R* in [mm/h], as a function of time and space;

- Discharge *Q* in [m3/s], as a function of time and space;

- Water level *h* in [m above MSL] (mean sea level), as a function of time and space;

- Drought in [hours] as a function of space (immediately follows from *R = 0* over longer durations of time).

7.3 Spatial scale of analysis

The spatial scale of analysis depends on the autocorrelation function $\rho_{(x,x+\tau)}(\tau)$ of the process of interest. Commonly the autocorrelation is written as:

$$\rho_{x,x+\tau}(\tau) = \mathrm{e}^{-\frac{\pi}{4}\cdot\left(\frac{\tau}{D}\right)^2} \quad (25)$$

in which:

$$D = \int_0^{\infty} \rho_{x,x+\tau}(\tau)\cdot \mathrm{d}\,\tau \quad (26)$$

Values for D, which is known as the spatial scale or fluctuation scale, are very much case dependent. Some typical values for *D* are:

- 100 km for water levels along the coastline;

- 5 to 10 km for shower gusts;

-20 to 50 km for wave heights;

- 1 km for crest heights of embankments.

7.4 Methodology

Currently two main approaches can be distinguished in defining the flood:

The first one is generated by the drainage area, with certain conditions of runoff, in a previously defined storm. It is the approach used in the development of the method of the Probable Maximum Flood (PMF), commonly used in the United States. The PMF is defined as the estimate of the volume that can be expected with the most severe combination of conditions that are "reasonably possible" in a region and usually leads to conservative results.

The second approach uses a certain probability of a certain flood not being overcome or, using the usual terminology, a period of return in years. This method addresses the problem in terms of probability. The probability (*P*) that a certain flow is to be exceeded over *N* years, being F the probability that the flow is not surpassed in a year, is:

$$P = 1 - F^N \quad (27)$$

or expressed on the basis of the period of return *T*:

$$P = 1 - \left(1 - 1/T\right)^N \quad (28)$$

This allows the calculation for a certain period of return (*T*) and a service life of the infrastructure (*N*).

There are three basic types of methods used at present for the estimation of probabilities:

- Empirical. Based on empirical formulas that relate the maximum flow rate exclusively with the area of the basin, so frequently carry out an excessive simplification of the phenomenon of the flood. However, their employment in the region where it was obtained usually gives acceptable results.
- Statistical. Based on the treatment of existing local and regional data, properly using the historical references in the case they are available. These methods obtain an estimation of the law of frequency of maximum flow and sometimes of flood volumes. They require the existence of peak flow data being then subject to the availability of this type of information. The frequent absence of peak flow data is the main difficulty in the application of the method, so frequently these are estimated from daily average flow, which introduces important uncertainties in the baseline data.
- Hydrometeorological. Simulate the rainfall-runoff process, usually using deterministic models of varying complexity. The data required are fundamentally rainfall data and therefore leverage the advantage of the existing higher density and length of the pluviometric network with respect to the gauging series.

The use of one or another method is conditioned by both, the very definition of the design flood and the availability of data.

The adoption of a design flood based on a particular storm, necessarily requires modelling of the rain-runoff process and therefore it should be dealt with the **hydrometeorological methods**.

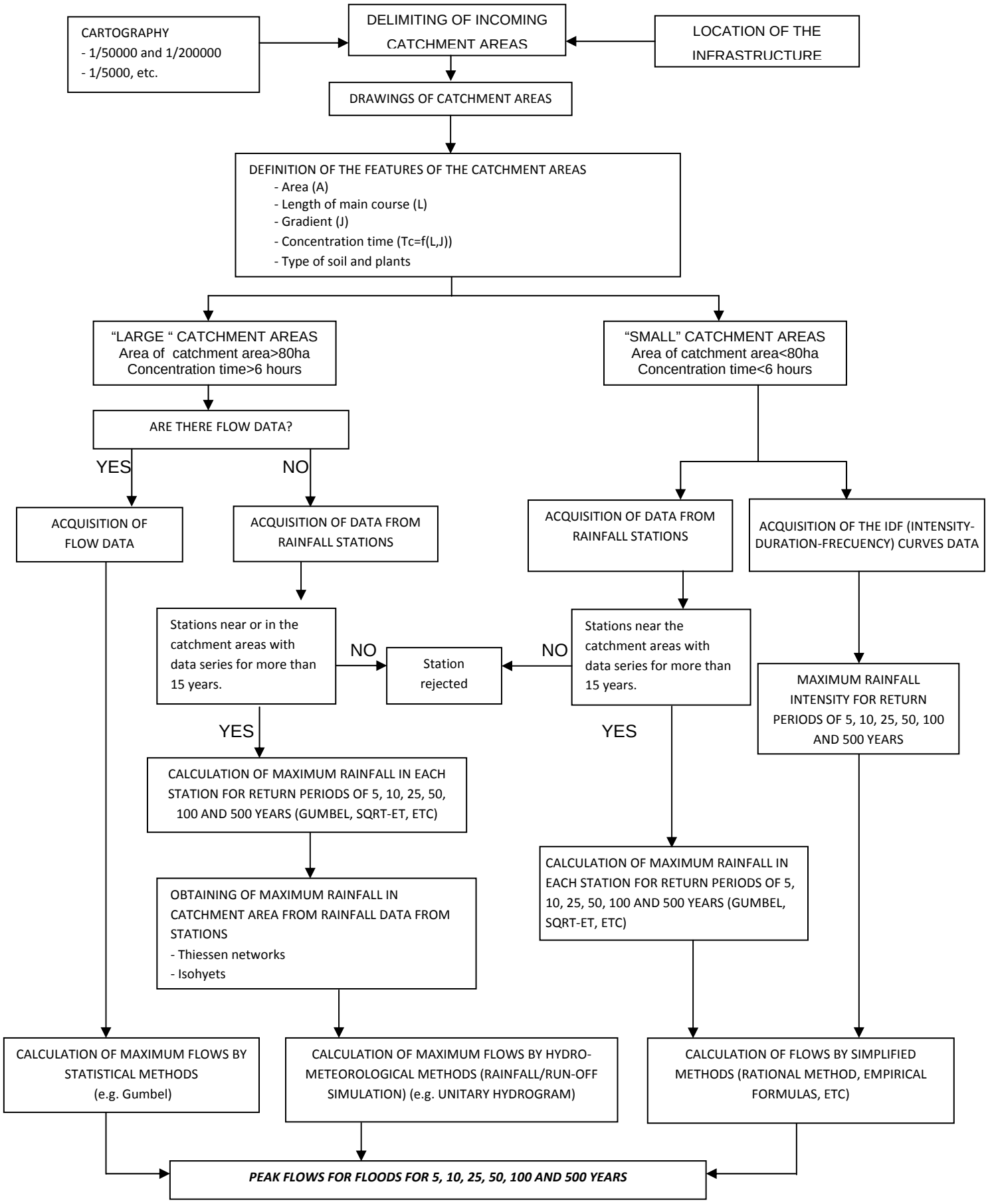

Figure 27: Contents of a hydrological study of natural catchment areas

7.4.1 Rainfall

For the determination of rainfall in the study area, there are several sources of data, all of which are official, provided by the Central Administration or by local agencies. All sources of information are usually studied and the more conservative value for each return period is finally adopted. It can be done in two ways:

- Rainfall stations data collection. Rainfall stations should have to cover generously the entire surface of the basin and should have series of data for more than fifteen years. The quality of statistical adjustments of precipitation from the rainfall stations selected must be analysed, in light of its graphical representation. For this, the method of maxima adjustment is used, applying a distribution function. The most widely used distribution function is the Gumbel distribution although there is an increasing trend to use the SQRT-Etmax distribution since it is more reliable for high return periods (Zorraquino, 2004). Such fitting of distributions has to be done for each rainfall station in the given area. In order to obtain the calculation of rainfall for the catchment areas under consideration, once the maximum daily rainfall has been obtained for each station, the Thiessen networks method or the Isohyets method (this is usually used for large catchment areas and with a sufficient number of rainfall stations) is applied. An arithmetic average or a weighted average must never be used for the areas of each catchment area. Once the maximum daily rainfall is fixed for the return period, a calculation is applied in order to get the maximum rainfall intensity.
- Map of maximum daily rainfall. Maximum daily rainfall for the different return periods can be obtained from the map of maximum daily rains usually published in each country (e.g. in Spain is the "Mapa de Máximas Lluvias Diarias en la España Peninsular", Dirección General de Carreteras, 1999).

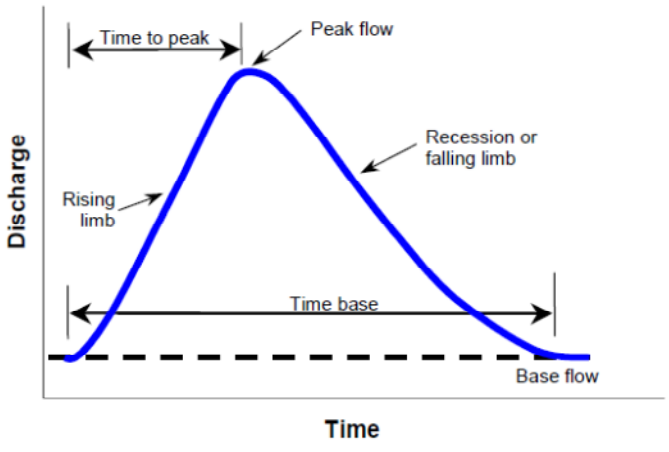

Figure 28: Elements of a flood hydrograph

7.4.2 Flow Calculation

Hydro-meteorological methods, as outlined above, use hydrological models to simulate the process of rain runoff. These models are broadly categorized as either peak-flow or continuous-flow models. Continuous flow models estimate the variation of runoff over time. Peak flow models estimate only

peak runoff values. Greater simplicity in the formulation and the flexibility to address hourly or even smaller time scales, makes most common the use of the second type of models.

While several methods exist, the rational method is by far the most common method for estimating peak runoff.

Greater simplicity in the formulation and the flexibility to address hourly or even smaller time scales, makes most common the use of the second type of models.

Rational Method

This method uses an empirical linear equation to compute the peak runoff rate from a selected period of uniform rainfall intensity:

$$Q = C \cdot i \cdot A \quad (29)$$

where: *A* is the area that drains to the design point of interest (the drainage area) in [ha], *C* is the runoff coefficient for that drainage area (dimensionless), *i* is the design rainfall intensity in [mm/h], *Q* is the peak storm water runoff rate from the drainage area in [m^3/s].

With the rational method, peak flow is obtained at a particular control point in the catchment area. To obtain the flow of calculation in small catchment areas (time of concentration less than 6 hours), the method of common application is the rational method whose formulation is expressed below (the divider is introduced by the change of units as expressed below).

$$Q = \frac{C \cdot i \cdot A}{3.6} \quad (30)$$

Q [m^3/s]: Peak flow

A [km^2]: Catchment area

i [mm/h]: Maximum rainfall intensity in the duration time *Tc*

C: Run off coefficient of the drainage area

In Spain, this method has been enhanced by Témez (1991) and Ferrer (1993), introducing some correction factors and it is now applied in most infrastructure projects. This method has been enhanced and used in this way in other European countries such as Greece. The formulation of this modified rational method is as follows:

$$Q = \frac{C \cdot i \cdot A}{3.6} \cdot K_u \quad (31)$$

where K_u is the uniformity coefficient.

This method is applicable to all countries but the method of calculation of the specific variables (*C*, *i*) depend on each country (provided the data for the calculation is available).

The method should be limited to drainage areas less than 80 ha with generally uniform surface cover and topography and time of concentration of less than 6 hours. Only the peak runoff rates can be

computed using this method. Since it is not based on a total storm duration, but a period of rain that produces the peak runoff rate, the method cannot compute runoff volumes unless a total storm duration is assumed.

Runoff coefficient

Runoff coefficient of drainage area (*C*) represents the part of the rainfall which becomes a runoff and depends on land use, soil, type and slope. A table with such coefficients according to Knox County Tennessee, Stormwater Management Manual, section on the Rational Method (Knox County, 2014), is presented below:

Table 11: Runoff coefficient for storms of 5 to 10-year frequencies

Land Use	Runoff Coefficient (C) by Hydrologic Soil Group and Ground Slope											
	A			B			C			D		
	<2%	2 - 6%	>6%	<2%	2 - 6%	>6%	<2%	2 - 6%	>6%	<2%	2 - 6%	>6%
Forest	0.08	0.11	0.14	0.10	0.14	0.18	0.12	0.16	0.20	0.15	0.20	0.25
Meadow	0.14	0.22	0.30	0.20	0.28	0.37	0.26	0.35	0.44	0.30	0.40	0.50
Pasture	0.15	0.25	0.37	0.23	0.34	0.45	0.30	0.42	0.52	0.37	0.50	0.62
Farmland	0.14	0.18	0.22	0.16	0.21	0.28	0.20	0.25	0.34	0.24	0.29	0.41
Res. 1 acre	0.22	0.26	0.29	0.24	0.28	0.34	0.28	0.32	0.40	0.31	0.35	0.46
Res. 1/2 acre	0.25	0.29	0.32	0.28	0.32	0.36	0.31	0.35	0.42	0.34	0.38	0.46
Res. 1/3 acre	0.28	0.32	0.35	0.30	0.35	0.39	0.33	0.38	0.45	0.36	0.40	0.50
Res. 1/4 acre	0.30	0.34	0.37	0.33	0.37	0.42	0.36	0.40	0.47	0.38	0.42	0.52
Res. 1/8 acre	0.33	0.37	0.40	0.35	0.39	0.44	0.38	0.42	0.49	0.41	0.45	0.54
Industrial	0.85	0.85	0.86	0.85	0.86	0.86	0.86	0.86	0.87	0.86	0.86	0.88
Commercial	0.88	0.88	0.89	0.89	0.89	0.89	0.89	0.89	0.90	0.89	0.89	0.90
Streets: ROW	0.76	0.77	0.79	0.80	0.82	0.84	0.84	0.85	0.89	0.89	0.91	**0.95**
Parking	0.95	0.96	0.97	0.95	0.96	0.97	0.95	0.96	0.97	0.95	0.96	**0.97**
Disturbed Area	0.65	0.67	0.69	0.66	0.68	0.70	0.68	0.70	0.72	0.69	0.72	0.75

where:
- Group A: Deep sand; deep loess; aggregated soils;
- Group B: Shallow loess; sandy loam;
- Group C: Clay loams; shallow sandy loam; soils low in organic content; soils usually high in clay;
- Group D: Soils that swell significantly when wet; heavy plastic clays; certain saline soils.

For 25-year frequency, the runoff coefficient should be multiplied by 1.1, 50-year by 1.2, 100-year by 1.25.

Intensity calculation

Intensity is defined as ratio of rainfall depth with time and is commonly given in the units of millimeters per hour (inches per hour). All precipitation is measured as the vertical depth of water (or water equivalent in the case of snow) that would accumulate on a flat level surface if all the precipitation remained where it fell. A variety of rain gauges have been devised to measure precipitation. All first-order weather stations use gauges that provide nearly continuous records of

accumulated rainfall with time. These data are typically reported in either tabular form or as cumulative mass rainfall curves.

- Intensity is the most important of the rainfall characteristics. All other factors being equal, the more intense the rainfall, the larger will be the discharge rate from a given watershed.
- Duration is the time from the beginning of rainfall to the point where the mass curve becomes horizontal, indicating no further accumulation of precipitation.
- Frequency is also an important characteristic because it establishes the frame of reference for how often precipitation with given characteristics is likely to occur. From the standpoint of highway design, a primary concern is the frequency of occurrence of the resulting surface runoff, and in particular, the frequency of the peak discharge.

For use in design, the three characteristics are combined, usually graphically into the intensity-duration-frequency (IDF) curve. Rainfall intensity is graphed along the ordinate and duration along the abscissa. One curve of intensity versus duration is given for each exceedance frequency.

To determine the calculation of storm intensity, generally each country has defined IDF curves that relate the intensity with the duration and frequency of the storm.

If it is possible to get an IDF curve taken from different studies next to the study area, it is simple to get the maximum rainfall intensity only by introducing the duration time and the return period. The only problem is to get a suitable IDF curve. Figure 29 presents an example of an IDF curve in Greece, with the following equation:

$$i = 30.87 \cdot \frac{T^{0.15} - 0.517}{t_s^{0.58}} \quad (32)$$

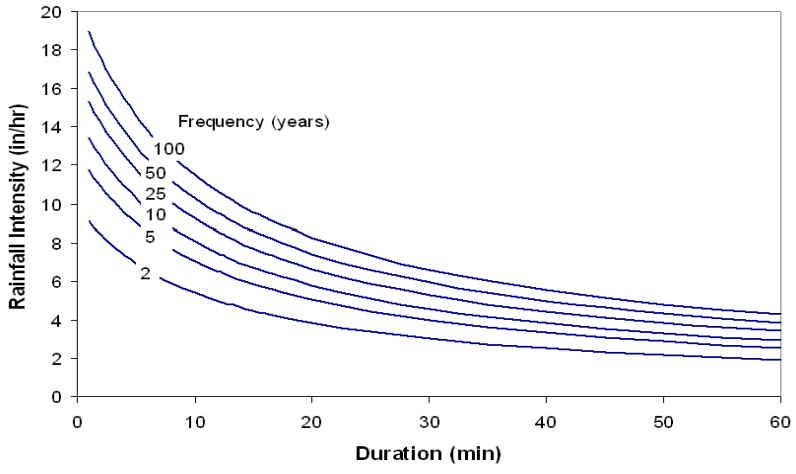

Figure 29: Intensity-duration-frequency (IDF) curve

If IDF curves are not available, the intensity can be calculated using the time of concentration and rainfall associated with the period of return, according to the standards of each country.

Time of concentration Tc

The calculation of rainfall intensity (*i*) is based on the duration of time of concentration (*Tc*). It is the time that the rainfall takes to reach the outlet gauge from the most remote point of the catchment. There are many different empirical equations suggested in a literature for the calculation of *Tc* such as the Manning equation, the National Resources Conservation Service (NRCS) method, etc. (Knox County Stormwater Management Manual, 2008). No overall preferred method is proposed.

There are several formulations that usually link slope and length of the watershed:

- The formula for the concentration time recommended by the Spanish road instruction 5-2IC is a modification of the formula of the US Army Corps of Engineers:

$$T_C = 0.3 \cdot \left(\frac{L}{J^{1/4}} \right)^{0.76} \quad (33)$$

T_C = concentration time [hours]

L = length [km]

J = slope of the main water course [m/m]

- Kirpich formula. Recommended for areas outside city master plans:

$$T_C = 3.97 \cdot \left(\frac{L^3}{H} \right)^{3.385} \quad (34)$$

T_C = concentration time [minutes]

L = length of the natural stream bed [km])

H = maximum altitude difference [km]

- Giandotti formula. Recommended for external catchment area without formed stream:

$$T_C = \frac{4 \cdot F^{1/2} + 1.5 \cdot L}{0.8 \cdot z^{1/2}} \quad (35)$$

T_C = concentration time [hours]

F = surface of catchment area [km^2]

L = length of the line of the natural run-off [km]

z = leveling difference of average leveling of catchment area and the control point [m]

It should be noted that a slight variation of this value represents a big change in the average rainfall intensity.

After that the rainfall intensity could be determined from the intensity-duration-frequency graph or equation for the drainage area location.

Peak Discharge flow

Once all parameters of the equation are known the Peak Discharge can be calculated. An example of calculation is presented in Figure 30 (taken from Bengtson, 2010).

Calculation of Design Rainfall Intensity								
and Peak Storm Water Runoff Rate - S.I. units								
(for specified return period and storm duration)								
Inputs								
Drainage Area, **A** =		25	ha		Runoff Coefficient, **C** =	0,35		
Design Return Period =		15	years		Design Storm Duration, **d** =	22	min	
					(= time of concentration)			
Data from IDF (intensity-duration-frequency) graph or table for the design location:					**Calculation of equation constants (a & b) using linear regression:**			
Input i, mm/hr	**Input** d, min	**Calculated** 1/i, hr/mm			slope =	0,000207	= 1/a	
187	10	0,01			**a** = 1/slope =			**4840**
153	15	0,01						
105	30	0,01			intercept =	0,0033	= b/a	
					b = a*intercept =			**16,2**
Calculation of Design Rainfall Intensity, i, using the equation: i = a/(d + b):								
(using the value for storm duratin, **d**, specified above)								
Design Rainfall Intensity, **i** =						**126,7**	mm/hr	
Calculation of Design Peak Storm Water Runoff Rate, Q, using the equation: Q = CiA								
Design Peak Storm Water Runoff Rate, **Q** =						**3,10**	m^3/s	

Figure 30: Calculation of rainfall intensity and peak runoff

Reservoir models

Other well-known methodologies for flood calculations are based on the linear reservoir methodology for flooding, based on De Zeeuw (1973). The discharge (*Q*) is assumed to have a linear relationship with the water volume stored (*S*):

$$Q(t) = \frac{1}{k} \cdot S(t) \tag{36}$$

where *k* is a constant.

A more detailed description of a single reservoir model can be found in the technical report by the US Army Corps of Engineers (USACE, 1980). The arrangement of the storage elements in series or parallel gives a more flexible structure of model (Koren, 1991).

One step more complicated becomes the non-linear reservoir or the non-linear reservoir with pre-reservoir for recharge (as described in ILRI, 1995). Contrary to the linear reservoir, the non-linear reservoir has a reaction factor that is not a constant, but is a function of storage or discharge. The recharge, also called effective rainfall or rainfall excess, can be modeled by a pre-reservoir giving the recharge as overflow. The pre-reservoir knows the following elements, a maximum storage, an actual storage, a relative storage, a maximum escape rate (i.e. the maximum rate of evaporation plus percolation and groundwater recharge, which will not take part in the runoff process), an actual escape rate, and a storage deficiency.

***Q-h* Relationships**

Water level - discharge relations are commonly developed for gauges by measuring the water discharges at a wide range of water levels (especially for extremely high and low water levels). The water level-discharge relation depends on the shape, size, slope, and roughness of the channel.

For the usual hydraulic structures as weir of flumes this relation can be determined by the following general equation (Jerome Le Coz, 2012):

$$Q = \alpha \cdot (h - h_0)^n \tag{37}$$

where α is a coefficient (depending on the discharge coefficient and length of weir), h_0 is a reference level, and n is an exponent which varies with the type of a structure. For example, for triangular weirs the following formulas are recommended in Table 12: ***Q-h* relationships (by Civil Engineering Portal, 2014)**.

Table 12: *Q-h* relationships (by Civil Engineering Portal, 2014)

Notch (vertex) angle	Discharge formula
90°	$Q = 0.685h^{2.45}$
60°	$Q = 1.45h^{2.47}$
30°	$Q = 2.49h^{2.48}$

From the first formula the water level can be estimated as:

$$h = \sqrt[2.45]{Q / 0.685} \tag{38}$$

For a rectangular weir the coefficient n is n = 2/3. Other formulas for different types of weirs are presented in the Codecogs (2014) library.

Hydrodynamic modelling tools

There are a number of advanced rainfall runoff models which allows to simulate the discharges of a given drainage basin, in literature (Beven, 2012). A selection of hydrodynamic models is given by:

- SOBEK, http://www.deltaressystems.com/hydro/product/108282/sobek-suite

SOBEK can be used for 1D/2D flood simulation of river systems, polder areas, dikes/levees/dam breaches, etc. It is based on the complete De Saint Venant Equations. Nearly any type of hydraulic structure (pumps, weirs, gates, culverts, sluices and bridges) can be specified. The scale of modelling can be from 10 to 100 km^2. The outputs of the model are water depths and depth-averaged velocities, outflow hydrograph downstream. This model allows to simulate accurately transcritical flows, dam break and fast transient flows. Examples of high accuracy calculations by Sobek in dam break simulation can be found in Liang et al. (2004). Sobek also allows to model the breach growth, heavy rain and evaporation, and effect of strong winds.

- DELFT-3D, http://www.deltaressystems.com/hydro/product/621497/delft3d-suite

Delft3D simulates two-dimensional (in either the horizontal or a vertical plane) and three-dimensional flow, sediment transport and morphology, waves, water quality and ecology and handles the interactions between these processes. The D-Flow module includes 3D flow and turbulence modelling, spherical grids, domain decomposition (connect multiple grids; refinement in both horizontal and vertical direction allowed), structures (weirs, gates, floating structures, semi-transparent structures) and horizontal large eddy simulations (sub-grid turbulence in horizontal). It is based on the Navier Stokes equations for an incompressible fluid, under the shallow water and the Boussinesq assumptions. The outputs of the model (flood modelling) are water level, U and V-velocities (horizontal), magnitude and direction, ω-velocities relative to σ-plane (not strictly horizontal but following the bottom topography and the free surface) and w-velocities (velocity in z-direction, Cartesian system).

- HEC-RAS (Hydrologic Engineering Centers River Analysis System) http://www.hec.usace.army.mil/software/hec-ras/features.aspx#Steady

HEC-RAS models 1D steady flow, unsteady flow, sediment transport/mobile bed computations, and water temperature. HEC-RAS for steady flow is based on the solution of the one-dimensional energy equation, for unsteady flow is based on 1-D Saint Venant equation. The different types of hydraulic structures can be specified (bridges, culverts, etc.). The unsteady flow modelling component allows also the simulation of a dam break. Design scale modelling can be from 10 to 100 km^2. The outputs of the model for flood modelling are water depth and average velocity, inundation extent by predicted water depths, and downstream out-flow hydrograph.

Damage curves for fluvial flooding

Flooding may lead to economic damage (direct and indirect), as shown in Figure 31, or to loss of human life, as shown in Figure 32. At an inundation depth of 4 meters, the economic loss has reached 100% of the total economic value of the flooded area. The mortality rate is about 1% of the exposed population, unless the flood goes with a very strong vertical rise. In that case the rate can go up to 50% of the exposed population.

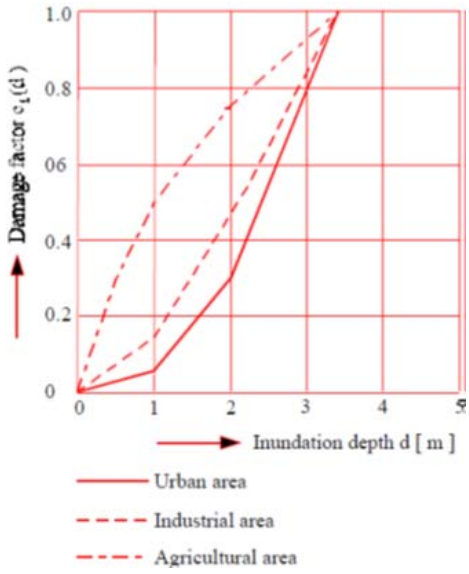

Figure 31: Damage curves for flooding (from Vrijling, 2000)

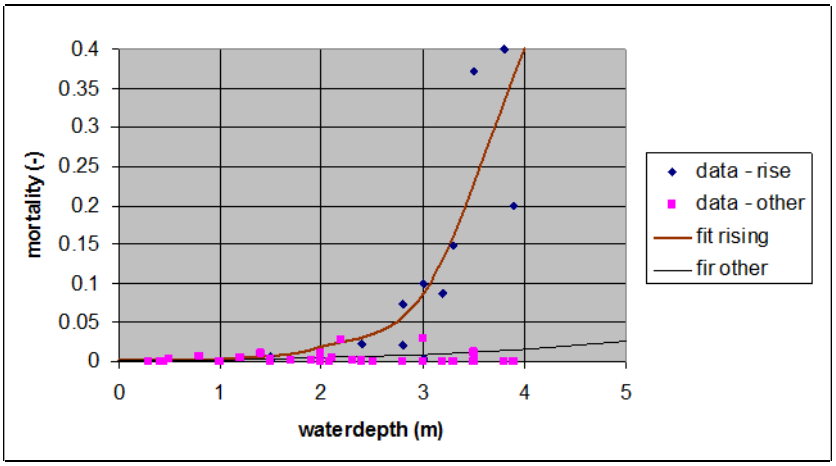

Figure 32: Loss of life caused by flooding (from Vrijling, 2000)

7.5 Conclusions

The rate of runoff resulting from any constant rainfall intensity is maximum when the duration of rainfall equals the time of concentration. That is, if the rainfall intensity is constant, the entire drainage area contributes to the peak discharge when the time of concentration has elapsed. This assumption becomes less valid as the drainage area increases. For large drainage areas, the time of concentration can be so large that the assumption of constant rainfall intensities for such long periods is not valid, and shorter more intense rainfalls can produce larger peak flows. Additionally, rainfall intensities usually vary during a storm. In semi-arid and arid regions, storm cells are relatively small with extreme intensity variations.

The frequency of peak discharge is the same as the frequency of the rainfall intensity for the given time of concentration. Frequencies of peak discharges depend on the following:

1. rainfall frequencies;

2. antecedent moisture conditions in the watershed;

3. the response characteristics of the drainage system.

For small, mostly impervious areas, rainfall frequency is the dominant factor. For larger drainage basins, the response characteristics are the primary influence on frequency. For drainage areas with few impervious surfaces (less urban development), antecedent moisture conditions usually govern, especially for rainfall events with a return period of 10 years or less.

The rainfall intensity is uniformly distributed over the entire drainage area. In reality, rainfall intensity varies spatially and temporally during a storm. For small areas, the assumption of uniform distribution is reasonable. However, as the drainage area increases, it becomes more likely that the rainfall intensity will vary significantly both in space and time.

The fraction (C) of rainfall that becomes runoff is independent of rainfall intensity or volume. The assumption is reasonable for impervious areas, such as streets, rooftops, and parking lots.

For pervious areas, the fraction of runoff varies with rainfall intensity, accumulated volume of rainfall, and antecedent moisture conditions. Thus, the art necessary for application of the Rational Method involves the selection of a coefficient that is appropriate for storm, soil, and land use. By limiting the application of the Rational Method to 200 acres (80 hectares), these assumptions are more likely to be reasonable.

8.0 SCOUR

8.1 General description

River bed consists of cohesive and not cohesive material of different size: sand, gravels, pebbles, etc. In ordinary conditions remains at rest, but during floods, when the flow exceeds the critical beginning of drag, the background particles are transported by waters, and solid flow grows at the same time with the liquid flow.

In a specific section of the river will take place a few inputs and outputs of solid material at the same time, both growing with the liquid flow. The balance (inputs minus outputs) is the determining factor in the evolution of the river bed in that location: if it is positive there will be silting, else, scour will occur, and stability when the balance is zero.

In areas prone to the mismatch, this is accentuated as the flow grows, and with it the scour and silting. If the presence of a bridge, with its piles and abutments, changes the natural flow of the river, in its area a few unique erosions will occur which will be added to the generals of the section where it is located.

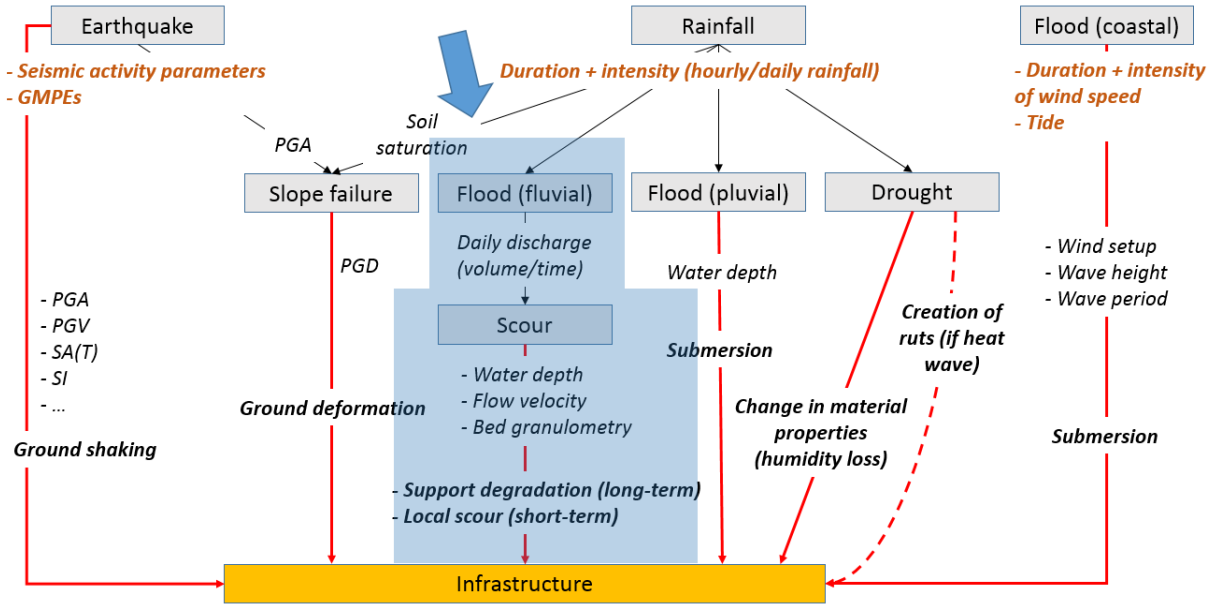

Figure 33: Synthesis of considered hazards and their corresponding IMs. Flood-induced scour hazard corresponds to the branch with grey background, the blue arrow pointing at it.

The most common cause of bridge failures is from floods scouring bed material from around bridge foundations. A U.S. Federal Highway Administration study (Chang, 1973), concludes that from 383 bridges observed failures, 97% were due to hydraulic problems of local erosions: 25% in piers and 72% in abutments. It means that only 3% of registered failures were due to causes unrelated to the hydraulics.

In structures, the scour at the piers and abutments for the reference discharge can endanger its stability as they are not always founded on solid rock. So it is necessary to check if the maximum foreseeable erosion affects the foundation and if so, then project elements for control, mainly rockfill beds.

Every bridge over water, whether existing or under design, should be assessed as to its vulnerability to floods in order to determine the prudent measures to be taken. The added cost of making a bridge less vulnerable to scour is small when compared to the total cost of a failure which can easily be two to ten times the cost of the bridge itself.

To successfully complete the study of scour, river bedstream granulometry and hydraulic data must be known.

8.2 Intensity measures

The following parameters are used to calculate the scour at bridges:

- Water depth [m];
- Flow Velocities [m/s];
- Total flow or discharge [m^3/s];
- Streambed granulometry (bed material gradation);
- Piers: location and shape;
- Abutments: location, shape and length.

Water elevation and flow velocity depend on the daily discharge and the stream geometry. A hydraulic model of the stream and the bridge, made with HEC-RAS or a similar program, is necessary to determine these parameters.

8.3 Spatial scale of analysis

Scour has to be evaluated at the level of the bridge span (i.e. for a few tens to several hundreds of meters). For general and contraction scour, a global depth level can be estimated at the scale of the riverbed cross-section.

Local scour depends on the shape of piles and it should be evaluated at each location, with a distinction between scour at piers or abutments.

8.4 Methodology

The proposed model is an empirical model based on laboratory tests and experience. Many studies had been developed since the 80's. Melville (1997) resumed studies of different investigators through envelope curves that are adjusted to the laboratory data of these authors.

Determining the magnitude of scour is complicated by the cyclic nature of the scour process. Scour can be deepest near the peak of a flood, but hardly visible as floodwaters recede and scour holes refill with sediment. Designers and inspectors need to carefully study site-specific subsurface information in evaluating scour potential at bridges, giving particular attention to foundations on rock. Massive rock formations with few discontinuities are highly resistant to scour during the lifetime of a typical bridge.

All of the equations for estimating contraction and local scour are based on laboratory experiments with limited field verification. However, contraction and local scour depths at piers as deep as computed by these equations have been observed in the field. The equations recommended in this document are considered to be the most applicable for estimating scour depths.

There are different international standards, one of the most used is the publication HEC (Hydraulic Engineering Circular) of the U.S. FHWA (Federal Highway Administration), specifically the HEC-18 circular, "Evaluating scour at bridges" Fourth Edition (2001). It presents the state of knowledge and practice for the design, evaluation and inspection of bridges for scour. It contains revisions obtained from further scour-related developments and the use of the 1995 edition by the highway engineering community.

Total scour at a highway crossing is comprised of three components:

- General Scour : Erosion due to the channel itself, regardless of the existence of the structure;
- Contraction Scour: Erosion due to narrowing generated by the structure;
- Local Scour: Erosion due to turbulence created around piers and abutments.

To calculate general scour, a Spanish publication "Control de la erosión fluvial en puentes" (Bridge's fluvial scour control), MOPU (1988), is followed. To calculate the general erosion, this method is preferred to the HEC one since it needs for the calculation a large number of very detailed data, which could only be obtained in field. For this reason we believe that for INFRARISK it makes no sense to use a methodology that requires so much detail.

8.4.1 General Scour

The general scour is influenced by the flow transportation capability on the river bedstream, regardless of the existence of a structure, therefore depends on the flow velocity and the grain size of the bed material.

The formulation applied to calculate the general erosion, comes from the D_{50} to characterize the bed material, and has the following expression (D_{50} = Median diameter of bed material) based on the Blench methodology:

$$e_{gen} = K \cdot y_r - y_0 \quad (39)$$

where:

- e_{gen} = General scour. Minimum value: $y_0/4$;
- K = Average depth correction factor;
- $y_r = \alpha \cdot y_c$;
- α = correction factor based on the size of the river bedstream material, from figure 4.9 of the MOPU guide:

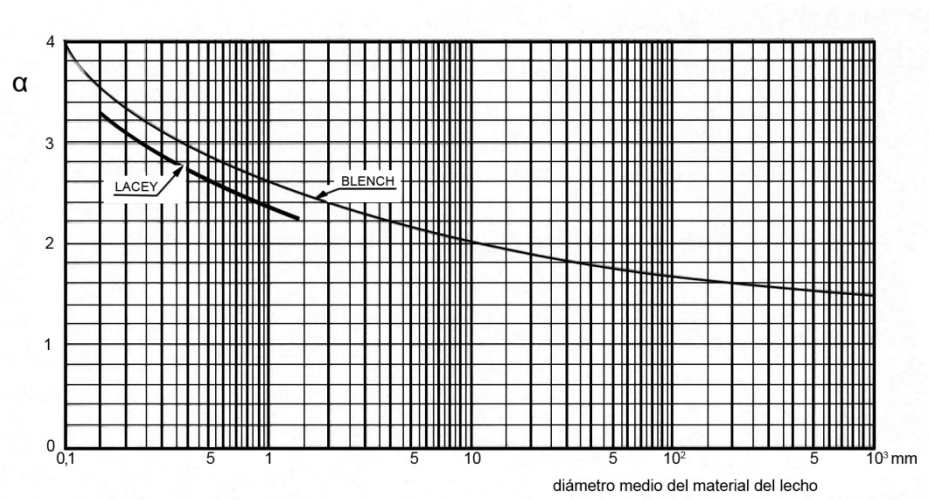

Figure 34: Correction factor α as a function of the size of the riverbed material (MOPU guide, 1988)

- y_c = Critical depth;
- y_o = Normal depth.

This equation can only be used in case of not cohesive material river beds. The greatest depths of scour are usually found on streams having sand or sand-silt beds. The general conclusion is that scour problems are as common on streams having coarse bed material as on streams having fine bed material. However, very deep scour is more probable in fine bed material. In general, sand-bed alluvial streams are less stable than streams with coarse or cohesive bed and bank material.

8.4.2 Contraction Scour

First the scouring condition has to be found, since according to the condition (whether Clear Water or Lived Bed), formulation to be used is different. This condition depends on critical velocity. If the critical velocity of the bed material is larger than the mean velocity ($V_c > V$), then clear-water contraction scour will exist, and if the critical velocity is less than the mean velocity ($V_c < V$), then live-bed contraction scour will exist.

To calculate the critical velocity the equation used is (5.1, HEC-18):

$$V_c = K_u \cdot y^{1/6} \cdot D^{1/3} \; V_c = K_u \cdot y^{1/6} \cdot D^{1/3} \tag{40}$$

where:

- V_c = Critical velocity above which bed material of size D and smaller will be transported, [m/s];
- y = Average depth of flow upstream of the bridge, [m];
- D = Particle size for V_c, [m];
- K_u = 6.19 SI units.

The equation for **Live Bed** contraction scour is (5.2, Hec-18):

$$\frac{y_2}{y_1} = \left(\frac{Q_2}{Q_1}\right)^{6/7} \cdot \left(\frac{W_1}{W_2}\right)^{K_1} \; \frac{y_2}{y_1} = \left(\frac{Q_2}{Q_1}\right)^{6/7} \cdot \left(\frac{W_1}{W_2}\right)^{K_1} \tag{41}$$

$$y_s = y_2 - y_1 \tag{42}$$

where:

- y_S = Scour depth;
- y_1 = Average depth in the upstream main channel, [m];
- y_2 = Average depth in the contracted section, [m];
- Q_1 = Flow in the upstream channel transporting sediment, [m^3/s];
- Q_2 = Flow in the contracted channel, [m^3/s];
- W_1 = Bottom width of the upstream main channel that is transporting bed material, [m];
- W_2 = Bottom width of the main channel in the contracted section less pier width(s), [m];
- K_1 = Exponent determined below, depends on velocity:

Table 13: Estimation of exponent K1 as a function of velocity

V^*/ω	K_1
< 0.50	0.59
0.50 - 2.00	0.64
> 2.00	0.69

  - $V^* = \sqrt{g \cdot y_1 \cdot S_1}$;
  - G = Acceleration of gravity (9.81 m/s^2);
  - S_1 = Slope of energy grade line of main channel, [m/m];
  - ω =based on the river bedstream material D_{50}:

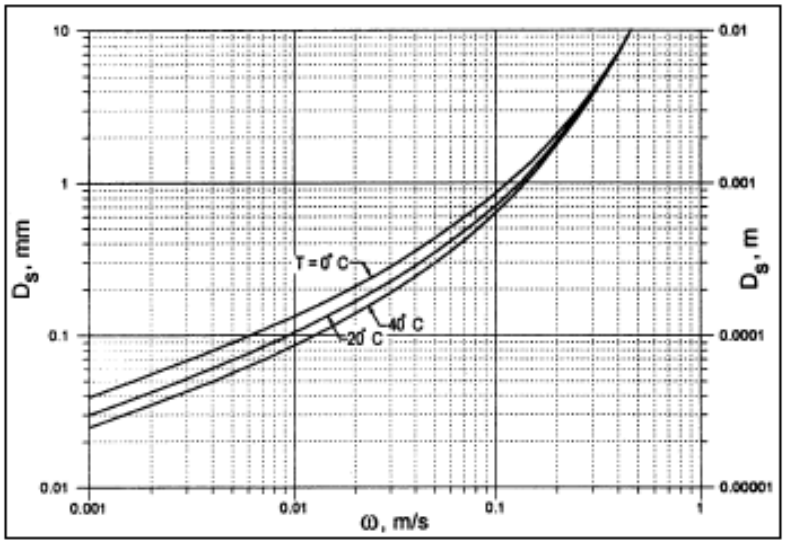

Figure 35: Evolution of ω as a function of bedstrean material and temperature

The equation for **Clear Water** contraction scour is (5.4, Hec-18):

$$y_2 = \left(\frac{K_u \cdot Q^2}{D_m^{2/3} \cdot W^2} \right)^{3/7} \quad (43)$$

$$y_s = y_2 - y_1 \quad (44)$$

where:

- y_s = Scour depth;
- y_1 = Average depth in the upstream main channel, [m];
- y_2 = Average equilibrium depth in the contracted section after contraction scour, [m];
- Q = Discharge through the bridge or on the set-back overbank area at the bridge associated with the width W, [m^3/s];
- W = Bottom width of the contracted section less pier widths, [m];
- D_m = Diameter of the smallest non transportable particle in the bed material (1.25 x D_{50}) in the contracted section, [m];
- K_u = 0.025 [SI units];

8.4.3 Local Scour

The methodology is presented below, being necessary to make a difference between piers and abutments.

Piers:

To determine the maximum pier scour depths, the recommended equation for both live-bed and clear-water pier scour is:

$$\frac{y_s}{a} = 2 \cdot K_1 \cdot K_2 \cdot K_3 \cdot K_4 \cdot \left(\frac{y_1}{a}\right)^{0.35} \cdot Fr_1^{0.43} \quad (45)$$

where:

- y_s = Scour depth;
- y_1 = Flow depth directly upstream of the pier, [m];
- K_1 = Correction factor for pier nose shape from the following figure:

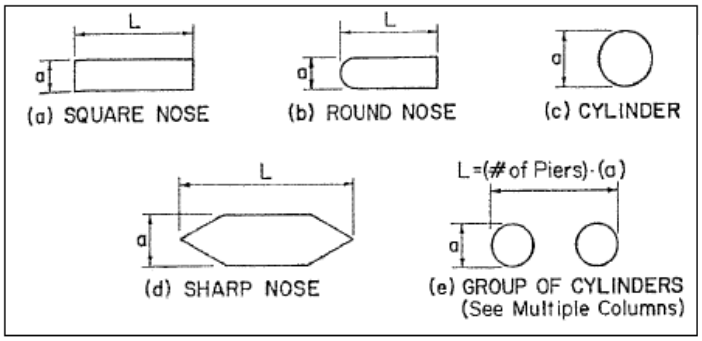

Table 6.1. Correction Factor, K_1, for Pier Nose Shape.	
Shape of Pier Nose	K_1
(a) Square nose	1.1
(b) Round nose	1.0
(c) Circular cylinder	1.0
(d) Group of cylinders	1.0
(e) Sharp nose	0.9

Figure 36: Estimation of the correction factor for nose shape

- K_2 = Correction factor for angle of attack of flow from:

$$K_2 = \left(\cos\theta + \frac{L}{a} \cdot sen\,\theta\right)^{0.65} \quad (46)$$

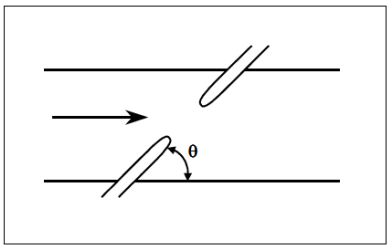

Figure 37: Definition of the angle of attack of flow

- K_3 = Correction factor for the riverbed morphology:

Table 6.3. Increase in Equilibrium Pier Scour Depths, K_3, for Bed Condition.		
Bed Condition	Dune Height m	K_3
Clear-Water Scour	N/A	1.1
Plane bed and Antidune flow	N/A	1.1
Small Dunes	3> H ≥ 0.6	1.1
Medium Dunes	9> H ≥ 3	1.2 to 1.1
Large Dunes	H ≥ 9	1.3

Figure 38: Estimation of the correction factor for bed condition

- K_4 = Correction factor for armoring by bed material size:
  - If $D_{50} < 2$ mm or $D_{95} < 20$ mm, $K_4 = 1$;
  - Otherwise:

$$K_4 = 0.40 \cdot \left(\frac{v_1 - v_{icD_{50}}}{v_{cD_{50}} - v_{icD_{95}}} \right)^{0.15} > 0 \quad (47)$$

$$v_{icD_x} = 0.645 \cdot \left(\frac{D_x}{a} \right)^{0.053} \cdot v_{cD_x} \quad (48)$$

$$v_{cD_x} = K_u \cdot y_1^{1/6} \cdot D_x^{1/3} \; v_{cD_x} = K_u \cdot y_1^{1/6} \cdot D_x^{1/3} \quad (49)$$

where:

- y_1 = Depth of flow just upstream of the pier, excluding local scour, [m];
- v_1 = Velocity of the approach flow just upstream of the pier, [m/s];
- D_x = Grain size for which x percent of the bed material is finer, [m];
- K_u = 6.19 [SI units];

Abutments:

For abutments the equation used depends only on the ratio length of the embankment affected by water depth / water depth:

- $L/y_s \leq 25$ → Froelich's equation;
- $L/y_s > 25$ → Hire equation.

Froelich's equation is:

$$\frac{y_s}{y_a} = 2.27 \cdot K_1 \cdot K_2 \cdot \left(\frac{L'}{y_a}\right)^{0.43} \cdot Fr^{0.61} + 1 \quad \frac{y_s}{y_a} = 2.27 \cdot K_1 \cdot K_2 \cdot \left(\frac{L'}{y_a}\right)^{0.43} \cdot Fr^{0.61} + 1 \tag{50}$$

where:

- y_s = Scour depth, [m];
- K_1 = Coefficient for abutment shape:

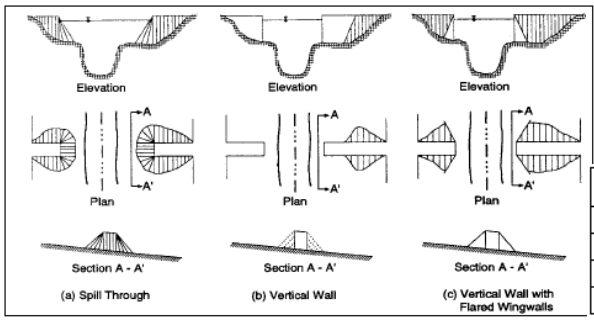

Table 7.1. Abutment Shape Coefficients.

Description	K_1
Vertical-wall abutment	1.00
Vertical-wall abutment with wing walls	0.82
Spill-through abutment	0.55

Figure 39: Estimation of the correction factor for abutment shape

- K_2 = Coefficient for angle of embankment to flow:

$$K_2 = \left(\frac{\theta}{90}\right)^{0.13} \tag{51}$$

- L' = Length of active flow obstructed by the embankment, [m];
- y_a = Average depth of flow on the floodplain (A_e/L), [m];
- Fr = Froude Number of approach flow upstream of the abutment:

$$Fr = \frac{v_e}{\sqrt{g \cdot y_a}} \tag{52}$$

where:

- v_e = Q_e/A_e, [m/s];
- Q_e = Flow obstructed by the abutment and approach embankment, [m3/s];
- A_e = Flow area of the approach cross section obstructed by the embankment, [m^2];
- L = Length of embankment projected normal to the flow, [m].

Hire equation is:

$$\frac{y_s}{y_1} = 4 \cdot Fr^{0.33} \cdot \frac{K_1}{0.55} \cdot K_2 \quad \frac{y_s}{y_1} = 4 \cdot Fr^{0.33} \cdot \frac{K_1}{0.55} \cdot K_2 \tag{53}$$

where:

- y_s = Scour depth, [m];
- y_1 = Depth of flow at the abutment on the overbank or in the main channel;
- Fr = Froude Number of approach flow upstream of the abutment;
- K_1 = Coefficient for abutment shape (calculated as for Froelich's);
- K_2 = Coefficient for angle of embankment to flow (calculated as for Froelich's).

8.5 Conclusions

The proposed calculation model of local and contraction scour is valid for all kind of rivers, although the proposed methodology for calculating general scour is not applicable to beds of cohesive material. However, in this type of river beds, the general scour is not too large compared to the local and contraction scour, which in this case can be ignored.

A formula with general validity that defines this type of erosion is unviable, since it is very sensitive to countless local morphological factors affecting hydraulic circulation and sediment through the main and the flood channel. The more extensive is the area of influence, the minor is the accuracy obtained, as scour processes are subject to changes in the rates of transport and silting of solid particles.

The more realistic is the model, the more accurate will be the scour calculation. However, the baseline data include those relating to hydraulic flow (discharge, water velocity and depth) that will be obtained from a study of rainfall and flood. On the other hand, granulometric data will be approximated, obtained from geological maps or projects, not taking samples on site and the corresponding tests, which will give greater uncertainty to the method.

9.0 COASTAL FLOODING

9.1 General description

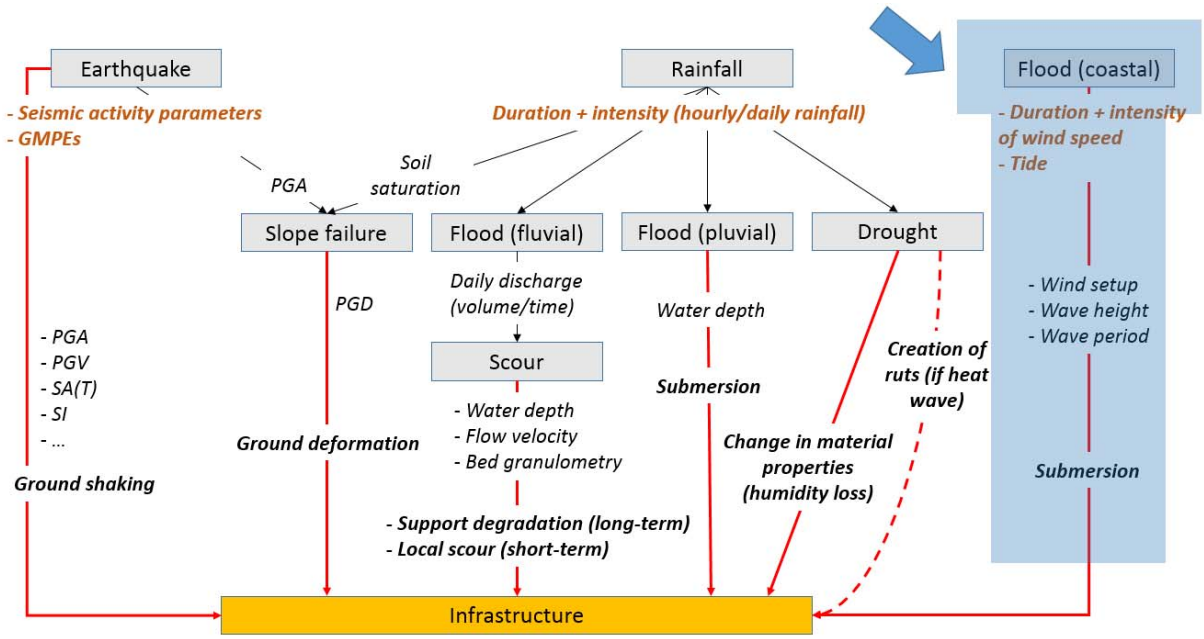

Figure 40: Synthesis of considered hazards and their corresponding IMs. Coastal Flooding

Coastal flood processes (Figure 41) are complex phenomena which require a technical approach and experience in the analysis application; it is not a prescriptive technique that can be applied uniformly in all study areas.

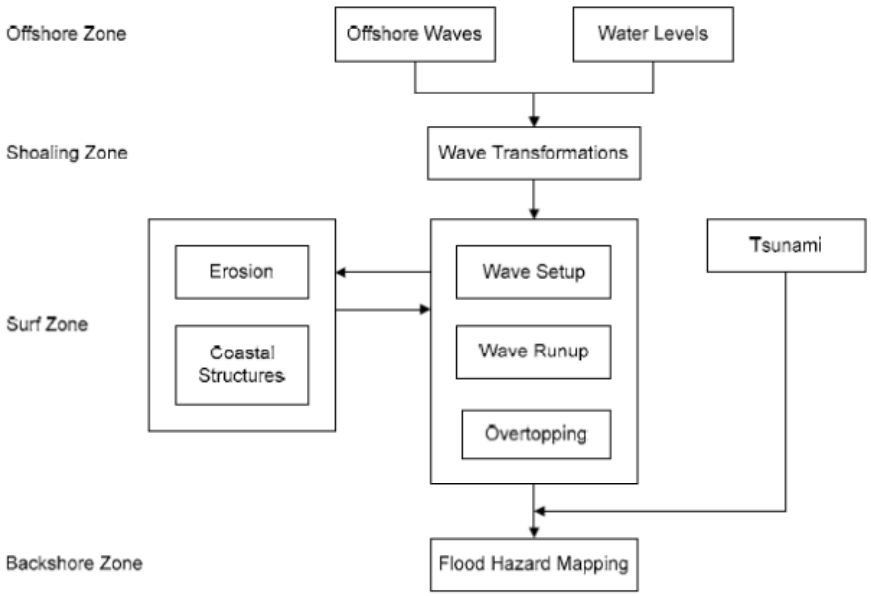

Figure 41: Types of coastal zones and corresponding physical processes

This section establishes the main guidelines applied to a range of settings, but explicit warning is made that all settings and conditions cannot be addressed in general terms due to the broad variability of the problem.

9.2 Intensity measures

The main intensity measures to represent the damaging effects of coastal floods are the following:

- Wind setup, in [m];
- Wave height, in [m];
- Wave period, in [s].

9.3 Spatial scale of analysis

The spatial scale of analysis depends on the autocorrelation function $\rho(x,x+\tau)(\tau)$ of the process of interest, as shown in Equations 25 and 26. Some typical values for the spatial scale D are 100 km for water levels along the coastline and 20 to 50 km for wave heights.

9.4 Methodology

In order to achieve Flood Hazard mapping and Coastal Flood Hazard analyses a first assessment is made to obtain information of the main agents and parameters involved in the phenomenon.

- **Topography/Bathymetry**: shall obtain backshore topography to define hazard zones, obtain near shore bathymetry to define beach profiles, and define the geometry to evaluate hydrodynamic conditions.
- **Wind**: The climate is dependent on localized wind conditions, and sometimes wave data are unavailable at the suitable resolution. In those cases identification must be done of appropriate wind data sources.
- **Tide and Currents**: It is needed to define fundamental tide characteristics, such as astronomical tide, storm surge, tidal amplification, wind setup, and tidal and fluvial currents.
- **Waves**: Occasionally it's possible to obtain available data on the observed wave height, wave length, and wave period, but water physical processes can be complex and may require detailed numerical modeling to define adequately the extreme waves.

Coastal analyses involving hydrodynamic modeling for development of water levels and wave processes (transformation, refraction, and diffraction) are highly specialized and complex.

The response approach will be known through measured or predicted wave conditions along with simultaneously measured or predicted water-levels to determine site specific storm response parameters. Then some estimations must be done such as run-up and maximum water levels at the points of interest.

The extent and complexity of water coastal flood analyses can be summarized in some basic steps considering the following studies as the main lines for analysis methods.

9.4.1 Waves

According to coastal setting and availability of data it will be possible sometimes to have long-term wave information to develop flood hazard estimates. If these data are not available, wave estimation must be done. There are two general approaches for that: parametrical and numerical.

A parametric model for forecasting wave conditions is also based on wave growth in a uniform wind field in a one-dimensional situation. The earliest versions of this type of models date back to Sverdrup and Munk who developed the approach to enable the allied forces to perform wave forecasts for the Normandy landing in 1944. In the 1950's, Bretschneider further developed the concept, so that the approach is now known as the SMB-method (see CERC, 1973). The model is in a dimensionless form. The following set of dimensionless parameters is defined:

$$\begin{aligned} \tilde{H}_s &= \frac{H_s g}{u^2} \\ \tilde{T} &= \frac{Tg}{u} \\ \tilde{F} &= \frac{Fg}{u^2} \\ \tilde{d} &= \frac{dg}{u^2} \end{aligned} \tag{54}$$

The dimensionless wave height is a function of dimensionless Fetch and dimensionless water depth by:

$$\tilde{H}_s = \tilde{H}_\infty \tanh\left(k_3 \tilde{d}^{m_3}\right) \tanh\left(\frac{k_1 \tilde{F}^{m_1}}{\tanh\left(k_3 \tilde{d}^{m_3}\right)}\right) \tag{55}$$

Where:

$\tilde{H}_\infty$: dimensionless wave height in a wind field of infinite length and infinite water depth;
k_1, k_3, m_1, m_3: empirical coefficients.

The dimensionless wave period is written in a similar form:

$$\tilde{T} = \tilde{T}_\infty \tanh\left(k_4 \tilde{d}^{m_4}\right) \tanh\left(\frac{k_2 \tilde{F}^{m_2}}{\tanh\left(k_4 \tilde{d}^{m_4}\right)}\right) \tag{56}$$

With parameters similar to the wave height model.

The empirical parameters are derived from a very large dataset, containing observations from various locations all over the world. The values are stated in the Shore Protection Manual (CERC, 1973). An overview is given in the following table:

Table 14: Empirical parameters

Parameter	Value
H	0.283
T	7.539
k_1	0.0125
k_2	0.0770
k_3	0.5300

Using the parametric models outlined above, the wind setup and wave conditions can be written as a function of the wind speed, provided a suitable schematisation to a one dimensional situation can be found.

The parametric models (1D) include the most rudimentary physics and the numerical models require a big volume of data and are more computationally demanding.

The primary source of offshore wave information consists of predictions from wave hindcasting models, supported by limited measurements. The hindcast databases have been extended to cover relatively long periods (30 years or more), while measurements are generally available for only a few years and are sparsely spaced. Hindcasts and observations commonly represent conditions at a point offshore, usually in deep water.

This model must include wave generation, dissipation, non-linear interactions and transformations.

- Global Ocean Waves (GOW) and Downscaling Ocean Waves (DOW) are databases provide a reconstruction of various wave parameters for the last decades. GOW covers all the world's oceans and reports on the surf to coastal waters. DOW provides information only on the coast, where the waves are affected by the background bathymetry and local processes.
- WAVEWATCH III (NWWIII) is a third generation model of wave generation where physical processes for wave growing are parametrized including non –linear interactions calculation. This model outputs a statistical wave spectra.
- SWAN – (Delft Hydraulics) public domain code which includes wave generation, dissipation, non-linear interactions and transformations

Because waves in the surf zone are strongly influenced by local bathymetry and shoreline configuration, hindcast or measured wave data must be modified to account for wave transformations between the reference station and the study area.

Then, a wave transformation model including refraction will be used for obtaining spectral wave height and spectral wave period to be used in the run-up and overtopping estimation.

Numerical propagation models can be validated with available buoys and hindcast databases.

- OLUCA (IH Cantabria)- numerical model for wave propagation with parabolic approximation.
- MIKE 21 (DHI) – the NSW module is for near shore spectral wind wave estimation and includes wave generation, dissipation interactions and transformations. Also with a module for wave propagation.

9.4.2 Surge

A statistical method is recommended for determining the still water level for a tidal location subject to flooding.

For studies where long periods (greater than 30 years) of measured or hindcast data are available, the generalized extreme value distribution method is recommended for estimating extreme values, such as 1% annual chance total water level and still water level. For flood studies where long periods of measured or hindcast data are not available then numerical methods are recommended.

- Global Ocean Tide (GOT) is an application that provides the astronomical tide anywhere in the world and Global Ocean Surge (GOS) is a reanalysis database that provides the meteorological tide time scale during the last decades.

Coastal floods are caused by strong winds for sufficient duration of time over a sufficient long fetch length (in combination with weak flood defences). A one-dimensional model for the water level increase due to a uniform wind field can be derived on the basis of the model of Weenink (1958). Consider the infinitesimal water body *dx* in Figure 42.

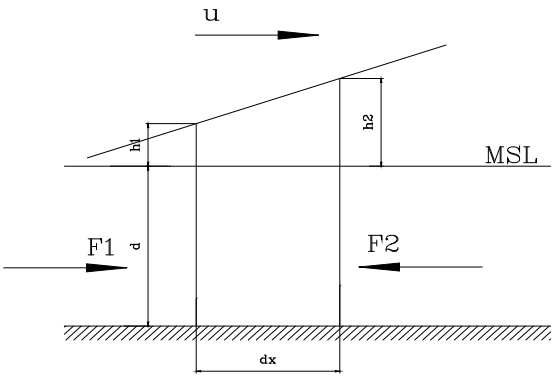

Figure 42: Definition sketch for coastal floods

The basic hypothesis used in describing the joint probability distribution of hydraulic loads is that the wind effects are independent of the astronomical tide. This appears to be a reasonable assumption for deep water conditions.

The force exerted on the water body by the wind field can be written as:

$$F_u = c_l \rho_l u^2 \mathrm{d}x \qquad (57)$$

Where:

- ρ_l = density of air;
- u = wind speed;
- c_l = empirical coefficient;
- dx = infinitesimal water body.

The hydrostatic forces are given by:

$$F_1 = \tfrac{1}{2}\rho_w g\left(d + h_1\right)^2$$
$$F_2 = \tfrac{1}{2}\rho_w g\left(d + h_2\right)^2 \quad (58)$$

Where:

- ρ_w = density of water;
- g = acceleration of gravity.

In equilibrium the hydrostatic forces compensate the force exerted by wind. Rearranging the momentum equation leads to the following differential equation for the wind setup:

$$\frac{\mathrm{d}h}{\mathrm{d}x} = \frac{cu_9^2}{g\left(d(x) + h(x)\right)} \quad (59)$$

Where *c* denotes an empirical coefficient combining the densities of water and air and the empirical coefficient of equation.

Following Weenink, the wind setup is written as a function of the wind speed that is exceeded during nine hours (u_9). If the depth is constant, a parametric model for the wind setup can be derived by integration:

$$h\left(u_9, F, d\right) = -d + \sqrt{d^2 + 2\frac{cu_9^2 F\alpha}{g}} \quad (60)$$

Where:
F: total basin length (fetch); α: factor describing the basin shape.

9.4.3 Run-up

Wave run-up is the uprush of water from wave arrival on a shore barrier intercepting the still water level. The extent of run-up can vary from different storm conditions so that a wide distribution of wave run up elevations provides the description for a specific situation.

This parameter can provide flood hazards above and beyond those from still after inundation and incident wave geometry.

Wave run-up is recommended to be evaluated at the 2% exceedance level. Then coast flood is considered when a part of the section is achieved by 2% of waves for every storm spectrum.

Incident wave run up on natural barriers is expressed originally due to Hunt (1959) in terms of the Iribarren number ξ:

$$\xi = \frac{m}{\sqrt{H/L}} \quad (61)$$

in which *m* is the beach slope or the slope of a barrier such as a breakwater or revetment. *H* and *L* are wave height and length, respectively. The wave characteristics in the Iribarren number can be expressed in terms of breaking or deep water characteristics. For these purposes, two wave characteristics in the Iribarren number are used, including that based on the significant deep water

wave height (H_o) and peak or other wave period (T) of the deep water spectrum, and that based on the significant wave height at the toe of a barrier. The first definition for a sandy beach is as follows:

$$\xi = \frac{m}{\sqrt{H_o / L_o}} \quad (62)$$

where L_o is the deep water wave length:

$$L_o = \frac{g}{2\pi} T^2 \quad (63)$$

and g is the gravitational constant. The beach profile slope is the average slope out to the breaking depth associated with the significant wave height.

The 2-percent incident wave run-up on natural beaches (Rinc) is expressed in terms of the Iribarren number as:

$$R_{inc} = 0.6 \frac{m}{\sqrt{H_o / L_o}} H_o \quad (64)$$

For the case of run-up on a barrier, the Iribarren number is formulated using the significant wave height at the toe of the barrier.

Run-up elevations on breakwaters or revetments depend not only on the height and steepness of the incident wave (and its interaction with the preceding wave), but also on the geometry (and construction) of the structure. Run-up on structures can also be affected by antecedent conditions resulting from the previous waves and structure composition. Because of these complexities, run-up on structures is best calculated using equations developed with tests on similar structures with similar wave characteristics, with coefficients developed from laboratory or field experiments.

The recommended approach to calculating wave run-up on structures is based on the Iribarren number (ξ) and reduction factors developed by Battjes (1974), van der Meer (1988), de Waal and van der Meer (1992), and described in the CEM (USACE, 2003).

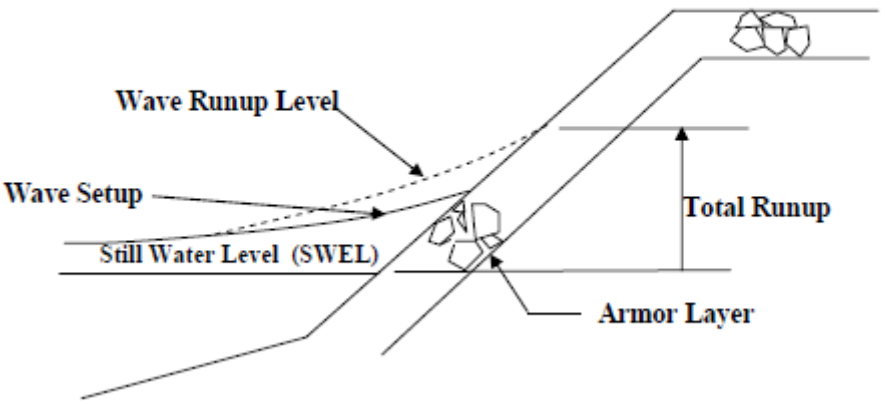

Figure 43: Illustration of run-up on structures

The general form of the wave run-up equation recommended for use (modified from van der Meer, 2002) is:

$$R = H_{mo} \cdot \begin{cases} 1.77 \cdot \gamma_r \cdot \gamma_b \cdot \gamma_\beta \cdot \gamma_P & \text{if } \ 0.5 \le \gamma_b \cdot \xi_{mo} < 1.8 \\ \gamma_r \cdot \gamma_b \cdot \gamma_\beta \cdot \gamma_P \cdot \left(4.3 - \dfrac{1.6}{\sqrt{\xi_{\mathrm{mo}}}} \right) & \text{if } \ \gamma_b \cdot \xi_{mo} \ge 1.8 \end{cases} \quad (65)$$

where:

- R is the 2-percent run-up;
- H_{mo} = spectral significant wave height at the structure toe;
- γ_r = reduction factor for influence of surface roughness;
- γ_b = reduction factor for influence of berm;
- γ_β = reduction factor for influence of angled wave attack;
- γ_P = reduction factor for influence of structure permeability.

Equations for quantifying the γ parameters are presented in the following table. The reference water level at the toe of the barrier for run-up calculations is DWL2%. Additionally, because some wave setup influence is present in the laboratory tests that led to that R-Equation, the following adjustments are made to the calculation procedure for cases of run-up on barriers.

Runup Reduction Factor	Characteristic/Condition	Value of γ for Runup	
Roughness Reduction Factor, γ_r	Smooth Concrete, Asphalt, and Smooth Block Revetment	$\gamma_r = 1.0$	(D.2.8-10)
	1 Layer of Rock With Diameter, D. H_s / D = 1 to 3.	$\gamma_r = 0.55$ to 0.60	
	2 or More Layers of Rock. H_s / D = 1.5 to 6.	$\gamma_r = 0.5$ to 0.55	
	Quadratic Blocks	$\gamma_r = 0.70$ to 0.95. See Table V-5-3 in CEM for greater detail	
Berm Section in Breakwater, γ_b, B = Berm Width, $\left(\frac{\pi d_h}{x}\right)$ in radians	Berm Present in Structure Cross section. See Figure D.4.5-8 for Definitions of B, L_{berm} and Other Parameters	$\gamma_b = 1 - \frac{B}{2L_{berm}}\left[1+\cos\left(\frac{\pi d_h}{x}\right)\right], 0.6 < \gamma_B < 1.0$ $x = \begin{cases} R \text{ if } \frac{-R}{H_{mo}} \le \frac{d_h}{H_{mo}} \le 0 \\ 2H_{mo} \text{ if } 0 \le \frac{d_h}{H_{mo}} \le 2 \end{cases}$ (D.2.8-11) Minimum and maximum values of γ_b = 0.6 and 1.0, respectively	
Wave Direction Factor, γ_β, β is in degrees and = 0° for normally incident waves	Long-Crested Waves	$\gamma_\beta = \begin{cases} 1.0, 0 < \lvert\beta\rvert < 10^\circ \\ \cos(\lvert\beta\rvert - 10^\circ), 10^\circ < \lvert\beta\rvert < 63^\circ \\ 0.63, \lvert\beta\rvert > 63^\circ \end{cases}$ (D.2.8-12)	
	Short-Crested Waves	$1 - 0.0022\lvert\beta\rvert, \lvert\beta\rvert \le 80^\circ$ $1 - 0.0022\lvert 80\rvert, \lvert\beta\rvert \ge 80^\circ$ (D.2.8-13)	
Porosity Factor, γ_P	Permeable Structure Core	$\gamma_P = 1.0$, $\xi_{om} < 3.3$; $\gamma_P = \frac{2.0}{1.17(\xi_{om})^{0.46}}$, $\xi_{om} >$ 3.3 and porosity = 0.5. for smaller porosities, proportion γ_P according to porosity . See Figure D.2.8-7 for definition of porosity (D.2.8-14)	

Figure 44: Values of *γ* parameters for the run-up equations (FEMA, 2007)

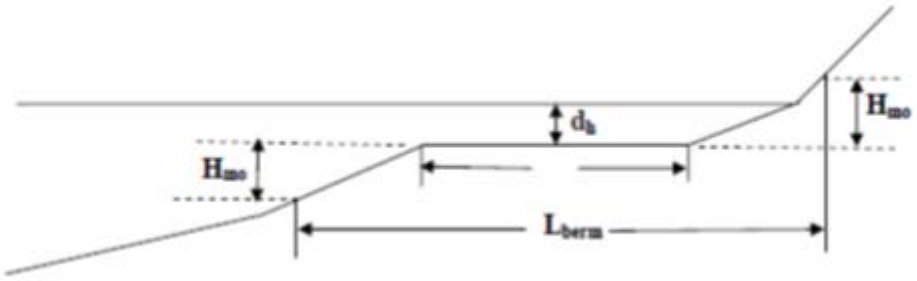

Figure 45: Berm parameters for wave run-up calculations (FEMA, 2007)

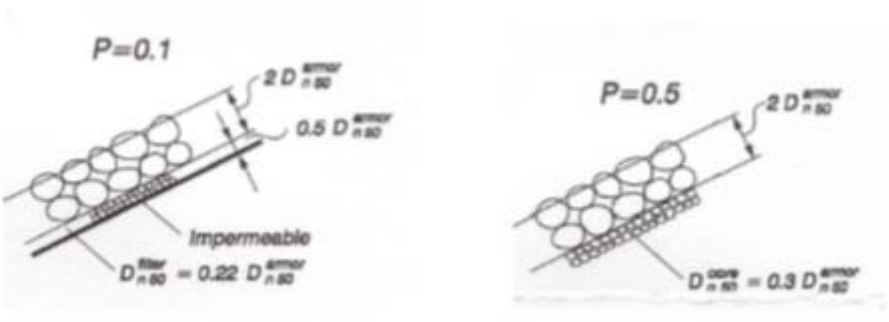

Figure 46: Structure porosity definition (FEMA, 2007)

For a smooth, impermeable structure of uniform slope with normally incident waves, each of the *γ* run-up reduction factors is 1.0.

In calculating the Iribarren number to apply in the last equation, it must be replaced H_o with H_{mo} and replace T with $T_{m\text{-}1.0}$ (the spectral wave period). H_{mo} and $T_{m\text{-}1.0}$ are calculated as:

$$\begin{cases} H_{mo} = 4.0\sqrt{m_o} \\ T_{m-1.0} = \dfrac{T_p}{1.1} \end{cases} \quad (66)$$

where H_{mo} is the spectral significant wave height at the toe of the structure and T_p is the peak wave period. In deep water, H_{mo} is approximately the same as H_s, but in shallow water, H_{mo} is 10-to15-percent smaller than the H_s obtained by zero up crossings (van der Meer, 2002). In many cases, waves are depth limited at the toe of the structure, and H_b can be substituted for H_{mo}, with H_b calculated using a breaker index of 0.78 unless it can be justified a different value. The breaker index can be calculated based on the bottom slope and wave steepness by several methods, as discussed in the CEM (USACE, 2003).

Run-up on structures is very dependent on the characteristics of the near shore and structure geometries. Hence, better run-up estimates may be possible with other run-up equations for particular conditions. See the CEM (USACE, 2003) for a list of presently available methods and their ranges of applicability. As an alternative, it's possible to use a numerical simulation with an interaction wave-structure model.

Finally, the flood Hazard Zone Limit (HZL) must be identified. Its limits and boundaries will be a result from the wave run-up analyses and wave overtopping rates determined during the coastal hydraulics phase.

A table of results should be provided as a summary by transect of the still water elevation, wave setup, maximum wave crest elevation, wave run-up elevations, and overtopping rates.

9.4.4 Summary of analysis steps

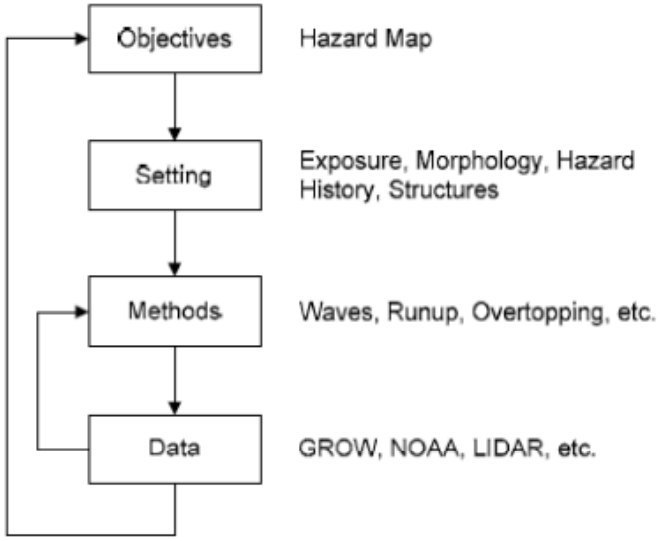

Figure 47: Summary of the main steps of Coastal Flood assessment (FEMA, 2007)

10.0 PROOF OF CONCEPT

A simple proof-of-concept example is proposed in order to validate and calibrate the hazard methodologies proposed in the previous sections: the objective is to check if, for each hazard type, the proposed methodology is applicable to the CI. All previously described steps and parameters should be covered in the analysis, from the definition of the source event to the estimation of the distributed IMs at the sites (see Figure 48): based on the type of component and the type of hazard considered, the spatial definition of the selected IMs (e.g. point-like, line-like or area-like definition) will have to be tested and made compatible with the simple constraints of this validation test. For each hazard it should be verified that the model proposed allows for a complete and sufficient description of the relevant IM at the site of the vulnerable infrastructure, with no need for further assumptions on the part of the user.

The application to this simple test is also an opportunity to explicitly identify limits of applicability of the hazard methodology proposed and associated uncertainties.

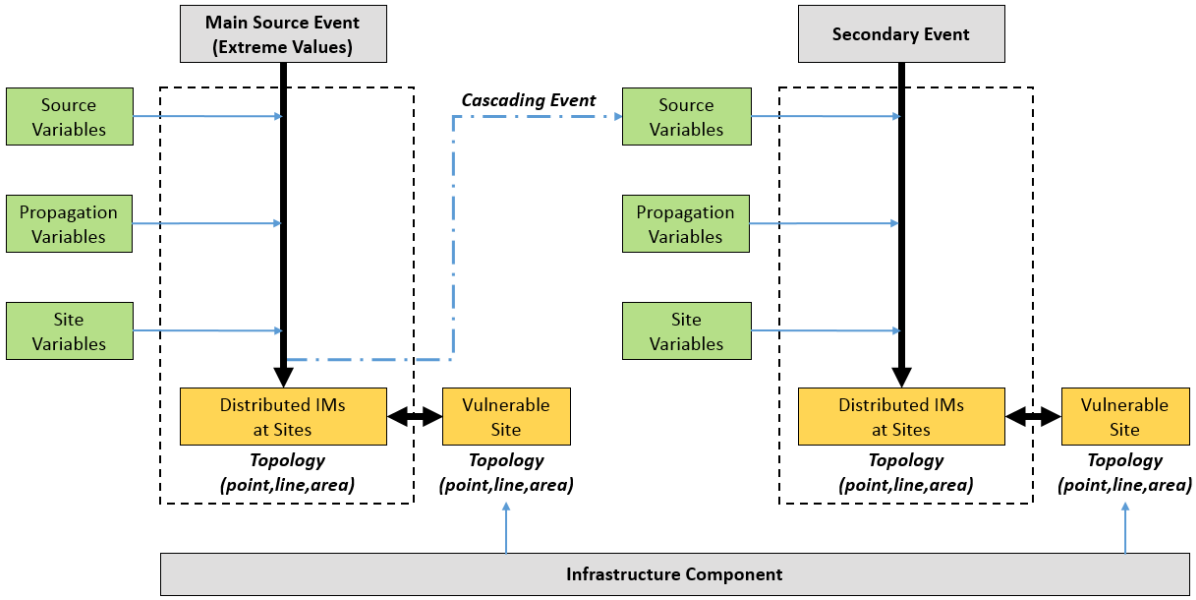

Figure 48: Presentation of the computation process (rectangle in dashed line) that is expected in the case-study, from the source event to estimation of IMs

10.1 Description

The hazard models presented in the previous sections are tested on a simple virtual proof of concept (see Figure 49): the aim of this exercise is to examine some issues related to the differences that are inherent to the various hazard types considered. The choice of a virtual application is motivated by the need to concentrate on the resolution of the technical issues without clouding the process with inexistent or incomplete data.

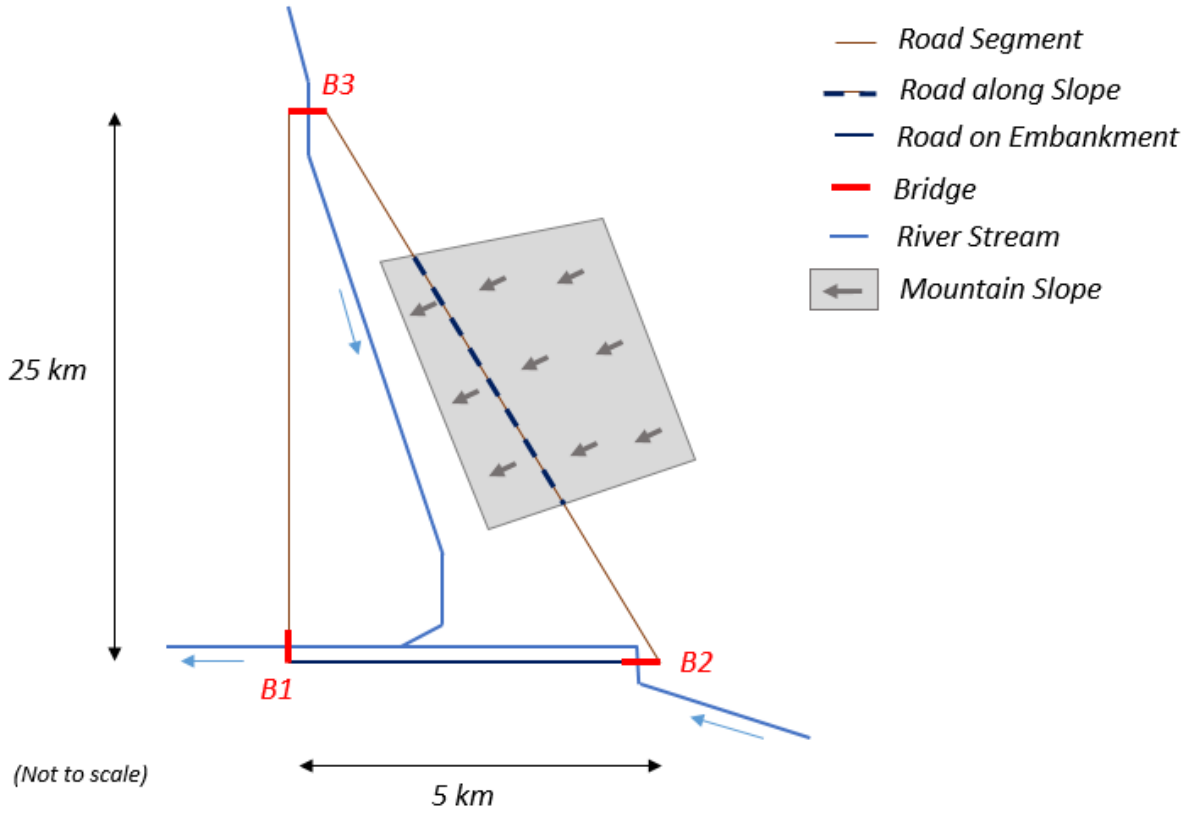

Figure 49: Layout of the proposed virtual application, with its different components

The application site is arbitrary located somewhere around Northern Central Italy. A virtual road network is imagined, with the following components:

- Plain road segments, connecting B1 to B3 and B2 to B3;
- A road on an embankment, connecting B1 to B2;
- A road along a slope, on the B2-B3 segment;
- Three bridges (B1, B2, B3): B1 and B3 are assumed to be the same structure, with a span length of 48.8m, while B2 is assumed to be 30m long.

The following hazard events are considered in the application:

- Earthquakes: different scenarios can be tested, by varying parameters such as the location of the seismogenic areas, the seismicity level of the area, or even the soil type.
- Landslides: they are expected to happen mainly on the mountain slope, due to occurrence of earthquakes (ground shaking) or heavy rainfall (soil saturation). Ground failure (lateral spreading) could also happen at the level of the embankment road, and even plain road segments (depending on the soil type).
- Fluvial floods due to the presence of the river streams.
- Pluvial floods due to heavy rainfall.
- Scour at bridges due to the fluvial floods.

10.2 Application: Earthquakes

In this section, the PGA values are estimated at the location of the three bridges, for both 4975- and 9950-year return periods.

Following the suggested approach (see subsection 5.3.1) a rectangular seismic area source about 100 km around the virtual infrastructure depicted in Figure 50 is selected.

A preliminary seismicity model has been developed to test the complete procedure for obtaining ground-motion values affecting the proposed virtual infrastructure. This model includes the generation by Monte Carlo simulation of 100 synthetic earthquake subcatalogues that are 99,500-year long (for a total catalogue length of 9,950,000 y), using four sets of magnitude-recurrence parameters, four sets of focal depth values, and four sets of maximum magnitude values. A weight is assigned to each set. Values are selected from averages of SHARE area sources in Northern Italy (Woessner et al., 2013). Alternatively, seismicity parameters can be randomly chosen from a uniform distribution. The Monte Carlo simulation assumes a stationary Poisson process of earthquake occurrence.

Table 15 summarizes the values assigned to each parameter-set (Minimum magnitude is fixed to M_w=4.5).

Table 15: Seismicity parameters (b, N0: activity parameters for a tapered Gutenberg-Richter recurrence relation)

	Magnitude-recurrence		
	b	N_0	weight
Set 1	1.0	300	0.20
Set 2	1.0	1,000	0.50
Set 3	1.0	3,000	0.20
Set 4	1.0	9,000	0.10
	Focal depth		
	depth (km)		weight
Set 1	2		0.10
Set 2	5		0.20
Set 3	10		0.50
Set 4	20		0.20
	Maximum magnitude (M_w)		
	M_{max}		weight
Set 1	6.5		0.15
Set 2	7.0		0.50
Set 3	7.5		0.30
Set 4	8.0		0.05

Figure 50 shows, as an example, a plot of one of the 100 generated 99,500-year subcatalogues in the virtual area source considered (around 200 km x 200 km). According to the simulation method, events are located in the area source by picking a randomly drawn point from a grid inside the source.

Three ground motion prediction models, based on the weighted average of several Eastern North America models, as proposed by Atkinson and Adams (2013) for B/C site conditions (V_{S30}=760 m/s), are used. This approach defines a lower, central, and upper GMPE, giving weights of 0.25, 0.50, and 0.25 respectively.

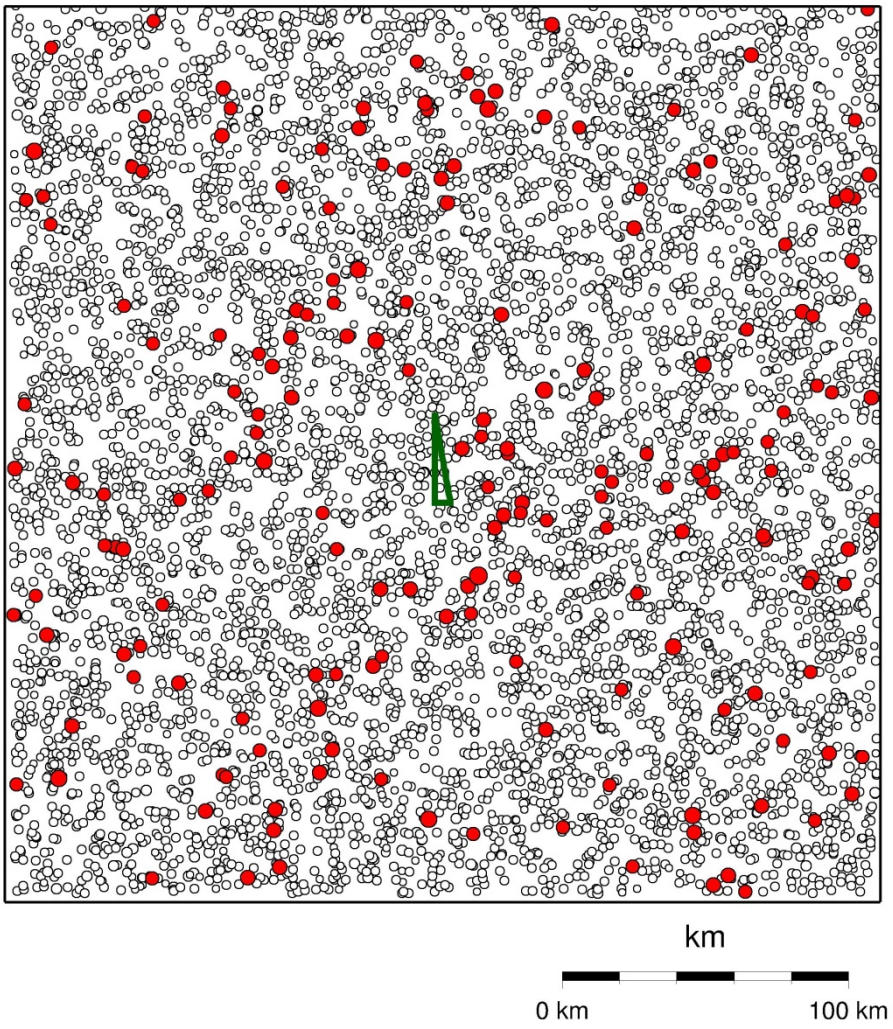

Figure 50: Example of a synthetic 99,500 year subcatalogue 4.5 ≤ Mw ≤ 8.0 (red dots: Mw ≥ 6.0) generated in the defined single source area surrounding the virtual infrastructure (green triangle)

In this application, calculations are performed to estimate the PGA in B/C site conditions with 1% probability of exceedance in 50 years (equivalent to 4975-year return period), and with 1% probability of exceedance in 100 years (equivalent to 9950-year return period). As an example, Mean-PGA hazard values for the area where the virtual infrastructure is located are mapped in Figure 51.

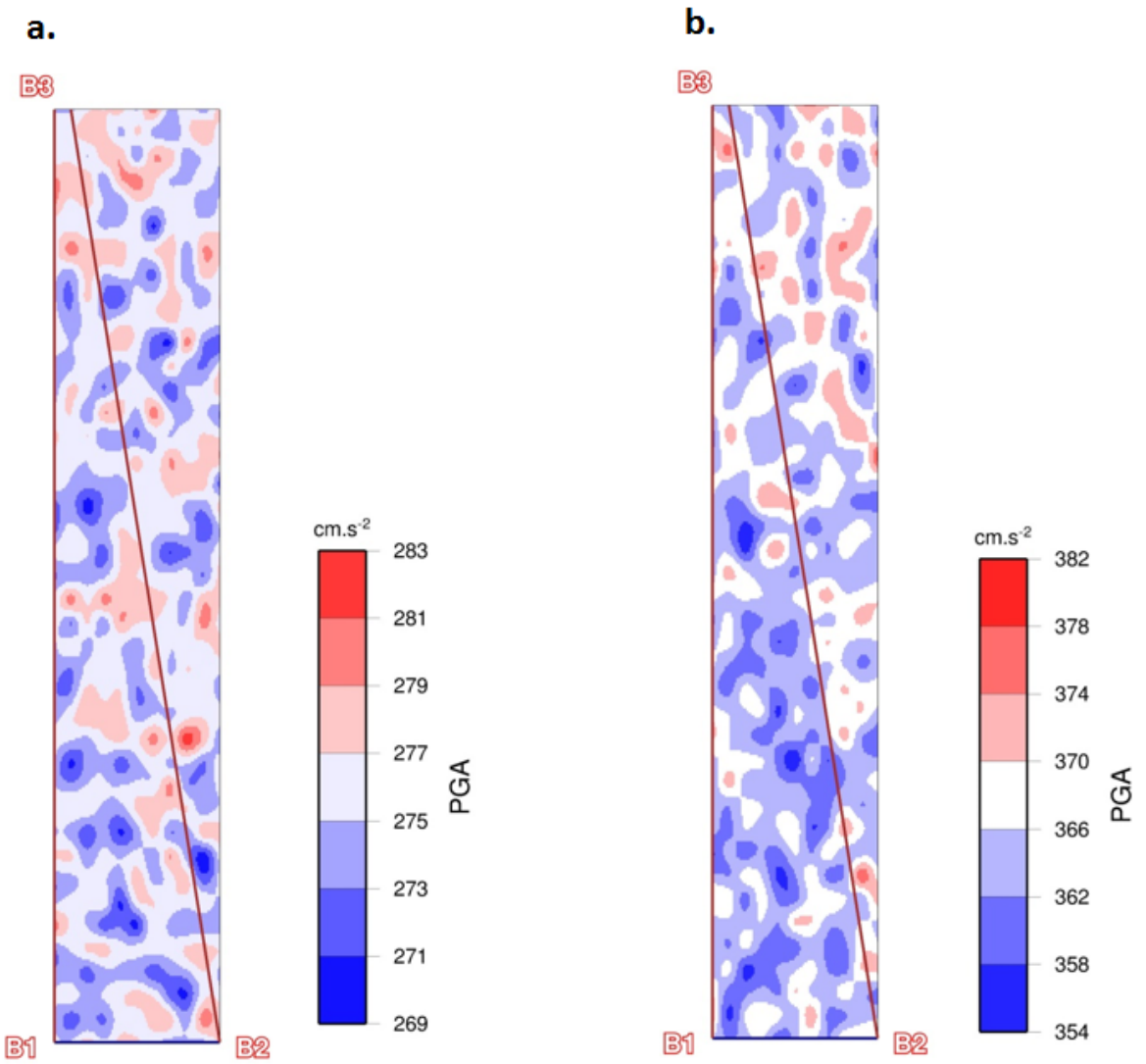

Figure 51: Mean PGA hazard values for B/C site conditions in the virtual infrastructure with (a) 1% probability of exceedance in 50 years (4975-year return period), and with (b) 1% probability of exceedance in 100 years (9950-year return period)

Mean PGA individual hazard curves, along with plots of fractiles of extreme values in 4975-year windows (mixing aleatory and epistemic uncertainty), and the contribution of different magnitude-distance bins (deaggregation) to the largest values of PGA for a 1% probability of exceedance in 50 years are obtained for the three bridges (B1, B2, B3) in the virtual infrastructure. Plots are summarized in Figure 52.

a.

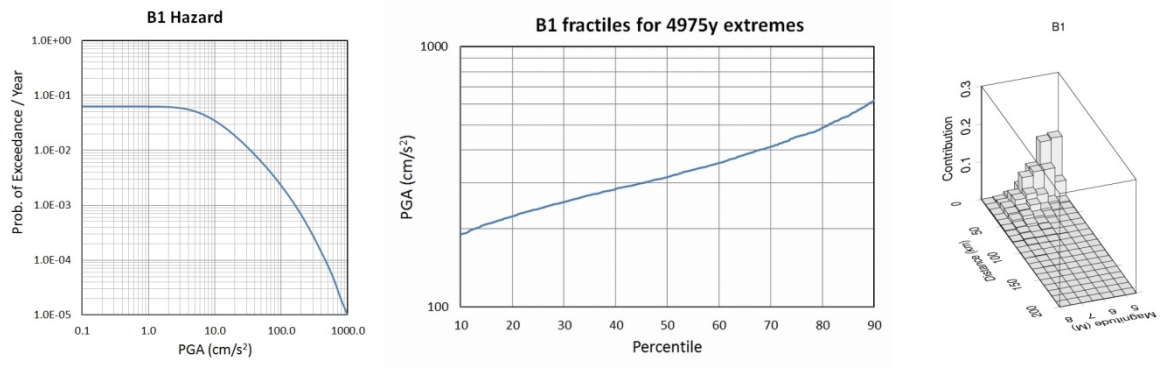

b.

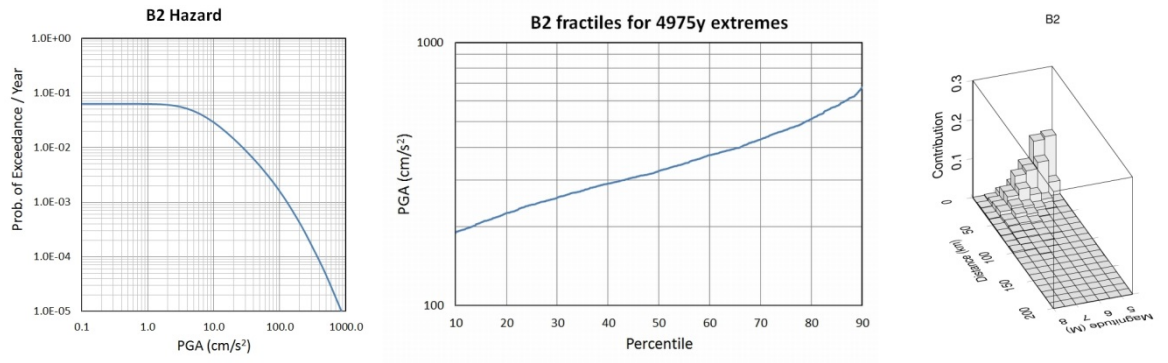

c.

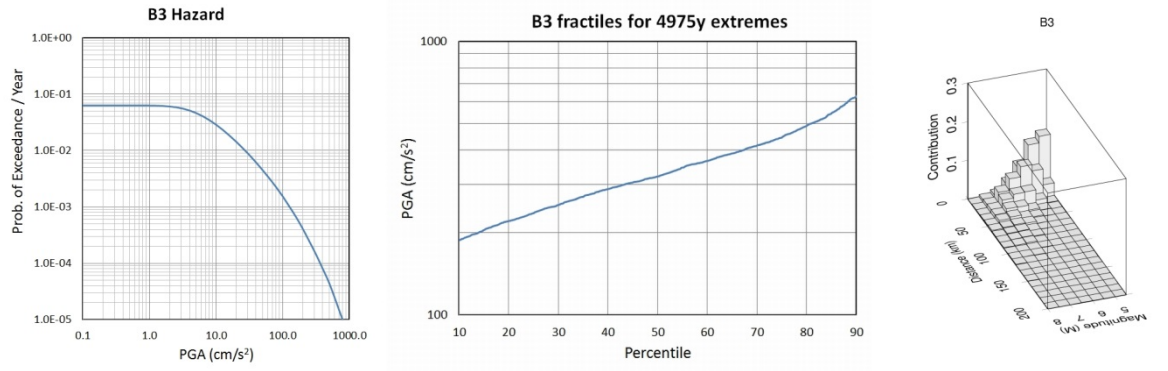

Figure 52: Mean-PGA hazard curves, fractiles of extreme values, and deaggregation of largest values of PGA for a 1% probability of exceedance in 50 years (4975-year return period) in the three bridges of the virtual infrastructure. (a) Bridge B1, (b) Bridge B2, (c) Bridge B3

Synthetic ground-motion time histories can be generated, using, e.g., stochastic point-source or finite-fault modelling (random horizontal component of acceleration), by selecting specific percentiles from the calculated maximum amplitudes / extreme values (e.g., fractile plots in Figure 52) consistent with the performance level expected for the CI. Alternatively, they can be generated selecting largest contributions obtained from the deaggregation analysis (e.g., deaggregation plots in Figure 52).

As an example, the contributions representing the 90th percentile of the maximum ground motions (PGA) for a 1% probability of exceedance in 50 years (4975-year return period) for each one of the

three bridges (B1, B2, B3) in the virtual infrastructure are given in Table 16. A realization of the corresponding synthetic time-histories generated by stochastic finite-fault modelling (random horizontal component of acceleration), is shown in Figure 53.

Table 16: 90th percentile of maximum PGA with 1% probability of exceedance in 50 years (4975-year return period) for the three bridges (B1, B2, B3) in the virtual infrastructure. Mw: Moment magnitude. Depi: Epicentral distance.

Bridge	M_w	D_{epi} (km)	PGA (g)
B1	6.3	13	0.63
B2	5.8	9	0.69
B3	5.3	11	0.64

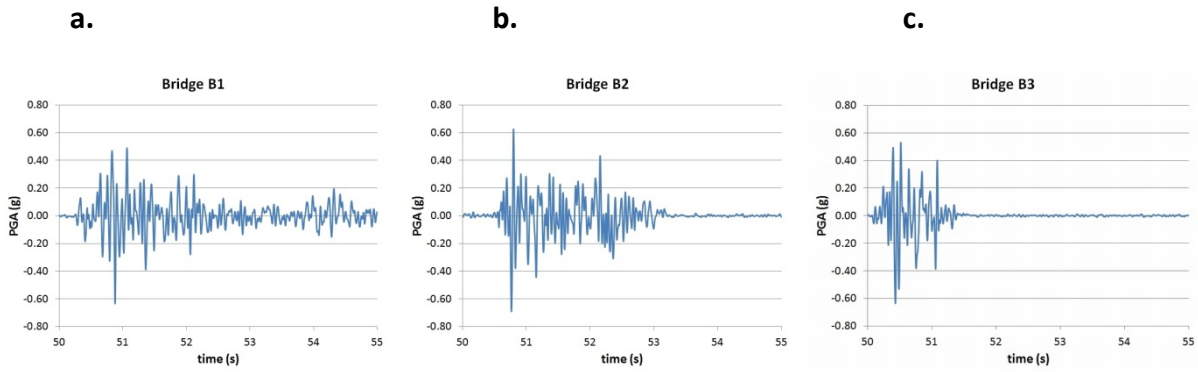

Figure 53: Examples of synthetic time histories (random horizontal component of acceleration) compatible with the 90th percentile of the maximum ground motions (PGA) for a 1% probability of exceedance in 50 years (4975-year return period). (a) Bridge B1, (b) Bridge B2, (c) Bridge B3

10.3 Application: Landslides

In this section, the sliding displacement values (i.e. D in m) are estimated for the slope along the road, for different values of PGA and soil saturation level.

10.3.1 Earthquake-triggered landslide hazard

The soil properties are presented in Table 17. The soil is considered to be sandy gravel with high friction and no cohesion

Table 17: Soil properties

Parameter	**Value**
Effective Cohesion (c')	0 kN/m^2
Internal Friction Angle (φ')	30^o
Unit weight (w)	19 kN/m^3
Failure surface thickness (t)	1 m
Saturation ratio (m)	0.2

Using Equations (18) to (22), the ln$D$ value and associated standard deviation can be calculated. Using an example from the literature (Rathje & Saygili, 2009), the PGA value was taken as 0.33g, the earthquake magnitude, M, was taken as 7 and the PGV value was taken as 30cm/s. Figure 54

illustrates the effect of k_y on the sliding displacement (D), for both the scalar model and the vector model.

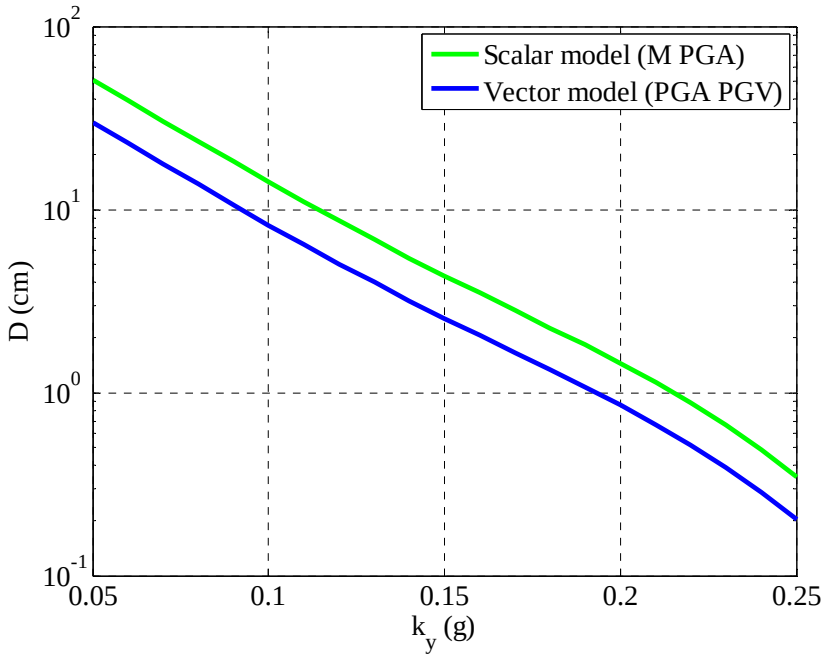

Figure 54: Effect of k_y on Sliding displacement

Saygili & Rathje (2009) noted that the most efficient models aim to minimise the standard deviation. The vector model proposed in Equations (20) and (21) provided lower standard deviations. Therefore, only the vector model is assessed in the current anlysis. Figure 55 illustrates the effect of the slope angle on the sliding displacement for the soil properties used.

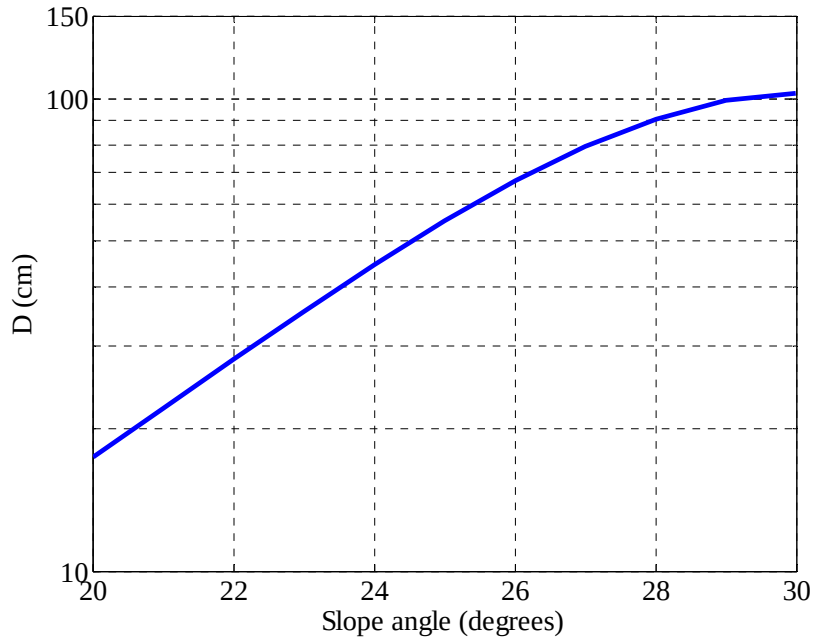

Figure 55: Effect of slope angle on sliding resistance (m = 0.2)

For the current analysis, the slope angle was taken as 20°. The effect of rainfall on earthquake induced landslides may be shown by the saturation ratio. this value was taken as 0.2 in the current case study. However, it is clear from Figure 56 that the effect of the saturation ratio on the sliding displacement is similar to that of the slope angle.

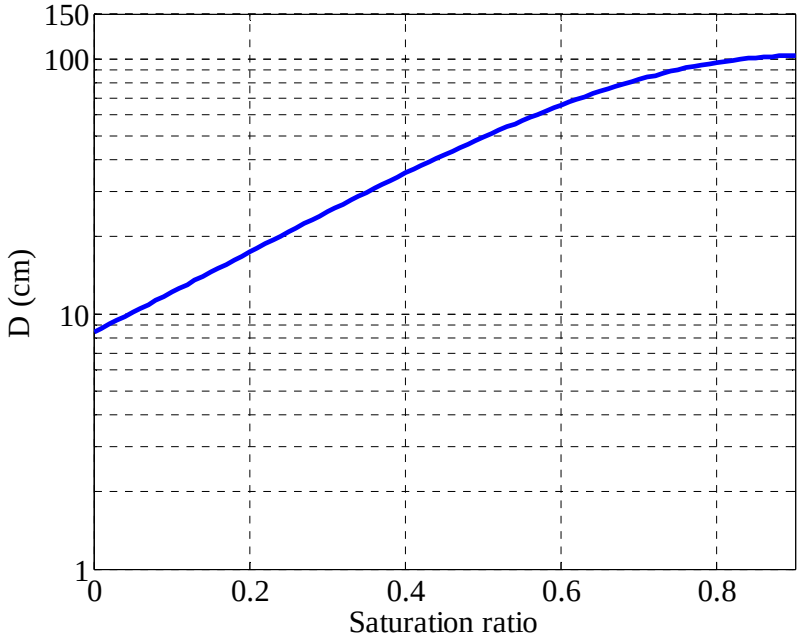

Figure 56: Effect of saturation on sliding resistance (slope = 20°)

Considering the current case study with a saturation ratio of 0.2 and a slope angle of 20°, the vector model provides an ln*D* value of 2.86. This is considered as the mean value of the lognormal distribution. Taking the exponential function of this value leads to a median value of 17.45 cm. The standard deviation of this function, given by Equation (21), is calculated as 0.5173 cm. The CDF of the sliding displacement is illustrated in Figure 57.

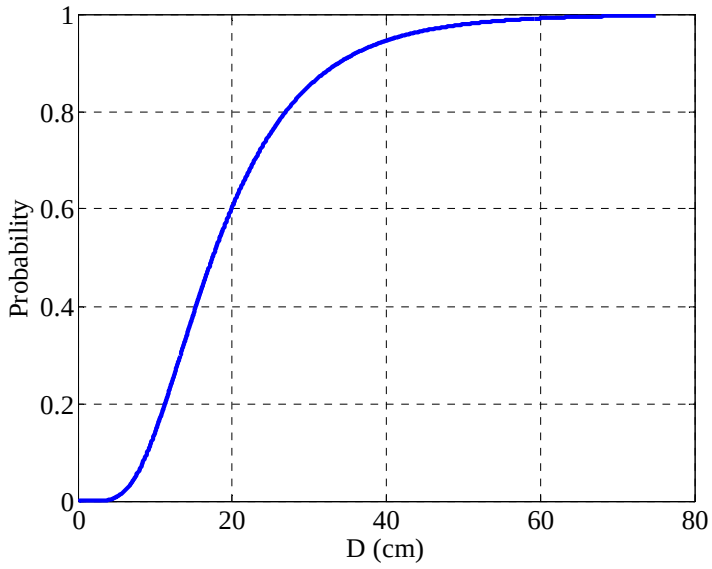

Figure 57: CDF of sliding displacement

Existing fragility functions from HAZUS (NIBS, 2004) may be used to select a level of landslide displacement indicative of damage rates for the current case study. The median displacement levels considered to constitute slight, moderate and extensive damage on major roads (highways) are 30cm, 60cm, and 150cm, respectively. Using the CDF in Figure 57, the probability associated with each displacement can be quantified at the given PGA level:

- P (D > 30 | PGA = 0.33g) = 0.1477
- P (D > 60 | PGA = 0.33g) = 0.0085
- P (D > 150 | PGA = 0.33g) = 1.6 x 10^{-5}

The spatial variation of the soil properties and PGA values along the slope may result in a variation in the probability associated with each damage level at different points along the road surface. The same procedure could also be applied to the road embankment (section B1 – B2).

10.3.2 Rainfall-triggered landslide hazard

The rainfall triggered hazard model presented in the previous sections is tested on the same simple virtual proof-of-concept example. The same topographical and geotechnical parameters used for the earthquake-triggered model are adopted. The statistical distribution types and coefficients of variations assigned for each parameter are presented in Table 18.

Table 18: Parameters adopted for virtual case study

Parameter	Value	Distribution	COV
Effective Cohesion (*c'*)	0 kN/m^2	Normal	0.1
Internal Friction Angle (*φ'*)	30^o	Normal	0.1
Unit weight (*w*)	19 kN/m^3	Normal	0.02
Failure surface thickness (*t*)	1 m	-	-
Saturation ratio (*m*)	0.2	-	-

Infiltration of rainfall is not explicitly modelled here, but instead a simplified calculation procedure is carried out. An increase in volumetric water content is chosen to correspond with the increase from the initial degree of saturation of 0.2 (as in earthquake-triggered model) to unity, and the related suction is assumed to decrease from 10 kPa to 0 kPa for this event. The probability of failure then increases from $P_f = 5.027x10^{-12}$ to $P_f = 0.0011$ following rainfall event.

In this simplified case study, the slope is completely uniform in terms of geotechnical parameters and slope angle. Subsequently, the entire slope has an identical probability of failure and all exposed road segments will be equally affected. In reality, the topography and spatial variability of soils (and their parameters) will result in different probabilities of failure across slope's length.

Furthermore, different failure depths will result in different landslide volumes. Each failure depth will have different P_f depending on the rainfall triggering event, i.e. as the duration and intensity increase, the slip depth increases. The landslide volume is directly correlated with the level of damage to the infrastructure element. Thresholds for damage levels and further development of the model will ensue in Task3.2 in developing fragility curves for rainfall triggered landslides.

For this particular case study and example calculation, this would mean that the 13 km long segment of the road is possibly affected by the 42 million m^3 of the sliding mass from the upper slope or

cutting (not all of it reaching road) with average depth of 1 m. According to the case study situation, there is also a possibility of simultaneous instabilities on the embankment downslope.

10.4 Application: Floods

In this section, the flow discharge and water elevation are estimated at the river cross-section under bridge 1, for a rainfall return period of 500 years.

10.4.1 Maximum daily rainfall

In order to find the maximum daily rainfall of the study area, starting data have been obtained from the Meteorological Institute and the Spanish publication of the Ministry for Development "Maximum Daily Rainfall in Mainland Spain" (General Roads Directorate, 1999).

In this example, the river stream between B1 and B2, as well as the flooding upstream and downstream of the bridge B1 are going to be studied.

The chosen rainfall stations of the Meteorological Institute are the ones closest located to the road under study with data record over a period of time longer than 15 years. Usually, based on current practice, three or four stations with complete data series in each catchment area start to be sufficient, additional stations will provide more accuracy to the rainfall calculation. Regarding the length of the time series, it is usually recommended to have the longest possible rainfall data (30 years at least); and data series also have to be uniform and continuous. Rain data series of less than 10 - 15 years do not contain enough data to reach definitive conclusions.

Table 19: Rainfall stations used in the study

Station number	Station name	Geographical coordinates		Working period	Complete / incomplete years	Longest complete series
		x	y			
1032	Station 1	44º06'46''	11º17'09''	1925-1987	43/11	1969-1983
1035	Station 2	44º05'49''	11º12'20''	1959-2008	17/33	1978-1995

The maxima adjustment method has been applied in each rainfall station, for different return periods, using two distribution functions: Gumbel distribution and SQRT-Etmax distribution. Once the maximum daily rainfall is calculated by each method, the results are compared and the highest one will be chosen (marked in bold):

Table 20: Distribution parameters for Station 1 (1032)

Return Period	SQRT-ET	Gumbel	Maximum rainfall map
50	150	139	154
100	168	152	174
500	214	182	**226**

Table 21: Distribution parameters for Station 2 (1035)

Return Period	SQRT-ET	Gumbel	Maximum rainfall map
50	166	152	156
100	187	166	176
500	**240**	199	228

In order to obtain the calculation of rainfall for the catchment areas under consideration, once the maximum daily rainfall has been obtained for each station, the Thiessen networks method or the isohyets method (this is usually used for large catchment areas and with a sufficient number of rainfall stations) is applied. But in this case, as the results are very similar and the station 1032 has longer complete data series, this step will be ignored. The maximum value from the stations is used because it is the worst possible scenario: the most conservative values are always adopted in order to be on the safe side.

10.4.2 Flow calculation

To obtain the calculation flows in small catchment areas (concentration time less than 6 hours), the modified rational method must be used, the formulation of which is shown below:

$$Q = \frac{C \cdot I \cdot A}{3.6} \cdot K_u \quad (67)$$

Where:

C = run-off coefficient

I = rainfall intensity [mm/h]

A = catchment area [km^2]

Q = design discharge [m^3/sec]

K_u = the uniformity coefficient

The different variables of the formula (especially C and I) are calculated according to the national standards of each country. For this imaginary example, the Spanish national standards are being used.

The use of the previous formula provides lower flow values than the method in the 5.2-IC standard. The only difference with it is the introduction of two coefficients:

- Area reduction factor: which considers that the distribution of the rainfall is not geographically uniform, is not simultaneous throughout the catchment area and corrects the rainfall.

$$P_d^* = P_d \cdot K_A \quad (68)$$

$$K_A = 1 - \frac{\log A}{15} \quad (69)$$

- Uniformity coefficient which takes into account the error introduced in the temporal uniformity hypothesis for the rainfall as the size of the catchment area increases. Its average value in a specific catchment area will fundamentally depend on the value of its concentration time and for practical purposes the effect of the other variables such as the rainfall intensity of the climate, etc, can be ignored.

$$Ku = 1 + \frac{T_c^{1,25}}{T_c^{1,25} + 14} \quad Ku = 1 + \frac{T_c^{1,25}}{T_c^{1,25} + 14} \quad (70)$$

The rest of the parameters involved in both formulas for the rational method are:

10.4.3 Run-off coefficient

The run-off coefficient of catchment areas is calculated as follows:

$$C = \frac{\left[(P_d / P_o) - 1\right] \times \left[(P_d / P_o) + 23\right]}{\left[(P_d / P_o) + 11\right]^2} \quad (71)$$

Where:

P_d [mm]: Maximum daily rainfall (corrected by the area reduction factor, in the case of the modified rational method).

P_o: run-off threshold as a function of the type of terrain, corrected by a coefficient that reflects the regional variation of the humidity in the soil at the start of important rainfalls. It includes an increase of the order of 100% to avoid over-valuing the reference flow because of certain simplifications in the statistical handling of the hydro-meteorological method. The value of this reduction coefficient is obtained from Figure 2.5 of the 5.2-IC standard (see Figure 58).

Figure 58: Map of correction coefficient for run-off threshold (from Figure 2.5 of the 5.2-IC standard)

To estimate the value of the correction coefficient at each flow station, quintiles obtained from maximum flow series recorded in flow stations were compared with the ones estimated using the modified rational method. The adjustment was carried out for the 10-year return period, since for lower return periods the runoff measured by an aggregate procedure may not be correct, and higher return periods have greater uncertainty in its determination due to the limited length of the data series. From this contrast the value of the correction coefficient was determined in such a way that the fit between the quintiles obtained by both procedures is suitable, using a kriging process. Although the adjustment of correction coefficient has been made for a 10 year return period, it is used for all return periods. The run-off threshold is based in the Curve Number (CN) method of the US Soil Conservation Service. The runoff curve number was developed from an empirical analysis of runoff.

It should be checked that the run-off coefficient has been applied for each area, an average coefficient should never be used. Further, in the same catchment area, each rainfall datum may have its own, different, run-off coefficient since soggy ground does not have the same coefficient as totally dry ground.

Intensity

To calculate the intensity (*I*) for a specific return period, the 5.2-IC standard uses the following values:

- The concentration time T_c [h] relating to the average intensity of the rainfall can be deduced from the formula:

$$T_C = 0.3 \cdot \left(\frac{L}{J^{1/4}} \right)^{0.76} \quad (72)$$

Where:

L [km]: the length of the main riverbed.

J [m/m]: its average gradient.

- The concentration time and the rainfall for the return period are used to calculate the intensity of the design rainfall with the formula:

$$I_{tc} = I_d \times \left[\frac{I_1}{I_d} \right]^{\frac{28^{0,10} - T_c^{0,10}}{28^{0,10} - 1}} \quad (73)$$

Where:

I_d is the average daily intensity for the design rainfall, that is, the maximum daily rainfall divided by 24 hours, in [mm/h].

I_1/I_d is the ratio between the hourly intensity and the average daily intensity for the area of the project; this value is obtained from Figure 2.2 of the 5.2-IC drainage standard (see Figure 59). These values are still applicable when considering consider low-probability high-consequence cases.

Figure 59: Isolines map I_1/I_d

Flow calculations made for each return period are represented in Table 22.

Table 22: Flow calculations for different return period

River	T [y]	Area [km^2]	P_d [mm]	P_d* [mm]	T_c [h]	P_o [mm]	Regional factor	P_o* [mm]	I_1/I_d	I_d [mm/h]	I [mm/h]	C	K_u	Q [m^3/s]
AB	50	5.98	154	146	1.04	26.4	1.5	40	9	6.1	53.5	0.33	1.07	31.61
AB	100	5.98	174	165	1.04	26.4	1.5	40	9	6.9	60.4	0.37	1.07	40.17
AB	500	5.98	226	214.3	1.04	26.4	1.5	40	9	8.9	78.5	0.47	1.07	64.93

Hydraulic modelling

For this study, *HEC-RAS* program (*River Analysis System*), developed by the *Hydrologic Engineering Center,* has been used. This program, starting from each of the cross sections through which water flows, and from the appropriate hydraulic parameters (flow, Manning roughness, type of flow data, steady or unsteady, etc.), gives as a result, among other variables, depth and velocity of water flow.

In order to define the stream system, some stations have been considered (*River Stations, RS*). Cross sections have been obtained, for each one of these *River Stations*, from the cartography of the area. For modelling, profiles of the cross sections to the axis which defines the riverstream have been extracted every 40 or 50 m, and an interpolation of profiles every 10 m has been made later. Two small bridges located downstream have been modelled to reproduce more faithfully the existing conditions.

Manning roughness coefficients used in the calculations are the following:

- Manning roughness coefficient in the central channel: n=0.035.
- Manning roughness coefficient in the banks: n=0.050.

With these data, a mixed flow regime calculation is performed with boundary conditions, relating to steady flow data upstream and downstream, for the 500 years return period flood.

Some of these data are empirical (like Manning roughness) and the rest are obtained with a deterministic model (like the flow). Only the maximum rainfall calculation is made in a statistical way: probability in the return period and a distribution function in the rainfall data.

Figures included below represent the water surface obtained in the calculation.

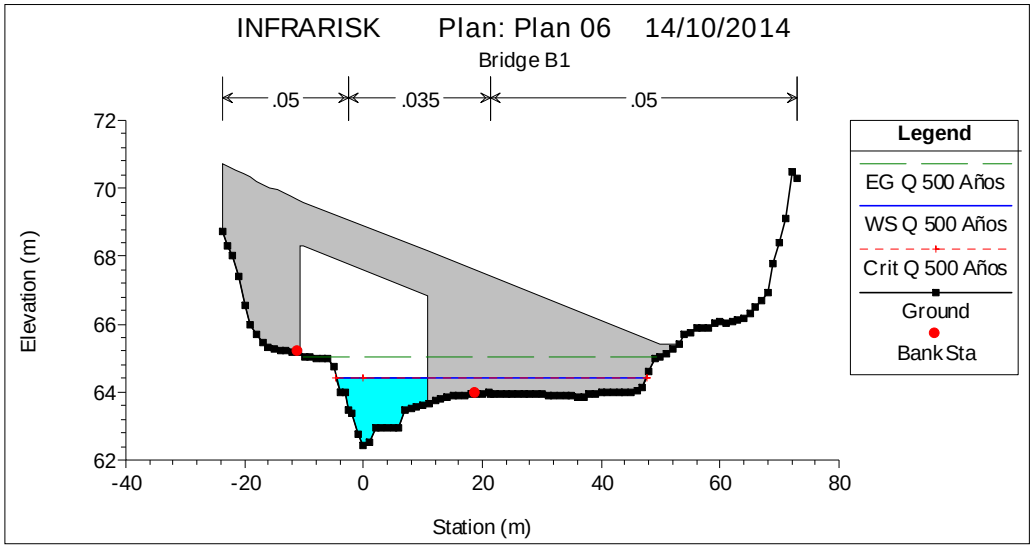

Figure 60: Upstream Bridge cross section (RS 525 BR U)

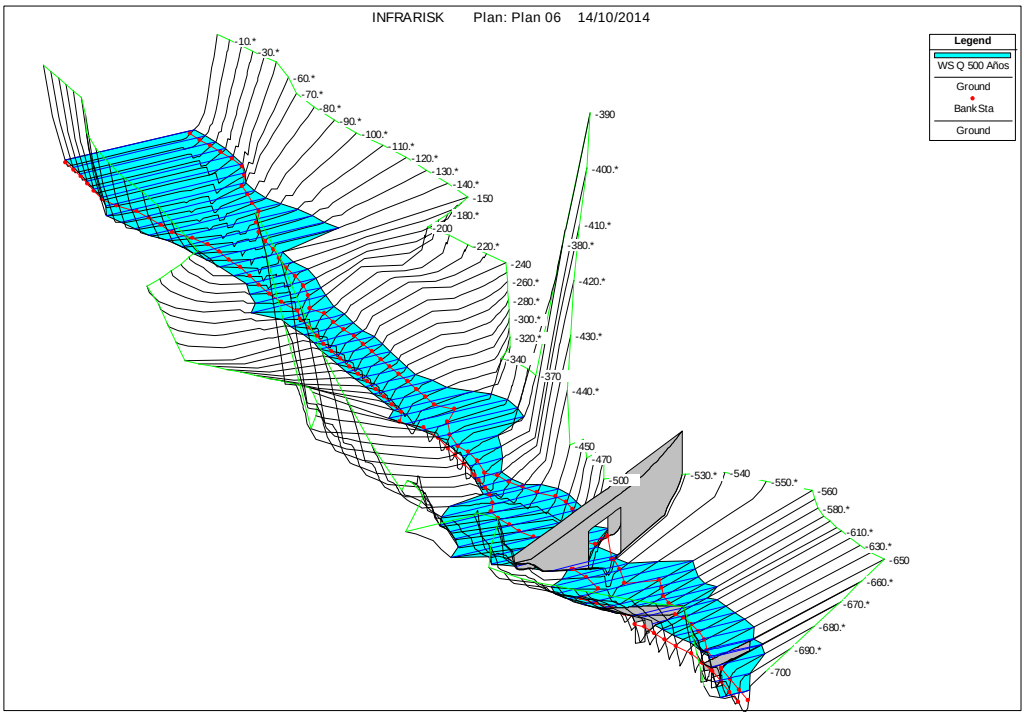

Figure 61: 3D plot of the 500 years return period flood

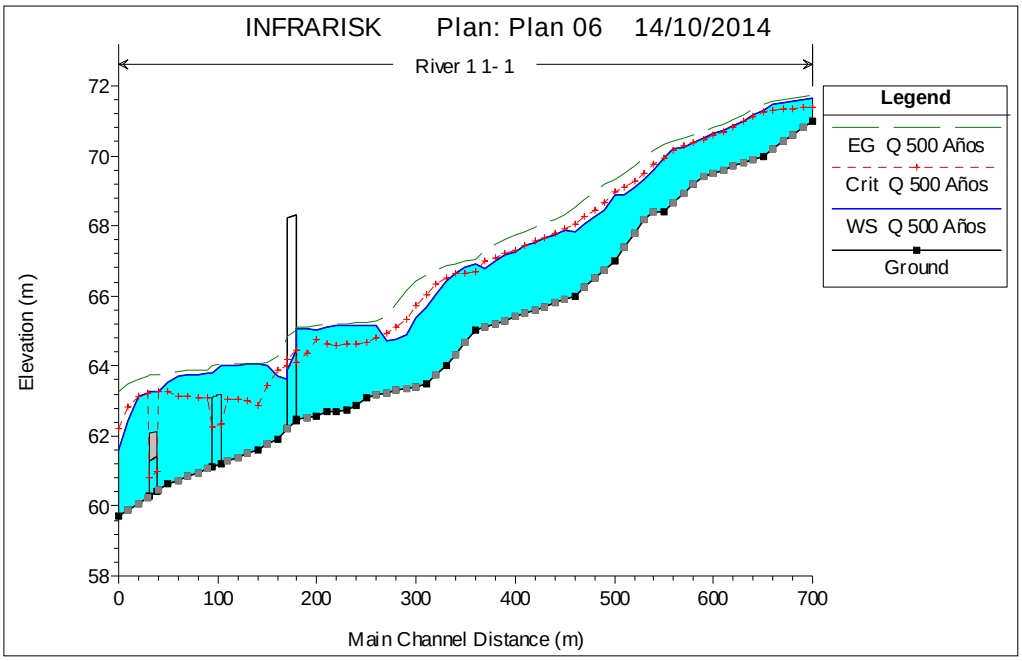

Figure 62: Longitudinal profile of the river

Table 23: HEC-RAS results for the successive sections of the river stream

River Station	Total Flow	Minimum Channel Elevation	Water Surface Elevation	Critical Water Surface	Energy Gradeline Elevation	Energy Gradeline Slope	Velocity Channel	Flow Area	Top Width	Channel Froude number
	[m^3/s]	[m]	[m]	[m]	[m]	[m/m]	[m/s]	[m^2]	[m]	
0	64.93	71	71.65	71.41	71.73	0.003419	1.24	52.71	84.71	0.49
-10.*	64.93	70.8	71.61	71.38	71.69	0.003685	1.26	51.97	86.61	0.51
-20.*	64.93	70.6	71.57	71.36	71.65	0.004054	1.28	51.04	88.97	0.53
-30.*	64.93	70.4	71.52	71.33	71.61	0.004527	1.31	49.92	90.63	0.56
-40.*	64.93	70.2	71.46	71.31	71.56	0.005336	1.36	47.89	91.68	0.6
-50	64.93	70	71.29	71.27	71.46	0.015553	1.87	34.87	92.28	0.97
-60.*	64.93	69.9	71.16	71.12	71.32	0.011967	1.77	37.57	92.14	0.86
-70.*	64.93	69.8	70.99	70.99	71.19	0.014418	2	34.8	91.6	0.96
-80.*	64.93	69.7	70.85	70.84	71.05	0.013	2	35.27	88.03	0.92
-90.*	64.93	69.6	70.71	70.71	70.92	0.012925	2.04	34.82	86.33	0.92
-100.*	64.93	69.5	70.63	70.58	70.8	0.009566	1.9	38.12	86.5	0.81
-110.*	64.93	69.4	70.51	70.48	70.7	0.008974	2.06	38.56	86.36	0.8
-120.*	64.93	69.19	70.38	70.38	70.61	0.0091	2.25	36.75	86	0.83
-130.*	64.93	68.93	70.24	70.27	70.51	0.009603	2.41	33.68	85.41	0.86
-140.*	64.93	68.67	70.19	70.14	70.41	0.006707	2.2	37.2	87.39	0.73
-150	64.93	68.41	69.95	69.95	70.31	0.011265	2.74	26.41	41.12	0.94
-160.*	64.93	68.42	69.6	69.76	70.15	0.019264	3.34	21.51	39.23	1.2
-170.*	64.93	68.2	69.33	69.51	69.93	0.022998	3.51	20.62	40.32	1.3
-180.*	64.93	67.8	69.1	69.28	69.7	0.022101	3.53	21.29	43.46	1.28
-190.*	64.93	67.4	68.9	69.1	69.5	0.019097	3.61	22.41	42.77	1.22
-200	64.93	67	68.87	68.99	69.34	0.008929	3.53	30.76	48.91	0.89
-210.*	64.93	66.75	68.42	68.66	69.17	0.021823	3.97	19.41	34.52	1.31
-220.*	64.93	66.5	68.27	68.44	68.95	0.018406	3.82	20.7	34.69	1.21
-230.*	64.93	66.25	68.04	68.26	68.75	0.021187	3.83	19.44	32.7	1.28
-240	64.93	66	67.83	68.06	68.53	0.023452	3.75	18.79	31.74	1.33
-250.*	64.93	65.9	67.89	67.92	68.32	0.011421	2.99	24.81	36.39	0.96

Table 23: HEC-RAS results for the successive sections of the river stream

River Station	Total Flow	Minimum Channel Elevation	Water Surface Elevation	Critical Water Surface	Energy Gradeline Elevation	Energy Gradeline Slope	Velocity Channel	Flow Area	Top Width	Channel Froude number
	[m^3/s]	[m]	[m]	[m]	[m]	[m/m]	[m/s]	[m^2]	[m]	
-260.*	64.93	65.8	67.76	67.79	68.2	0.011955	3.04	24.27	35.4	0.98
-270.*	64.93	65.7	67.66	67.67	68.08	0.011124	2.98	24.83	35.1	0.95
-280.*	64.93	65.6	67.52	67.55	67.97	0.01207	3.05	23.95	34.02	0.99
-290.*	64.93	65.5	67.42	67.43	67.85	0.011218	2.98	24.5	33.89	0.95
-300.*	64.93	65.4	67.27	67.29	67.73	0.012342	3.07	23.54	33.01	1
-310.*	64.93	65.3	67.17	67.2	67.6	0.011338	2.97	24.71	38.6	0.96
-320.*	64.93	65.2	66.98	67.08	67.46	0.01429	3.16	23.35	41.39	1.06
-330.*	64.93	65.1	66.8	66.98	67.31	0.016617	3.28	23.88	52.28	1.14
-340	64.93	65	66.9	66.68	67.03	0.003846	1.68	46.25	67.25	0.56
-350.*	64.93	64.67	66.82	66.65	66.98	0.003937	2.1	47.05	66.72	0.59
-360.*	64.93	64.33	66.64	66.64	66.93	0.005292	2.95	40.76	62.92	0.7
-370	64.93	64	66.45	66.52	66.86	0.005957	3.36	35.52	57.16	0.74
-380.*	64.93	63.74	66.05	66.33	66.75	0.011052	3.95	22.12	31.29	0.98
-390	64.93	63.47	65.69	66.01	66.59	0.017193	4.51	19	25.56	1.15
-400.*	64.93	63.41	65.36	65.72	66.41	0.016162	4.87	17.94	21.9	1.18
-410.*	64.93	63.35	64.88	65.31	66.17	0.031819	5.05	13.42	17.95	1.58
-420.*	64.93	63.29	64.77	65.11	65.79	0.028438	4.49	15	21.29	1.49
-430.*	64.93	63.23	64.73	64.93	65.44	0.023799	3.73	17.83	26.79	1.34
-440.*	64.93	63.17	65.14	64.81	65.29	0.00327	1.79	43.22	60.06	0.53
-450	64.93	63.11	65.17	64.68	65.25	0.001621	1.24	61.73	76.91	0.37
-460	64.93	62.89	65.17	64.62	65.23	0.00128	1.12	68.97	84.81	0.33
-470	64.93	62.74	65.15	64.62	65.21	0.001392	1.18	66.52	82.93	0.35
-480	64.93	62.71	65.14	64.6	65.2	0.001393	1.19	66.92	84.52	0.35
-490	64.93	62.69	65.11	64.65	65.18	0.001728	1.34	63.3	84.94	0.39
-500	64.93	62.57	65.02	64.77	65.16	0.002626	2.07	59.36	89.46	0.5
-510.*	64.93	62.53	65.06	64.38	65.12	0.000933	1.17	77.96	78.81	0.3
-520	**64.93**	**62.48**	**65.09**	**64.08**	**65.1**	**0.000579**	**0.97**	**86.12**	**73.36**	**0.25**
-525	**Bridge**									
-530.*	64.93	62.2	63.63	63.99	64.81	0.072533	4.83	13.71	32.23	2.17
-540	64.93	61.92	63.7	63.86	64.28	0.020517	3.47	21.84	43.34	1.24
-550.*	64.93	61.76	64.01	63.45	64.1	0.001546	1.54	64.08	70.33	0.39
-560	64.93	61.6	64.05	62.88	64.07	0.000289	0.69	108.37	90.18	0.17
-570.*	64.93	61.49	64.04	62.98	64.07	0.000424	0.83	93.76	83.23	0.2
-580.*	64.93	61.38	64.02	63.03	64.06	0.000595	0.99	81.54	76.1	0.24
-590.*	64.93	61.27	63.99	63.05	64.05	0.000759	1.13	71.91	69.28	0.27
-600	Culvert									
-610.*	64.93	61.06	63.8	63.08	63.9	0.001456	1.46	52.39	50.39	0.37
-620.*	64.93	60.95	63.77	63.1	63.88	0.00164	1.54	50.14	48.4	0.39
-630.*	64.93	60.84	63.74	63.12	63.86	0.001887	1.65	47.81	47.27	0.42
-640.*	64.93	60.73	63.69	63.16	63.84	0.002294	1.84	44.94	45.85	0.46
-650	64.93	60.62	63.55	63.26	63.8	0.003724	2.52	38.17	42.06	0.58
-660.*	64.93	60.44	63.27	63.26	63.73	0.006603	3.38	29.04	34.96	0.77
-665	Culvert									
-670.*	64.93	60.25	63.24	63.21	63.7	0.005709	3.41	30.25	34.53	0.72
-680.*	64.93	60.07	63.12	63.12	63.64	0.005486	3.58	29.39	35.35	0.72
-690.*	64.93	59.88	62.43	62.82	63.5	0.011944	4.76	17.77	23.34	1.05
-700	64.93	59.7	61.62	62.2	63.28	0.025576	5.85	13.44	19.21	1.49

10.5 Application: Scour

In this section, the scour depths (i.e. general, contraction and local scour) are estimated at the location of bridge 1, using the 500-year return period flood levels computed in previous section.

The calculation is made in a deterministic way, as it is included in the text "*Hydrometeorological methods. Simulate the rainfall-runoff process, usually using deterministic models of varying complexity.*"

The probability is included in the return periods used in the Maximum rainfall calculation:

$$P = 1 - \left(1 - 1/T\right)^N \quad (74)$$

10.5.1 Introduction

The starting data for this scour study had been obtained from the hydraulic modelling contained in the previous section. For this example scour will be studied at the bridge B1.

After considering the results of this hydraulic modelling, we conclude the only subject of study of scour is at abutment nº 1, since the abutment nº 2 is not affected by water (see Figure 63).

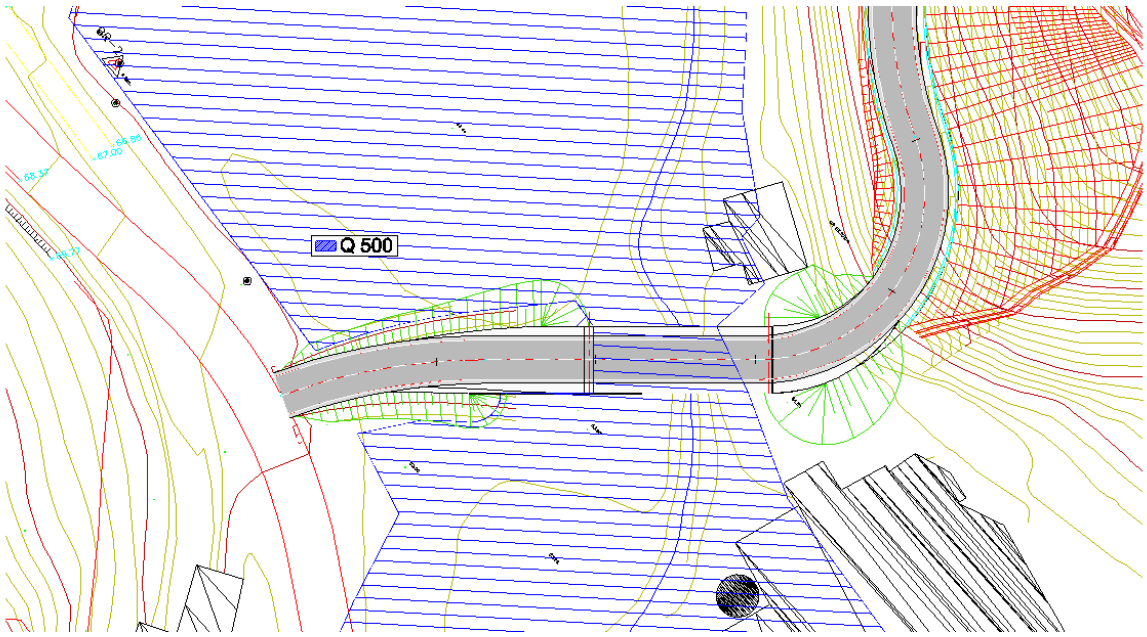

Figure 63: Map of water flooding for 500 years return period at the bridge section

10.5.2 Scour calculation

To calculate scour two different publications have been followed:

- "Control de la erosión fluvial en puentes" (Bridge's fluvial scour control), MOPU (1988).
- HEC-18 circular, "Evaluating scour at bridges". FHWA (2001).

Many hydraulic programs have been developed to calculate scour. HEC-RAS is a relevant choice, as it includes part of this methodology (contraction and local scour).

The Hydrologic Engineering Center's River Analysis System (HEC-RAS) is a hydraulic modeling program developed by the Hydrologic Engineering Center (HEC), used by the Federal Highway

Administration, and accepted by many agencies around the world. This software is free to use and guarantees state-of-the-art results due to continuous developments.

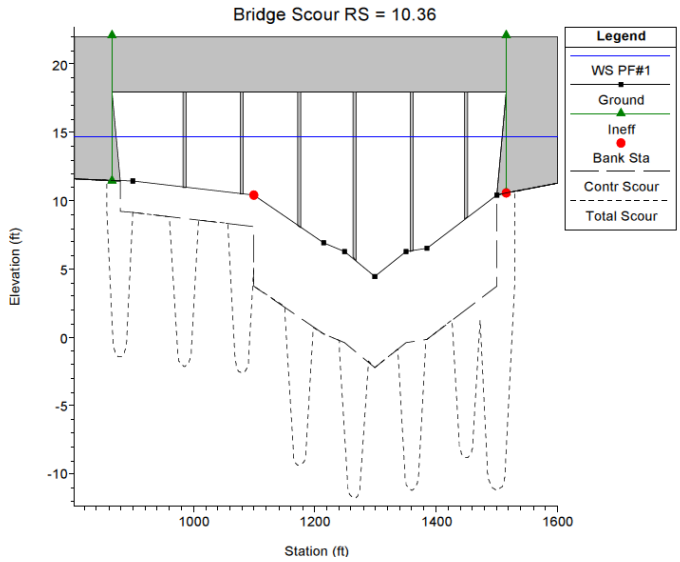

Figure 64: Typical Hec-Ras scour section

General Scour

The formulation applied to calculate the general erosion, comes from the D_{50} to characterize the bed material (D_{50} = Median diameter of bed material), and has the following expression, according to MOPU (1988):

$$e_{gen} = K \cdot y_r - y_0 \quad (75)$$

Where:

- e_{gen} = General scour. Minimum value: $y_0/4$;
- K = Average depth correction factor;
- $y_r = \alpha \cdot y_c$;
- α = correction factor based on the size of the river bedstream material, from figure 4.9 of the MOPU guide;
- y_c = Critical depth;
- y_o = Normal depth.

General scour in the abutment nº 1 is 0.37 m, according to the following computation sheet (Table 24). Scour is treated in a deterministic way and the probabilistic aspect is introduced by the input flow and the associated return period of rainfall.

Table 24: Computation of general scour

Return period:	**Tr= 500 years**	
Flow:	**Q= 64.93 m3/s**	
		Abutment
Water surface level:	WS=	65.09
Critical depth level:	Crit.WS=	64.08
Streambed level:	Z streambed=	63.61
Flood máximum depth:	**yo=**	**1.48**
BEDSTREAM GENERAL SCOUR		
Regular sections		
MAXIMUM SCOUR DEPTH:	**e_{gen}=y/4=**	**0.37**
Regime equations (Blench)		
Average depth correction factor:	K=	1.50
Median diameter of bed material: mm	D50=	2.00
Correction factor:	α =	2.50
Riverstream width:	B=	73.58
Riverstream width (form. Lacey):	B=	37.51
Unitary flow:	q=Q/B=	0.88
Critical depth (form. depending on q):	yc=	0.43
Critical depth:	yc=	0.47
Regimen depth:	yr=α.yc=	1.18
Majored regimen depth:	K.yr=	1.76
MAXIMUM SCOUR DEPTH:	e.g=K.yr-yo=	0.28
GENERAL SCOUR:	**e_{gen}=**	**0.37**

Contraction scour

To calculate contraction scour, the methodology of the HEC-18 circular has been followed. First the scouring condition has to be found, since according to the condition (whether Clear Water or Lived Bed), formulation to be used is different.

To calculate the critical velocity the equation used is (5.1, HEC-18):

$$V_c = K_u \cdot y^{1/6} \cdot D^{1/3} \quad (76)$$

Where:

- V_c = Critical velocity above which bed material of size D and smaller will be transported, [m/s];
- y = Average depth of flow upstream of the bridge, [m];
- D = Particle size for V_c, [m];
- K_u = 6.19 SI units.

If the critical velocity of the bed material is larger than the mean velocity ($V_c > V$), then clear-water contraction scour will exist, and if the critical velocity is less than the mean velocity ($V_c < V$), then live-bed contraction scour will exist.

Table 25: Comparison of V_C and V for the estimation of the contraction scour regime (clear-water or live-bed)

Vc=	0.81 m/s	Clear-Water
y=	1.22 m	
D=	0.0020 m	
D_{50}=	2.00 mm	
Ku=	6.19	
V=	0.75 m/s	

The equation for Clear Water contraction scour is (5.4, Hec-18):

$$y_2 = \left(\frac{K_u \cdot Q^2}{D_m^{2/3} \cdot W^2} \right)^{3/7} \quad (77)$$

$$y_s = y_2 - y_1 \quad (78)$$

Where:

- y_s = Scour depth;
- y_1 = Average depth in the upstream main channel, [m];
- y_2 = Average equilibrium depth in the contracted section after contraction scour, [m];
- Q = Discharge through the bridge or on the set-back overbank area at the bridge associated with the width W, [m^3/s];
- W = Bottom width of the contracted section less pier widths, [m];
- D_m = Diameter of the smallest non transportable particle in the bed material (1.25 x D_{50}) in the contracted section, [m];
- K_u = 0.025 [SI units];

Contraction scour is given in Table 26.

Table 26: Computation of contraction scour

y_2 =	2.94 m
Q =	64.93 m^3/s
D_m =	0.0025 m
D_{50} =	0.0020 m
D_{50} =	2 mm
W =	21.50 m
Y_o =	1.48 m
K_u =	0.025
y_s =	**1.46 m**

Local scour in the abutment

For abutments the equation used depends only on the ratio length of the embankment affected by water depth / scour depth. In the case of this study this ratio is lower than 25, so the formula to apply is Froelich's equation:

$$\frac{y_s}{y_a} = 2.27 \cdot K_1 \cdot K_2 \cdot \left(\frac{L'}{y_a}\right)^{0.43} \cdot Fr^{0.61} + 1 \quad (79)$$

Where:

- y_s = Scour depth, [m];
- K_1 = Coefficient for abutment shape
- K_2 = Coefficient for angle of embankment to flow $K_2 = \left(\frac{\theta}{90}\right)^{0.13}$
- L' = Length of active flow obstructed by the embankment, [m];
- y_a = Average depth of flow on the floodplain (A_e/L), [m];
- Fr = Froude Number of approach flow upstream of the abutment:

$$Fr = \frac{v_e}{\sqrt{g \cdot y_a}} \quad (80)$$

Where:

- v_e = Q_e/A_e, [m/s];
- Q_e = Flow obstructed by the abutment and approach embankment, [m3/s];
- A_e = Flow area of the approach cross section obstructed by the embankment, [m^2];
- L = Length of embankment projected normal to the flow, [m].

Contraction scour is given in Table 27.

Table 27: Computation of local scour

K_1 =	1.000
K_2 =	1
Θ =	90.00 º
L' =	36.77 m
y_a =	1.48 m
Fr =	0.164
G =	9.81 m/s^2
V_e =	0.62 m/s
Q_e =	33.20 m^3/s
A_e =	53.18 m^2
y_s =	**5.92 m**

10.5.3 Total Scour

Total scour depth in bridge B1 is given in Table 28.

Table 28: Computation of total scour

Contraction scour	Abutment Local scour	General Granular scour	Total scour
1.46 m	5.92 m	0.37 m	**7.75 m**

The value of total scour is 7.75 m but, as the width of the eroding substrate in this area is smaller (3.15 m, from the geotechnical study), total erosion will be 3.15 m.

10.6 Summary

Throughout the proof-of-concept example, intensity measures related to the different hazard types have been estimated for various locations of the virtual CI:

- Seismic hazard (i.e. PGA) at the three bridges;
- Landslide hazard (i.e. sliding displacement) at the slope along road segment B2-B3;
- Fluvial flood hazard (i.e. flow discharge and water elevation level) at bridge B1;
- Scour hazard (i.e. erosion depth) at bridge B1.

It has been shown that a true probabilistic model from source to site is available only in the case of earthquakes and landslides. For fluvial floods, the estimation of flow discharge at the various river cross-sections is carried out through a set of deterministic equations: the association of the flood level with a given return period is possible thanks to the probabilistic distribution of the source event (i.e. rainfall). The same observation can also be made regarding scour, which is estimated through deterministic equations based on the distribution of flow discharge and water height. Finally, this virtual example has the merit of highlighting the differences in terms of spatial scale and extent, which are highly dependent on the hazard type and the type of CI component (e.g. bridges treated as point-like objects for seismic hazard or line-like objects for flood and scour hazard).

11.0 HAZARD DISTRIBUTION MATRIX

Based on the chosen modelling of each hazard presented in section 5 to 9 and on the validation examples shown in section 10, it is possible to produce an Hazard Distribution Matrix: its aim is to provide the researcher / modeller with all the essential parameters that are required to evaluate the distributed IMs at sites, based on the characterization of the source event. The IMs have to be estimated in a way that they can be directly convolved with the component fragility functions, in order to complete the single risk assessment process. This matrix should contain sufficient information for the computation of a case-study like the one described in Section 10 or a more complex one.

Once values are being attributed to all the variables contained in the matrix and these are geo-referenced, these should be sufficient to determine the specific hazard/hazards and specific site/s to be selected for the single hazard risk analysis and then for the multi-hazard. The matrix should also aid the user in determining the best time-frame and space frame over which to conduct the risk analysis and the most appropriate model useful to propagate the uncertainties associated with the determination of the specific hazard.

It should be noted that in general a probabilistic treatment of the source variable has been used for each hazard. However for some hazards the site variables do not account for a probabilistic distributions, hence the IM at site is conditioned only by the source variables and not by the site variability condition.

Table 29: Hazard Distribution Matrix

	Earthquakes	**Landslides**	**Fluvial floods**	**Coastal floods**	**Scour**
Source event	Maximum (extreme) ground motion catalogue (Earthquake catalogue + GMPEs)	- Earthquake ground-motion - Rainfall	Rainfall	- Wind - Tide	Fluvial flood
Source variables	O = [seismicity parameters (b-value, N0, Mmax, depth), GMPEs, percentile/fractile]	- O = [PGA, PGV] - O = [rainfall intensity and duration]	O = [rainfall intensity and duration]	O = [duration and intensity of wind speed]	O = [depth, velocity, granulometry]
Site variables	S = [soil class / amplification factor, Lat&Lon coordinates]	S = [soil class, DEM, FS, soil saturation]	S = [DEM, channel section, time of concentration, soil conditions]	S = [fetch length, DEM]	S = [support location and shape (section, depth)]
Distributed IMs at sites	IM = {PGA, PGV, SA(T)}	IM = {PGD, debris volume, impact energy}	IM = {discharge (volume/time), water depth}	IM = {wind setup, wave height, wave period}	IM = {scour depth, spatial distribution}

Table 29: Hazard Distribution Matrix

Recommended method in INFRARISK	Monte-Carlo approach (synthetic earthquake catalogue => site-specific ground-motion catalogues with mean hazard curves + disaggregation and percentiles at select probability levels + GMPEs)	Infinite Slope model (analytical model with factor of safety and yield acceleration)	Rational Method (empirical equation linking rainfall intensity and peak flow discharge)	Empirical parametric model (1D-approximation)	HEC-18 (2001) method for contraction and local scour, MOPU guide (1988) for general scour
Model type	Probabilistic: $\lambda(IM) = P(IM \mid O,S)$	Probabilistic: $\lambda(IM) = P(IM \mid O,S)$	Probabilistic: $\lambda(IM) = P(IM \mid O,S)$	Probabilistic: $\lambda(IM) = P(IM \mid O,S)$	Semi probabilistic: $IM = f(O,S)$
Time Scale	Seconds to Minutes	Seconds to days	Hours to days	Hours to days	Hours to weeks
Return period	Defined by the performance level expected for the CI	Defined by the performance level expected for the CI	Follows from EV distribution	Follows from EV distr.	Linked to return period of fluvial floods
EV distribution	Gumbel / Weibull (extreme ground motions)	The earthquake triggered landslide hazard model is derived from the seismic hazard model therefore Gumbel/Weibull is suitable.	Normal (Gaussian), exponential, gamma, lognormal, Weibull, mixed exponential and hybrid exponential/Pareto distributions, generalized extreme value distr.	Normal (Gaussian), exponential, gamma, lognormal, Weibull, mixed exponential and hybrid exponential/Pareto distributions, generalized extreme value distr.	Linked to EV distribution of fluvial floods
Uncertainty sources	O, S	Soil parameters, displacement model (σ_{lnD}), epsilon (ϵ_D) due to probabilistic seismic hazard	Rainfall distribution, modelling parameters (e.g. concentration time, runoff model)	Wind speed distribution, modelling parameters (e.g. fetch length, basin shape)	Flow distribution, modelling parameters (streambed, structure support)
Model from IMs to EDP	Fragility curves: $P(EDP \geq edp \mid IM)$ EDP: structure deformation (e.g. drift)	Fragility curves: $P(EDP \geq edp \mid IM)$ EDP: road deformation / cracks	Vulnerability functions: Damage ratio = f(IM)	Vulnerability functions: Damage ratio = f(IM)	No models currently available.

12.0 CONCLUSION

Deliverable 3.1 details the general framework for the assessment of different hazard types, in the context of a single risk analysis. It is based on the harmonization of probabilistic models, which estimate a set of intensity measures at the vulnerable sites based on the occurrence of source events, accounting for various uncertainties (e.g. source, site or modelling variables). The parameters that are specific to each hazard types are then summarised in a Hazard Distribution Matrix, which allows to consider the appropriate inputs for the fragility functions of infrastructure components, starting from the extreme distribution of single source events.

Probabilistic models and recommended approaches have been identified for earthquakes, landslides and fluvial and coastal floods. In the case of scour, the intensity level is estimated through a set of deterministic equations, however, since the source conditions of scour are generated by fluvial flooding (with a probabilistic approach), it is possible to propagate the associated uncertainties up to the estimation of scour depth at bridge piers. For each hazard type, the distribution of appropriate intensity measures can then be derived for the distributed sites of the infrastructure, while the distributions of physical damage and losses will finally be combined and compared once the Fragility Functions Matrix has been developed (deliverable D3.2) and the two matrices convolved.

The case of cascading hazard events is also highlighted by the Hazard Distribution Matrix, where in some columns the source event is represented by the outcome of other hazard columns. Therefore, when interactions between hazard events are taken into account, the straightforward risk convolution of hazard and fragility matrices cannot be performed and other approaches such as probabilistic scenarios (e.g. within a Bayesian framework) have to be used.

This framework supports the overarching methodology that is presented in INFRARISK deliverable D4.1. The distinction between source events (i.e. initiating events) and hazard events (i.e. manifestation of the source event in terms of loading or intensity levels at sites), such as advocated in D4.1, is necessary in order to account for all sources of uncertainties at all steps of the risk assessment chain. Moreover, it allows for the application of probabilistic approaches such as event- or fault-trees (see Figure 65), while allowing at any step the integration of cascading hazards events.

The validation carried out in section 10 highlights that some of the current models available to compute the intensity at site for some of the hazard sources do not allow a complete probabilistic treatment, as for many of the tabled parameters used only deterministic equations are available. Spatial variability of site parameters, for instance is in some cases not considered in current state of the art procedures. However this shortfall can be treated in the risk analysis by introduction of epistemic uncertainty.

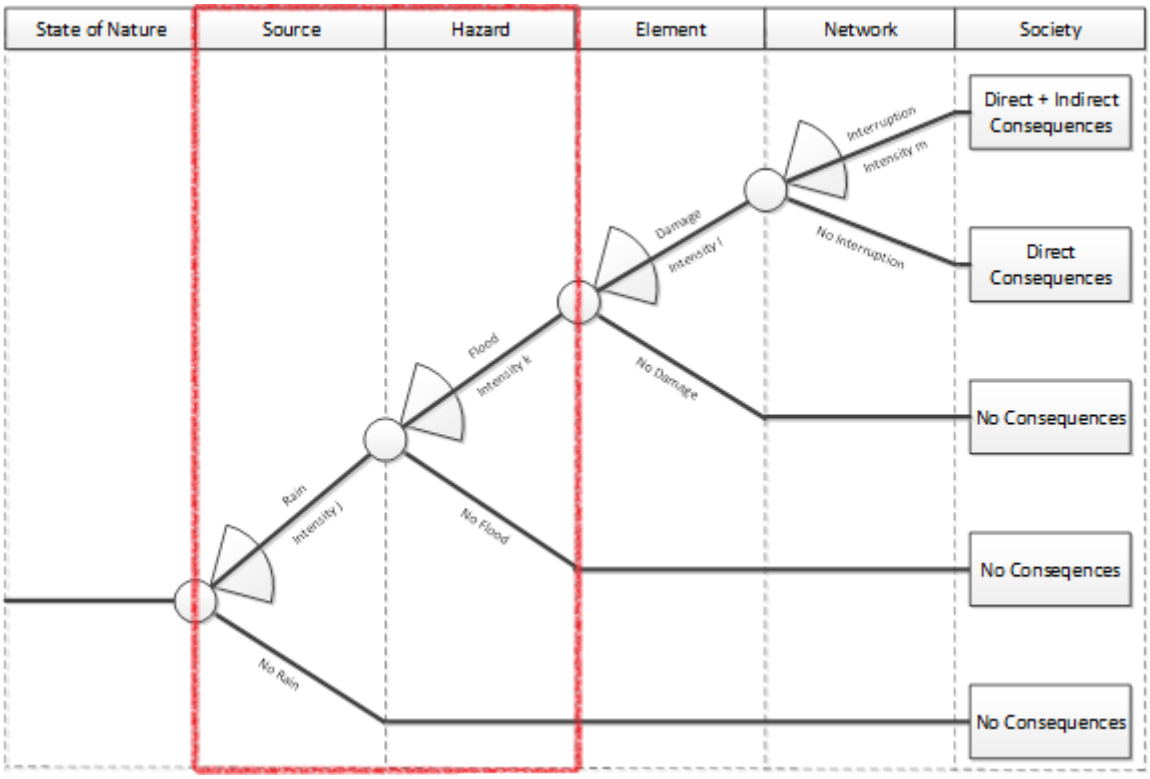

Figure 65: Event-tree structure proposed in deliverable D4.1. The red box highlights the elements the have been addressed in the present report.

13.0 REFERENCES

Atkinson, G., and Adams, J. 2013. Ground motion prediction equations for application to the 2015 Canadian national seismic hazard maps, Canadian Journal of Civil Engineering, 2013, 40(10): 988-998.

Atkinson, G., and Goda, K., 2013. Probabilistic seismic hazard analysis of civil infrastructure, in: S Tesfamariam, K Goda (eds) Handbook of Seismic Risk Analysis and Management of Civil Infrastructure Systems, Woodhead Publishing Ltd, Cambridge, pp. 3-28.

Baker, J.W., 2013. Probabilistic Seismic Hazard Analysis. White Paper V.2.0.1, 79 pp. (http://www.stanford.edu/~bakerjw/Publications/Baker_%282013%29_Intro_to_PSHA_v2.pdf, last accessed 02/06/2014).

Barbato, M., Petrini, F., Unnikrishnan, V. U., and Ciampoli, M., 2013. Performance-based hurricane engineering (PBHE) framework, Structural Safety, 45:24-35.

Bazzurro, P., 1998. Probabilistic seismic demand analysis. PhD Dissertation, Stanford University, California: s.n.

Bazzurro, P., and Cornell, C. A., 2002. Vector-valued probabilistic seismic hazard analysis. Boston, MA, s.n.

Bengtson, H. 2010. The Rational Method for Calculation of Peak Storm Water Runoff Rate, http://www.brighthubengineering.com/hydraulics-civil-engineering/60842-the-rational-method-for-calculation-of-peak-storm-water-runoff-rate

Bommer, J.J., and Scherbaum, F., 2008. The use and misuse of logic-trees in Probabilistic Seismic Hazard Analysis, Earthq. Spectra 24, no. 4, 997–1009.

Bommer, J.J., Scherbaum, F., Bungum, H., Cotton, F., Sabetta, F., and Abrahamson, N.A., 2005. On the use of logic trees for ground-motion prediction equations in seismic-hazard analysis, Bull. Seismol. Soc. Am. 95, 377–389.

Bradley, B.A., 2011. Empirical correlation of PGA, spectral accelerations and spectrum intensities from active shallow crustal earthquakes. Earthquake Engineering & Structural Dynamics, 40(15):1707–21.

Bray, J. D. & Traveasarou, T., 2007. Simplified procedure for estimating earthquake-induced deviatoric slope displacements. J Geotech Geoenviron Eng, 133(4), pp. 381-392.

Campbell, K.,and Bozorgnia, Y., 2008. NGA Ground Motion Model for the Geometric Mean Horizontal Component of PGA, PGV, PGD and 5% Damped Linear Elastic Response Spectra for Periods Ranging from 0.01 to 10 s. Earthquake Spectra, 24(1), 139–171.

Chang, F. M., 1973. A statistical summary of the cause and cost of bridge failures, Technical Report, FHWA-RD-75-87.

Chick, S., Shortle, J., Van Gelder, P., and Mendel, M., 1995. A Physics-Based Approach to Predicting the Frequency of Extreme River Levels, Engineering Probabilistic Design and Maintenance for Flood Protection, pp.89-107. Discussion: pp.109-138.

Chick, S., Shortle, J., Van Gelder, P., and Mendel, M., 1996. A Model for the Frequency of Extreme River Levels Based on River Dynamics, Structural Safety, Vol. 18, Nr. 4, pp.261-276.

Civil Engineering Portal, 2014. Weirs. http://www.engineeringcivil.com/weirs.html

Codecogs, 2014. Discharge over different types of weirs, Accessed on Sept. 2014. http://www.codecogs.com/library/engineering/fluid_mechanics/weirs/discharge.php

Cornell, C. A., 1968. Engineering Seismic Risk Analysis. Bulletin of the Seismological Society of America, 58(5), 1583–1606.

Crowley, H., and Bommer, J.J., 2006. Modelling Seismic Hazard in Earthquake Loss Models with Spatially Distributed Exposure, Bulletin of Earthquake Engineering, 4(3): 249–273

Crowley, H., Colombi, M., Crempien, J., Erduran, E., Lopez, M., Liu, H., Mayfield, M., and Milanesi, M., 2010. GEM1 Seismic Risk Report - Part 1. Seismic Risk Review, GEM Technical Report 2010-5, GEM Foundation, 194 pp.

De Waal, J.P. and van der Meer, J.W. 1992. Wave run-up and overtopping on coastal structures. Proceedings of 23rd International Conference on Coastal Engineering. ASCE, New York

de Zeeuw, J. W., 1973. Hydrograph analysis for areas with mainly groundwater runoff. In: Drainage Principle and Applications, Vol. II, Chapter 16, Theories of field drainage and watershed runoff. p 321-358. Publication 16, International Institute for Land Reclamation and Improvement (ILRI), Wageningen, The Netherlands.

Delavaud, E., Cotton, F., Akkar, S., Scherbaum, F.,·Danciu, L., Beauval, C., Drouet, S., Douglas, J., Basili, R., Abdullah Sandikkaya, M., Segou, M., Faccioli, E., and Theodoulidis, N., 2012. Toward a ground-motion logic tree for probabilistic seismic hazard assessment in Europe, Journal of Seismology, 16: 451-473.

Demuth, S., and Kulls, C., 1997. Probability analysis and regional aspects of droughts in southern Germany, Sustainability of water recourses under increasing uncertainty / Proceedings of Rabat Symposium, IAHS Publ. 240.

Eadie, C., and Favis-Mortlock, D., 2010. Estimation of drought and flood recurrence interval from historical discharge data: a case study utilising the power law distribution, EGU General Assembly 2010, held 2-7 May, 2010 in Vienna, Austria, p.13568.

EPRI. 2002. Seismic Fragility Application Guide, 1002988, 210 pp.

Federal Emergency Management Agency. 2007 Coastal Flood Hazard Analysis and Mapping for the Pacific Coast of the United States. Washington D.C.

Ferrer, F. J., 1993. Recomendaciones para el cálculo hidrometeorológico de avenidas, Madrid, CEDEX, Ministerio de Fomento, 76pp.

FHWA, 2002. Hydraulic Design Series No. 2, Second Edition, Highway Hydrology, Federal Highway Administration.

FHWA, 2001a. Evaluating scour at bridges, Technical report, Federal Highway Administration, Hydraulic Engineering Circular 18.

FHWA, 2001b. Stream Stability at Highway Structures, Technical report, Federal Highway Administration, Hydraulic Engineering Circular 20.

Fourie, A. B., Owe, D. R. & Blight, G. E., 1999. The effect of infiltration on the stability of the slopes of a dry ash dump. Geotechnique, 49(1), pp. 1-13.

Garcia-Aristizabal, A., and Marzocchi, W., 2012. Bayesian multi-risk model: demonstration for test city researchers

Gavin, K. & Xue, J. F., 2008. A simple method to analyze infiltration into unsaturated soil slopes. Computers and Geotechnics, 35(2), pp. 223-230.

Green, W. H. & Ampt, C. A., 1911. Studies on soil physics: Flow of air and water through soils. Journal of Agricultural Science, Volume 4, pp. 1-24.

Griffiths, G.A., 1989. A theoretically based Wakeby distribution for annual flood series, Hydrological Science Journal, 34(3): 231-243.

Guha-Sapir, D., Below, R., and Hoyois, Ph., 2009. EM-DAT: International Disaster Database – www.emdat.be – Université Catholique de Louvain – Brussels – Belgium.

Hao, Z., and Singh, V.P., 2011. Bivariate drought analysis using entropy theory, Symposium On Data-Driven Approaches To Droughts.

Hong, H.P., and Goda, K., 2006. A comparison of seismic-hazard and risk deaggregation, Bull. Seismol. Soc. Am. 96, 2021–2039.

Hong, H.P., Goda, K., and Davenport, A.G., 2006. Seismic hazard analysis: a comparative study, Canadian Journal of Civil Engineering, 33(9), 1156-1171.

Hosking, J.R.M., and Wallis, J.R., 1997. Regional Frequency Analysis: An Approach based on L-Moments. Cambridge University Press, Cambridge, UK.

ILRI, 1995. Land drainage and soil salinity: some Mexican experiences. In: ILRI Annual Report 1995, p. 44-53. International Institute for Land Reclamation and Improvement, Wageningen (ILRI), The Netherlands.

Jayaram, N., and Baker, J.W., 2009. Correlation Model For Spatially-Distributed Ground-Motion Intensities, Earthquake Engineering and Structural Dynamics, 38(15): 1687–1708.

Jayaram, N., and Baker, J.W., 2010. Efficient sampling and data reduction techniques for probabilistic seismic lifeline risk assessment. Earthquake Engineering and Structural Dynamics, 39: 1109-1131.

Jibson, R., 2007. Regression models for estimating coseismic landslide displacement. Eng Geol, Volume 91, pp. 209-218.

Jibson, R. W., Harp, E. L. & Micheal, J. A., 2000. A method for producing digital probabilistic seismic landslide hazard maps. Engineering geology, Volume 28, pp. 271-289.

Jury, W. A. & Horton, R., 2004. Soil Physics. New Jersey: John Wiley & Sons Inc.

Kim, Y.C., Choi, M., and Cho, Y.S., 2012. Tsunami Hazard Area Predicted by Probability Distribution Tendency, Journal of Coastal Research, 28(5): 1020-1031.

KNMI, 2014. Wind speed data obtained from KNWI website: http://www.knmi.nl/klimatologie/onderzoeksgegevens/potentiele_wind/index.cgi?language=eng

Knox County, TN Stormwater Management Manual, 2008, Volume 2 - Whole Manual, Accessible via: http://www.knoxcounty.org/stormwater/volume2.php

Krawinkler, H., 1999. Challenges and progress in performance-based earthquake engineering, In International Seminar on Seismic Engineering for Tomorrow, In Honor of Professor Hiroshi Akiyama, Tokyo, Japan.

Liang, Q., Borthwick, A. G. L. and Stelling, G. 2004. Simulation of dam- and dyke-break hydrodynamics on dynamically adaptive quadtree grids. International journal for numerical methods in fluids 46, 127–162.

Lin, N., Emanuel, K., Oppenheimer, M., and Vanmarcke, E., 2012. Physically Based Assessment of Hurricane Surge Threat Under Climate Change, Nature Climate Change 2(6): 462–467.

Lloyd, B., and Saunders, H.M., 2002. A Drought Climatology for Europe, Int. J. Climatol., 22: 1571-1592.

Marzocchi, W., Garcia-Aristizabal, A., Gasparini, P., Mastellone, M. L., and Di Ruocco, A., 2012. Basic principles of multi-risk assessment: a case study in Italy, Natural Hazards, 62:551-573.

MATRIX, 2010-2013. New Multi-HAzard and MulTi-RIsK Assessment MethodS for Europe, FP7 Project coordinated by J. Zschau, German Research Centre for Geosciences, Potsdam, Germany.

MATRIX, 2014. MATRIX Final Report, New Multi-HAzard and MulTi-RIsK Assessment MethodS for Europe, FP7 Project coordinated by J. Zschau, German Research Centre for Geosciences, Potsdam, Germany, http://matrix.gpi.kit.edu/index.php

McCrink, T. P., 2001. Mapping earthquake-induced landslide hazards in Santa Cruz County. In: H. Ferriz & R. Anderson, eds. Engineering geology practice in northern California: California Geological Survey Bulletin 210. s.l.:s.n., pp. 77-94.

McGuire, R., 2004. Seismic hazard and risk analysis. EERI Monograph MNO-10. Earthquake Engineering Research Institute, Oakland, Calif., 221 pp.

Mendel, M.B., and Chick, S.E., 1993. The Geometry and Calculus of Engineering Probability, UC-Berkeley, Lecture notes, December 1993.

Miller, M., and Baker, J.W., 2013. A Framework for Selecting A Suite Of Ground-Motion Intensity Maps Consistent With Both Ground-Motion Intensity And Network Performance Hazards For Infrastructure Networks, 11th International Conference on Structural Safety & Reliability, New York, NY, 8 pp.

Ministry of Public Works, Spain 1990. Instrucción de Carreteras 5-2IC, Drenaje superficial

MOPU, 1988. Control de la erosión fluvial en puentes, Tecnología carreteras, 29.

Musson, R.M.W. 1999. Determination of Design Earthquakes in Seismic Hazard Analysis Through Monte Carlo Simulation, Journal of Earthquake Engineering, 3: 463-474.

Musson, R.M.W., 2000. The use of Monte Carlo simulations for seismic hazard assessment in the U.K., Ann. Geofisc. 43, 1–9.

Musson, R.M.W., 2012. PSHA validated by quasi observational means, Seismol. Res. Lett. 83, 130–134.

NRC, 2010. Interim Staff Guidance on Implementation of a Probabilistic Risk Assessment-Based Seismic Margin Analysis for New Reactors DC/COL-ISG-020.

Newmark, N. M., 1965. Effects of earthquakes on dams and embankments. Geotechnique, 15(2), pp. 139-160.

NIBS, N. I. o. B. S., 2004. HAZUS-MH: User's manual and technical manuals, Washington D.C: Federal Emergency Management Agency.

Perreault, L., Bobée, B., and Rasmussen, P.F., 1999. Halphen Distribution System. I: Mathematical and Statistical Properties, Journal of Hydrologic Engineering--July 1999, Volume 4, Issue 3, pp. 189-296.

Pickands, J., 1975. Statistical inference using extreme order statistics, The Annals of Statistics, 3(1): 119-131.

Rathje, E. M. & Saygili, G., 2011. Pseudo-probabilistic versus fully probabilistic estimates of sliding displacements of slopes. J Geotech GeoEnviron Eng, 137(3), pp. 208-217.

Rathje, E. M. S. G., 2008. Probabilistic seismic hazard analysis for the sliding displacement of slopes: scalar and vector approaches.. J geotech Geoenviron Eng, 134(6), pp. 804-814.

Rathje, E. M. S. G., 2009. Probabilistic assessment of earthquake-induced sliding displacements of slopes.. Bull N Z Soc Earthq Eng, Volume 42, pp. 18-24.

Rathje, E. M. et al., 2013. Probabilisitic assessment of the seismic performance of earth slopes. Bull Earthquake Eng, 12(3), pp. 1071-1090.

Safeland, 2011. D2.5 Physical vulnerability of elements at risk to landslides: Methodology for evaluation, fragility curves and damage states for buildings and lifelines, s.l.: European Union Seventh Framework Programme.

Saygili, G., 2008. A propabilistic appraoch for evaluating earthquake-induced landslides. PhD Dissertation, University of Texas at Austin, Austin(TX): s.n.

Saygili, G. & Rathje, E. M., 2008. Empirical predictive models for earthquake-induced sliding displacements of slopes. J Geotech Geoenviron Eng, 134(6), pp. 790-803.

Saygili, G. & Rathje, E. M., 2009. Probabilistically based seismic landslide hazards maps: An application in Southern California. Engineering Geology, 109(3-4), pp. 183-194.

Schultz, M., Gouldby, B., Simm, J. & Wibowo, J., 2010. Beyond the factor of safety: Developing fragility curves to characterize system reliability, Washington DC: US Army Corps of Engineers.

Selva, J., 2012. ByMuR model: interaction among risks and uncertainty treatment in long-term multi-hazard/risk assessments, Proceedings of the AGU Fall Meeting, San Francisco, California.

Shiraki, N., Shinozuka, M., Moore II, J.E., Chang, S.E., Kameda, H., and Tanaka, S., 2007. System Risk Curves: Probabilistic Performance Scenarios for Highway Networks Subject to Earthquake Damage, Journal of Infrastructure Systems, 213(1): 43–54.

Strasser, F., Abrahamson, N., and Bommer, J. 2009. Sigma: Issues, insights and challenges. Seismological Research Letters, 80(1): 40–56. doi:10.1785/gssrl.80.1.40.

SYNER-G, 2011. A Review and Preliminary Application of Methodologies for the Generation of Earthquake Scenarios for Spatially Distributed Systems, D2.13 Deliverable, 90 pp.

Temez, J.R., 1991. Extended and improved rational method. Version of the Highways Administration of Spain. Madrid, Proceedings of XXIV IAHR Congress, 33-40.

U.S. Army Corps of Engineers, 2003. Coastal Engineering Manual. U.S.Army Corps of Engineers, Washington D.C.

U.S. Army Corps of Engineers, 1984. Shore Protection Manual. Dept. of the Army, Waterways Experiment Station.

U.S. Army Corps of Engineers, 1980. Hydrographs by Single Linear Reservoir Model. Institute for Water Resources, Hydrologic Engineering Center.

van Gelder, P.H.A.J.M., J.G. de Ronde, N.M. Neykov, Pl. Neytchev, REGIONAL FREQUENCY ANALYSIS OF EXTREME WAVE HEIGHTS: TRADING SPACE FOR TIME, Proceedings of the 27th ICCE, pp. 1099-1112, Vol. 2, Coastal Engineering 2000, Sydney, Australia.

Vrijling 2000. Lectures notes on probabilistic design in hydraulic engineering, TU Delft.

Wikipedia Runoff Models, 2014. Retrieved from:
http://en.wikipedia.org/wiki/Runoff_model_(reservoir)

Woessner, J., Danciu, L., Kästli, P., and Monelli, D. 2013. D6.6 – Databases of seismogenic zones, Mmax, earthquake activity rates, ground motion attenuation relations and associated logic trees (Available at www.share-eu.org).

Yusof, F., and Hui, F., 2012. Use of Statistical Distribution for Drought Analysis, Applied Mathematical Sciences, 6(21): 1031-1051.

Zorraquino, C., 2004. The SQRT-ET_{MAX} Model, Revista de Obras Publicas, 3.447:33-37.

APPENDIX A: DISTRIBUTION FUNCTIONS USED IN CLIMATOLOGY

Continuous distributions: normal (Gaussian), exponential, gamma, lognormal, Weibull, mixed exponential and hybrid exponential/Pareto distributions, extreme value.

Normal distribution can be used for sums or averages over several days or months such as temperature below 0°C, above 30°C and so on. For daily rainfall and wind speed, the most commonly used distributions are Gamma (Pearson type III), Weibull, exponential distributions. For extreme values over a period (maximum wind speed, minimum temperature, greatest 24-hr rainfall) distributions such as extreme value distribution GEV or log-Pearson type III can be used.

Discrete distributions: binomial, multinomial, Poisson, hypergeometric, negative binomial. Binomial distribution could be used for number of free frost days, number of crop failures and so on (data has no inter annual dependencies). Poisson distribution can be used for number of cyclones, for example.

Example: wind load data at airport Schiphol

According to statistics the instantaneous wind speed distribution is approximately Weibull. EV-theory says that the domain of attraction is Gumbel. If we plot the *monthly* maxima of hourly averaged wind speeds, then we obtain:

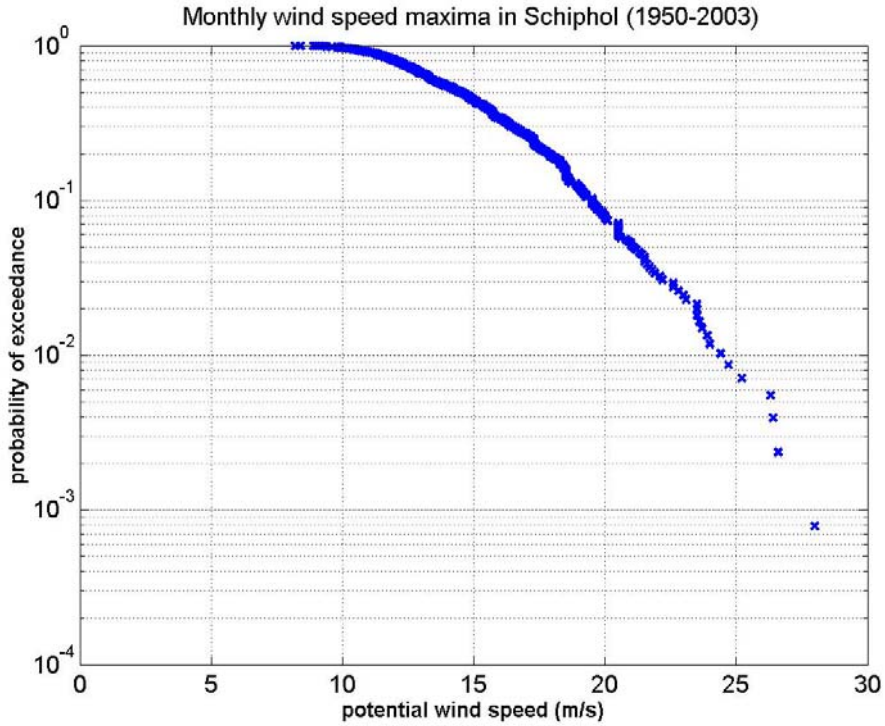

Figure 66: Monthly maxima of hourly averaged wind speeds at Schiphol airport (data obtained from KNMI, 2014)

The above figure indicates a slightly convex behavior (instead of a straight line). If we plot the data on Gumbel paper, we obtain:

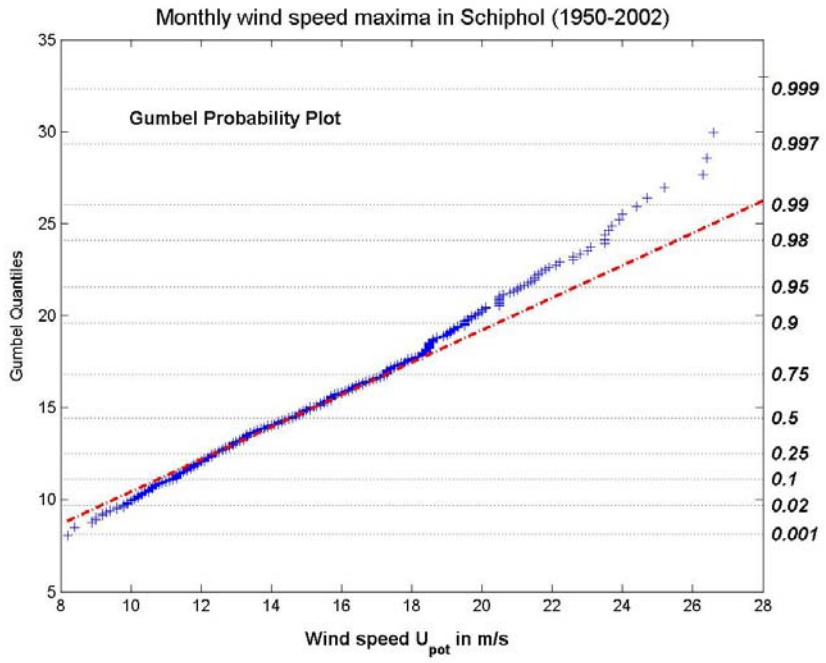

Figure 67: Monthly maxima of hourly averaged wind speeds at Schiphol airport, plotted on Gumbel paper

We notice a deviation from a straight line, and therefore Gumbel is apparently not the appropriate distribution for this extreme value data.

The wind speed *annual* maxima data at Schiphol does show a Gumbel behavior, as seen from:

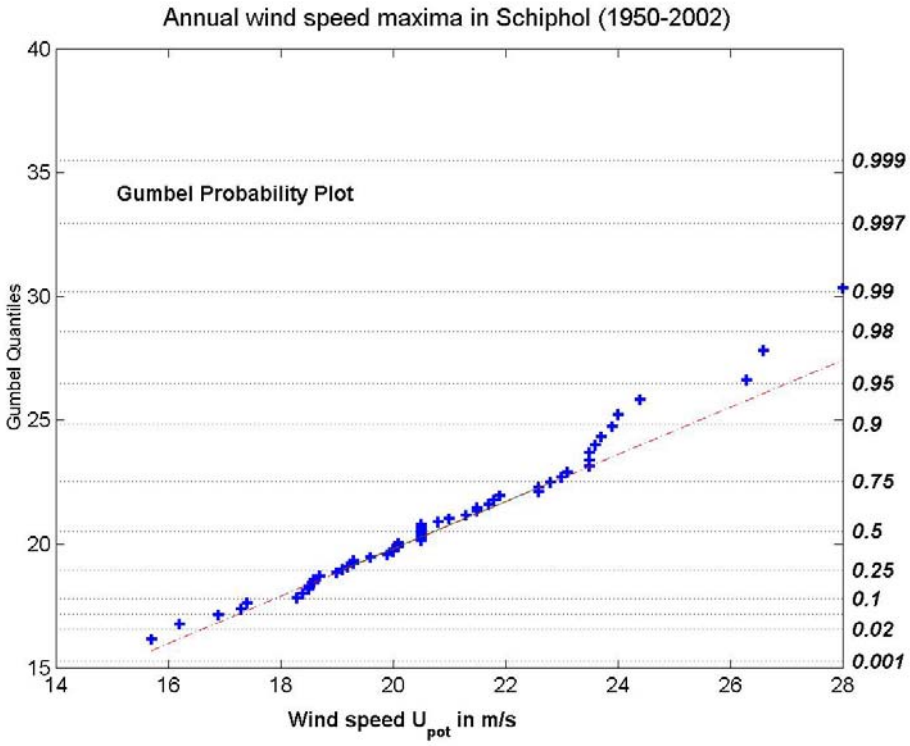

Figure 68: Annual maxima of hourly averaged wind speeds at Schiphol airport, plotted on Gumbel paper

From the above example, it is shown that convergence to an asymptotic distribution can be quite slow. Monthly maxima is not well enough converged. Annual maxima are needed, for the wind load data.

If we step over to *wind pressure* data monthly maxima Schiphol, then the convergence is much faster, as can be seen from:

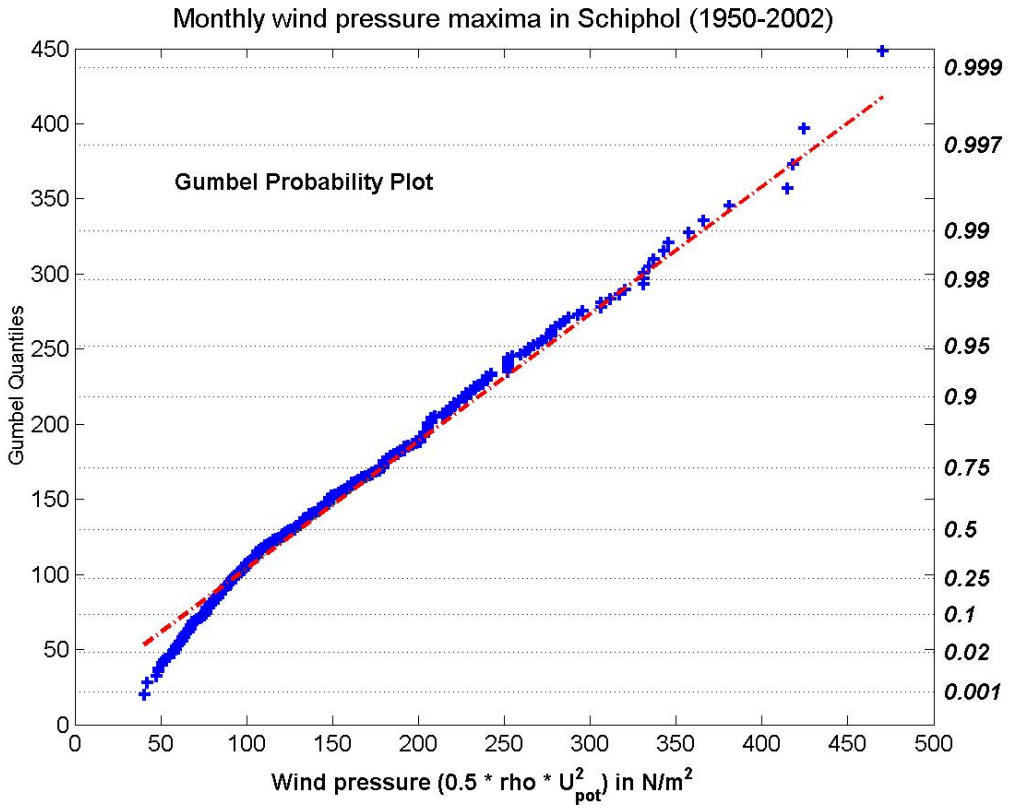

Figure 69: Monthly maxima of hourly averaged wind pressures at Schiphol airport, plotted on Gumbel paper

APPENDIX B: DISTRIBUTION FUNCTIONS USED IN HYDROLOGY AND HYDRAULICS

Common: Normal, lognormal, Gamma family and related distributions: exponential, three parameters gamma (Pearson type III, Kritsky-Menkel (Stacy distribution)), lognormal, beta.

Special (for extreme values): Poisson – frequency of events during fixed time intervals (for example in year) (example application: annual storm frequency in NY) (Lin et al., 2012), Gumbel, Weibull, Frechet, General extreme value – GEV (generalized form of Gumbel, Weibull and Frechet), Two component extreme value, Wakeby (Griffiths, 1989).

Drought (runoff data):

The lognormal, the generalized extreme value, the Pearson III and the generalized Pareto distributions (Demuth and Kulls, 1997).

Hao and Singh (2011) state the following: *"A traditional way to characterize the drought duration or severity is based on fitting a probability density function. The drought duration can be modeled by a geometric distribution (discrete) or an exponential distribution (continuous). The gamma distribution is generally used to model drought severity."*

Pluvial floods/droughts:

Exponential, gamma distribution and Weibull (Yusof and Hui, 2012).

Gamma (Lloyd and Saunders, 2002).

Coastal floods:

GEV.

Normal, Lognormal, Exponential, and Gumbel distributions were used by (Kim et al., 2012).

Regional frequency analysis of wave heights indicate a Generalized Pareto distribution as the analytical distribution function to be used. Within a regional frequency-analyses the idea is the "Use of data from neighbouring locations in order to determine more accurately the distribution function at a specific location".

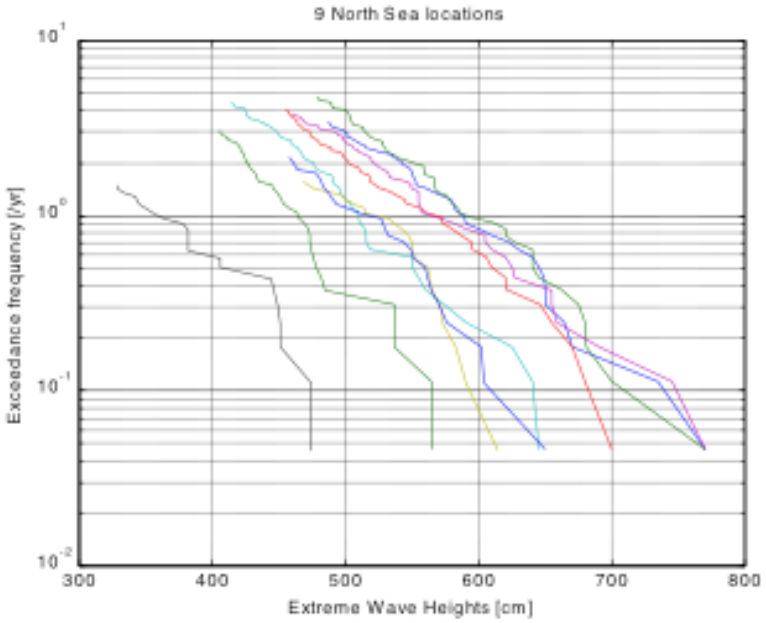

Figure 70: Regional frequency analysis of wave heights in 9 North Sea locations (Van Gelder et al., 2000)

Assume the sea levels in Hook of Holland exponentially distributed with parameter λ. In the figure below the ten highest sea levels at Hoek van Holland (>180cm) are depicted. In the same figure the distribution of X_{max} (being $(1-e^{-\lambda x})^n$) and the limit distribution (being Gumbel with mean 281cm and standard deviation 45cm) are given.

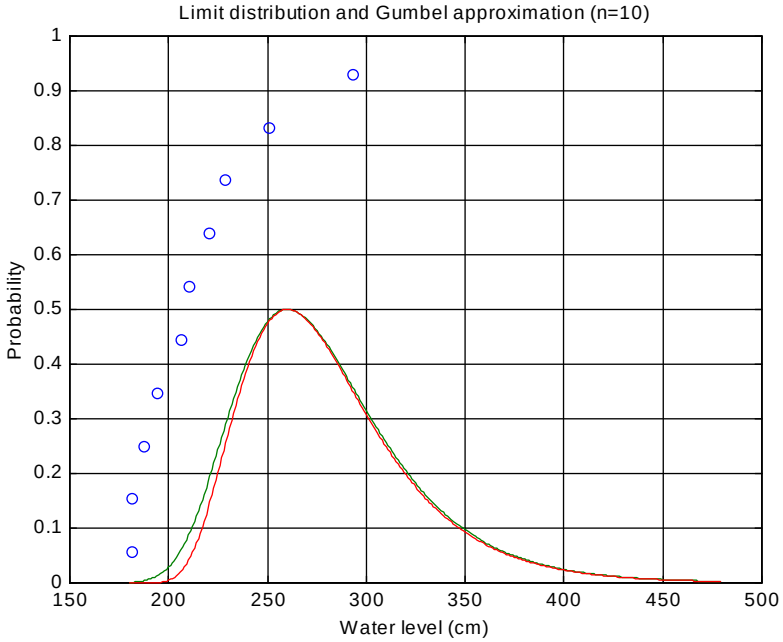

Figure 71: Extreme values with n=10 (parent distribution is Exponential)

Fluvial floods/droughts:

Eadie and Favis-Mortlock (2010) state the following:

"The choice of which statistical distribution to fit to historical discharge data is critical when attempting to predict the most extreme flows. It has been shown that depending upon the distribution selected, the calculated return periods can vary dramatically. Cunnane (1985) discussed the factors affecting the choice of distribution for river flow series data, and was able to show that small differences in the Extreme Value Type 1 (Gumbel), Type 2, and Type 3 can lead to large differences in the predicted return period. Indeed this divergence increases as the return period becomes larger: a finding which has obvious implications for fluvial management. Despite this, in many studies which fit a frequency-magnitude distribution to fluvial discharge data, the choice of distribution appears driven by regional convention, or even by some other apparently arbitrary factor. Benson (1968) analysed data for ten US stations, and compared the fit using the log-normal, gamma, Gumbel, log-Gumbel, Hazen and log-Pearson type 3 distributions. On the basis of this study alone, the standard approach to flow frequency estimation in the USA became the fitting of a log-Pearson type 3 (LP3) distribution (US Water Resources Council, 1982). While several other countries have adopted a similar approach, usage of the LP3 distribution is not geographically universal. Hydrologists in the United Kingdom conventionally utilizing a fitted logistic distribution for flow frequency estimation (Robson and Reed, 1999) while Chinese hydrologists utilize the log-normal distribution (Singh, 2002). Choice of fitted distribution is obviously crucial, since selecting one distribution rather than another will change the estimated probabilities of future droughts and floods, particularly the largest and rarest events. Malamud et al. (1996) showed that a flood of equivalent size to that experienced on the Mississippi in 1993 has a recurrence interval on the order of 100 years when a power-law distribution is fitted, but a much longer recurrence interval — on the order of 1000 years — using the USA's standard LP3 method. In addition Pandey et al. (1998) found that fitting a power-law distribution, compared with fitting a Generalized Extreme Value distribution, can lead to a large decrease in the predicted return period for a given flood event. Both these findings have obvious implications for river management design. Power-law distributions have been fitted to fluvial discharge data by many authors (most notably by Malamud et al., 1996 and Pandey et al., 1998), who then use these fitted distributions to estimate flow probabilities. These authors found that the power-law performed as well or better than many of the distributions currently used around the world, despite utilizing fewer parameters. The power-law has not, however, been officially adopted by any country for fitting to fluvial discharge data. This paper demonstrates a statistically robust method, based on Maximum Likelihood Estimation, for fitting a power-law distribution to mean daily streamflows. The fitted distribution is then used to calculate return periods, which are compared to the return periods obtained by other, more commonly used, distributions. The implications for river management, extremes of flow in particular, are then explored."

APPENDIX C: CASE OF NON-STATIONARY DATA

Extreme events are non-stationary data, as can be seen from the following figure:

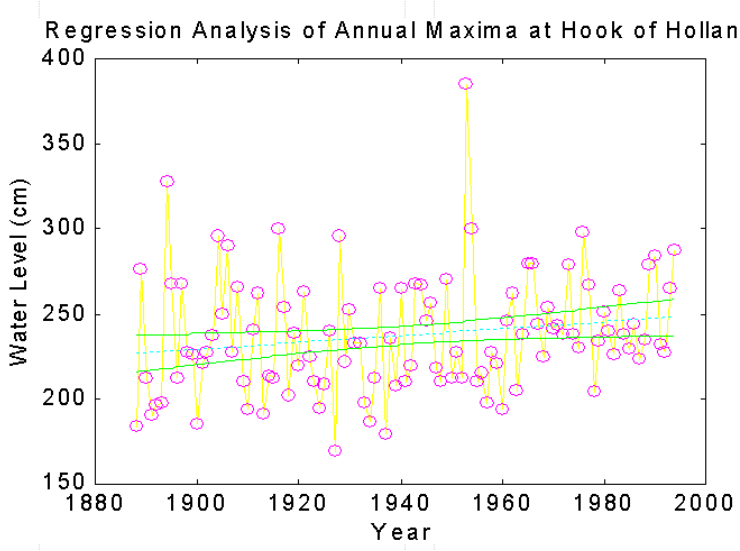

Figure 72: Annual water level maxima at Hook of Holland (data obtained from KNMI, 2014)

It should be realized that because of climate change or non-stationary behavior of time series in general, the return periods of extreme events can be reduced. An event which used to be a 1-in-100 years event, now might be a 1-in-50 years event, depending on the actual case study. This is shown from the following statistical modelling exercise:

Top 10 observations of annual maxima of sea levels (m + MSL) over a period of 100 years:

2.8238 2.9635 2.2672 2.2292 3.6773 2.7138 2.8084 2.4365 2.3434 2.2815

The record value (3.7m) is a 3.10^{-3} event (once in 333 years):

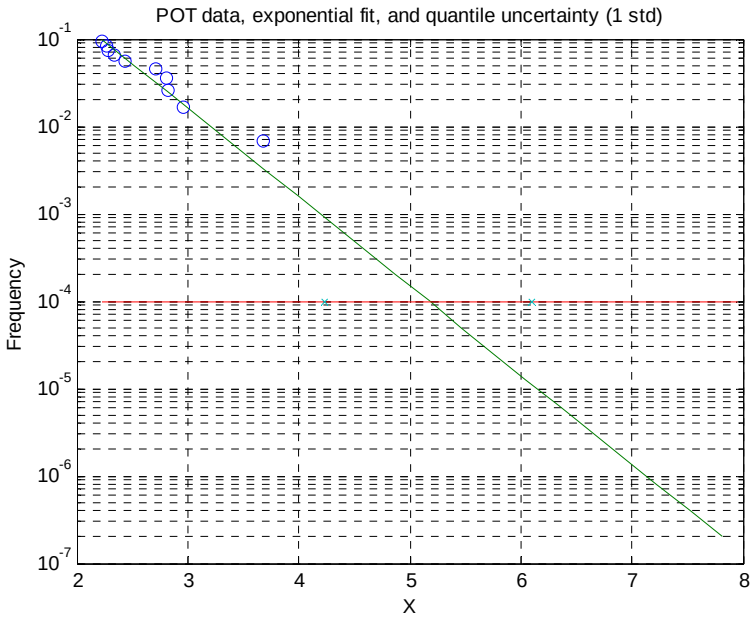

Figure 73: Frequency analysis of the test data

Now, 3.7 m corresponds to a $7*10^{-3}$ event (once in 142 years):

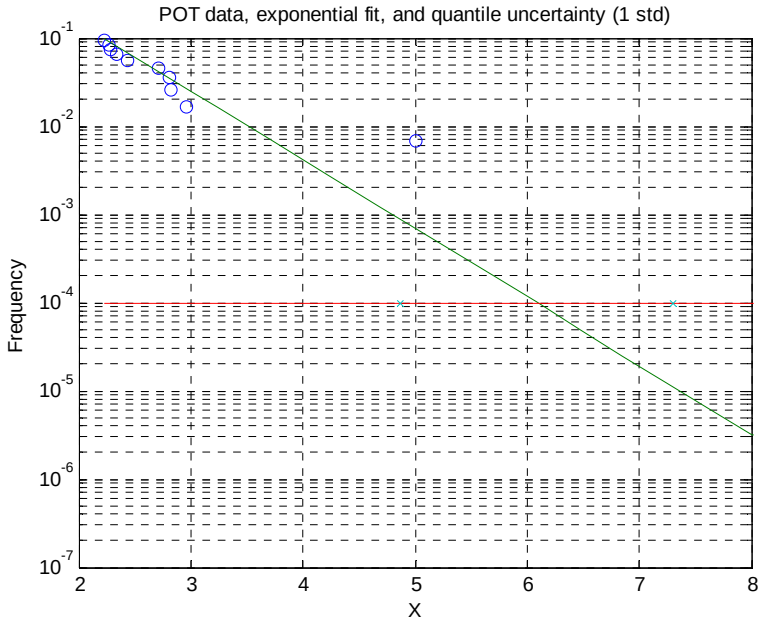

Figure 74: Frequency analysis of the test data

In other words, the occurrence of extreme events (due to climate change) causes the return periods to decrease.